Dissertation

On-chip Biosensing Using Magnetic Particles

ausgeführt zum Zwecke der Erlangung des akademischen Grades eines Doktors der technischen Wissenschaften unter der Leitung von

Univ.-Prof. Dr. Franz Keplinger

eingereicht an der Technischen Universität Wien
Fakultät für Elektrotechnik und Informationstechnik

von

Georgios Kokkinis

Benedikt-Schellingergasse 7/6, 1150 Wien
Matr.-Nr. 1227703

Wien, im April 2016

Erstbegutachter	Univ.-Prof. Dr. Franz Keplinger Vienna University of Technology, Vienna, Austria
Zweitbegutachter	Univ.-Prof. Dr. Evangelos Hristoforou National Technical University of Athens, Athens, Greece

ΠΑΝΤΑ ΡΕΙ

Alles fließt

Contents

Abstract

In the recent years, there is a growing interest in microfluidic platforms using magnetic particles in combination with magnetic sensors seeking to tackle a wide range of challenges in biomedicine and biotechnology. The goal of this thesis is to propose such platforms utilizing unexplored methods for pathogen detection, biomolecule resolution, biomolecule quantification and rare cell trapping for further analysis.

The first part of this work (Chapters 2 - 4) presents a biosensor for bacteria detection using the magnetically induced motion of functionalized superparamagnetic microparticles (SMPs). The concept of the proposed method is that the induced velocity on SMPs in suspension, while imposed to a magnetic field gradient, is inversely proportional to their volume. Specifically, a velocity variation of the functionalized SMPs inside a detection microchannel with respect to a reference velocity, specified in a parallel reference microchannel, indicates an increase in their non-magnetic volume. This volumetric increase of the SMPs is caused by the binding of organic compounds (e.g. bacteria) on their functionalized surface.

During the course of the experiments for the aforementioned biosensor, it was realized that friction plays an important role in the motion of particles that were in contact with the chip's surface. Out of that observation, a biosensor for the detection of biomolecules is proposed, where the friction is for the first time utilized for the resolution of biomolecules. The principle is used for the development of an antibody detection system. The results were verified with Atomic Force Microscopy (AFM) measurements (Chapter 5).

Furthermore, a modified biosensor system is used for the detection and quantification of nanomarkers due to their high biomedical relevance. Firstly, detection of commercial Nanomag-D particles of 250 nm diameter is presented (Chapter 6). The results show that the sensor is capable of detecting concentrations as low as 500 pg/µl of Nanomag-D particles and quantifying them in a linear scale over a wide particle concentration range (1 - 500 ng/µl). Subsequently, cus-

tom made alginate functionalized nanoparticles are tested and their detection for concentrations of 100 - 1000 ng/µl, over a linear scale is presented (Chapter 7). Lastly, it is reported in both cases, that the particle concentration is correlated to the time the particles need to accumulate on the sensor's surface.

The last part of this work suggests rare cell isolation systems. The first system incorporates a polymer microtrap with integrated current carrying microconductors (Chapter 8). The later drive leukaemia cells tagged with magnetic microparticles towards the microtrap. This entrapment allows for the further analysis of the cells with many advantages in the area of diagnostics and therapeutics. Finally a second isolation cell system is presented (Chapter 9). This time sequentially actuated conductors and giant magnetoresistance sensors are used for trapping and detecting magnetic micromarkers.

All the systems presented in this thesis are compact, portable and cost effective lab-on-chip systems. The utilized technologies render them appealing for economies of scale, while their low cost in addition to their straightforward operation make them ideal for Point of Care testing and for laboratories operating in poor conditions.

Chapter 1
Introduction

1.1 Motivation

Lab on a chip technologies have drawn considerable attention the last two decades. Scientific research driven by the promise for miniaturization and integration of complex laboratory equipment on inexpensive, reliable and accurate devices, has successfully migrated several analytical and diagnostic methods to the submillimeter scale. The miniaturization process was made possible with the birth of microfluidics, a technology that could confine, manipulate and mix very small volumes of liquids on devices integrated on standard silicon technology chips. The impact of microfluidic technologies to the scientific community is outlined by a 500% surge in peer reviewed journal publications reported between 2002 and 2012 (Figure 1.1) [1].

The main advantages of microfluidic approaches over traditional benchtop analytical (chemistry) and biomedical tools can be attributed to the unique behaviour of fluids in the microscale; most importantly the fact that due to inherently small Reynolds numbers, fluids flow almost exclusively within the laminar flow regime [2]. This allows for an accurate prediction and simulation of the flow profile. Equally important is that gravitational forces are irrelevant due to the small characteristic length of the devices, while surface and interfacial surface forces are dominant. These forces allow for a set of beneficial operations such as: passive pumping of fluids into the devices [3], user defined patterned surfaces [4], filtering out unwanted substances, forming encapsulations of a curtain fluid into multiphase fluid flows, the so called droplet microfluidics and lastly the formation of easy manipulatable, discrete droplets for mixing, storage, analysis and reaction of fluids in a discrete manner. This subcategory of microfluidic systems is know as digital microfluidics. One last advantage of microfluidics, is the presence of the capillary

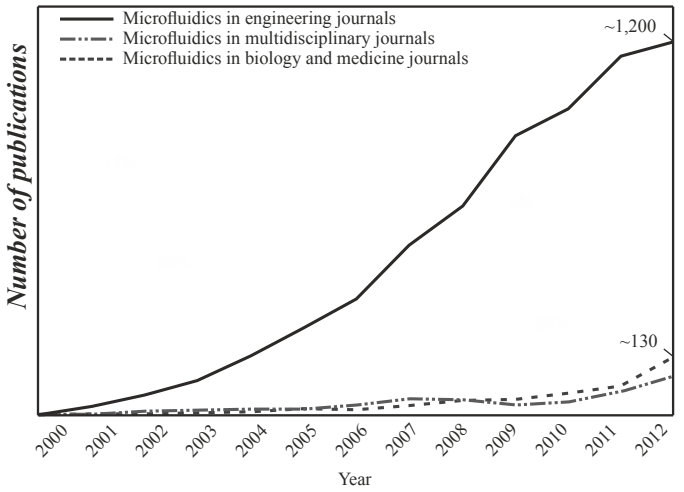

Figure 1.1: Annual number of publications of microfluidics in pear reviewed journals; progression over time. Microfluidics in engineering journals follow a disproportional growth with respects to publications in multidisciplinary, biology and medicine journals. Graph adapted from [1].

forces. These allow for the manipulation of fluids in narrow confinements and for counteracting the gravitational forces. Most importantly, capillarity forces spare the need for pumps, integrated or not, simplifying the operation and the development of the system.

These unique features of microfluidics, in terms of fluid handling, lead to miniaturized devices being very appealing. In particular they allow for small sample volumes and reagent requirements thus reducing valuable processing time and assay costs. Time is reduced through precise control of interactions and concentrations and through ingenious mixing devices especially enhanced in digital microfluidics. [5] These proporties of microfluidics has been employed, in various approaches, in the design and development of the systems presented in this thesis.

While microfluidics have a definite impact on analytical chemistry, their advantages have been more thoroughly explored in biology and biomedicine. It it often quoted that microfluidics has the potential to significantly change the way modern biology is performed [6]. Besides time and cost reduction, microfluidic promise in the field is the potential for moving and performing the measurement instrumentation on the exact location that is needed and more

importantly, the fact that those measurements and tests can be performed by personnel with minimal training. In other words proposed microfluidic systems can lead to what is described as Point of Care (PoC) testing, namely diagnostic tests carried out near the time and place of the patient. This revolutionary new practice leads to a shift of paradigm in traditional medicine, particularly towards a less centralized model, while improving diagnostics and biological research methods.

This progress is unquestionably beneficial for the developing world. Developing world countries often luck access to temperature controlled laboratories and chemical storage rooms, expensive reagents and highly trained personnel; meaning all the necessary infrastructure that contemporary diagnostics require. Proposed and developed lab on a chip systems substantially address those issues providing alternatives to traditional diagnostics and boosting the biomedical capacities of the developing world. [7] A characteristic example is the case of the mChip [8]. MChip is a PoC device that performs ELISA assays [9] on a single chip. The essay is straight forward and user friendly, inexpensive while the reported results are equivalent, in terms of specificity and sensitivity, to those of a modern laboratory. The device was tested on field conditions in Rwanda with sample volumes down to 1 µl. The bacteria and biomolecule detection biosensors developed in this thesis could potentially increase the food and water safety in such environments.

Microfluidic concepts can potentially substitute the most frequently performed laboratory diagnostic processes:

1. Blood chemistry analysis; in particular concentration of red and white cells, electrolytes, gases, lipids, blood enzymes, thyroid indicators, etc.

2. Immunoassays; e.g. the aforementioned ELISA tests, immunoprecipitation.

3. Nucleic acid amplification techniques; namely PCR, etc.

4. Flow cytometry.

5. Culture methods.

Indeed many systems have been proposed that downscale these techniques introducing all the aforementioned advantages [7].

Since the 70s, along with the advance of nanotechnology, a great deal of scientific effort has been focused on the development, synthesis and functionalization of nanoparticles. Nanotechnology provided with solutions to persisting issues in material science, namely material solubility and diffusivity. As far as their *in vivo* administration properties are concerned; improved blood circulation half life, drug release, immunogenicity and lower toxicity are of importance [10]. Undoubtedly, the most important property of nanoparticles is their size; with their characteristic length ranging from 1 to 100 nm. This order of magnitude is comparable to the size of important biological entities such as antibodies, DNA, proteins, etc. [11] This ultra small size along with their important physiochemical properties; large surface to volume ratio, high reactivity and the possibility for functionalization, renders nanoparticles unique materials for applications in diagnostics and therapeutics. Therapeutics utilize their targeted delivery and controlled release modalities, whereas in diagnostics, nanoparticles are employed in detection processes that range from the whole organism (in the case of single bacteria and cells) down to the molecular scale. For instance, they help determine fragments of nucleic acids (e.g. viral DNA), protein biomarkers and even cancerous cells. [12]

Nanoparticles can be roughly classified in two major categories: organic and inorganic. [13] Among them the most important subcategory is the magnetic nanoparticles. Magnetic nanoparticles couple the advantages of nanotechnology, as they were described above, with the unique features of magnetism. In particular, they can be manipulated by externally applied fields which are finely tuned and can be generated by on-chip embedded modules. Another element, important for integrated solutions, is that embedded magnetic sensors can detect the stray field or the relaxation time of the particles, thus determining their concentration, spatial resolution or solely their presence. [14] A last important feature is the intrinsic hysterisis loop of the magnetic nanoparticles that allows for the hyperthermia therapeutic treatment; a method for wireless transfer of thermal energy in such amounts that can cause the lysis of cancerous or other malignant cells. [15] Magnetic nanoparticles have especially revolution-

ized, *in vivo* diagnostics (e.g. Magnetic resonance imaging, MRI) and drug delivery therapies due to the permittivity of living tissue to magnetic fields. Summarizing, well established applications that utilize the features of the magnetic nanoparticles range from magnetic separation and hyperthermia to drug delivery, immunoassays and MRI contrast enhancement agents, [16] while emerging applications include control of cellular functions and whole cells through magnetic actuation, regenerative medicine, tissue engineering and visualization agents for a novel imaging technique called Magnetic Particle Imaging. [17] In the frame of this thesis, magnetic particles were used, in all the proposed systems, for tagging pathogens, biomolecules and cells allowing the manipulation and detection of the resulting compounds.

As stated above, magnetic nanoparticles, in the form of uncompounded particles, agglomerates or encapsulated in a polymer matrix can be detected by magnetic sensors. Especially in biomedicine and biotechnology, magnetic sensors are employed to determine concentrations of biomolecules and cells giving rise to biosensing systems. Most frequently, functionalized nano or microparticles (i.e. encapsulated nanoparticles) are conjugated with immunoassay agents (i.e. antibodies) and that way they capture the biomolecule or cell in question. [18] Then different sensing techniques are utilized to detect and quantify the sample. Of course the sample is suspended in a liquid, thus microfluidics are usually employed to confine the sample and contribute to the repeatability of the study. [19] The main advantages of magnetic biosensors over other biosensing methods is that their integration, using silicon technology processes, is well established and they are much cheaper than other methods such as optical systems, since the later require microscopes and fluorophores or quantum dots. Four different detection methods are commonly used in magnetic biosensing systems:

1. The diagnostic technique of magnetic resonance uses magnetic nanoparticles to modulate the spin-spin interaction and thus the relaxation time among the water protons that surround them. [20]

2. Magnetic particle brownian relaxation sensors use magnetic sensors to determine the relaxation rate of the particles. [21]

3. Magnetoresistive biosensors are used to directly sense the stray field of the magnetic nanoparticles and directly correlate the sensor's output to the concentration. [22]

This last category of magnetic sensors is used in the frame of this thesis.

Summarizing the above, it becomes apparent that proposed and developed microfluidic platforms utilizing magnetic nanoparticles and integrated sensors seek to enhance the capacities of contemporary biology and biomedical research. With many studies focusing on systems that aim to substitute macroscopic tests and assays while still microfluidics remaining an immersing field, most of those studies realize proof-of-concept experiments that aim on demonstrating the validity of an implementation. [23] At the frame of this thesis several systems, ranging from bacteria and antibody detection to cells and circulating tumour cells isolation were proposed, implemented and their concept was experimentally proven.

1.2 Objectives of this work

It was the aim of this thesis to conceptualize, design, implement and optimize lab-on-chip systems combining microfluidics, magnetic nanoparticles and magnetic sensors towards point-of-care devices for diagnostics and, cells and biomolecules analysis systems. The scientific and research objectives of this work, along with the developed systems were:

1. To design, implement and prove the concept of a novel magnetic biosensor for *in vitro* detection of bacteria tagged by magnetic microparticles and suspended in a static fluid. The detection is based on the physical forces exerted on tagged magnetic particles in flow. In particular, the stoke's drag force.

2. During the development of the previous biosensor it was assumed that the same design could be used for an antibody detection system utilizing a different force, i.e. the friction force. Proof of concept experiments were carried out.

3. To design and implement a system for detection and quantification of magnetic nanomarkers used in a wide range of application in therapeutics and diagnostics, such as biomolecule detection, drug delivery, hyperthermia, etc.

4. To design and implement devices for separation and trapping of cells out of liquid samples for further analysis; i.e. drug testing, viability studies, physical properties characterization, etc. Those systems can be also used for the purification and quantification of rare cell, e.g. circulating tumour cells (CTCs). [24]

1.3 Outline of the thesis

This work is presented in the form of a cumulative thesis. The introductory chapter (Chapter 1) leads the reader through the scientific motivation behind this work, briefly apposes the scientific issues dealt with in this thesis, explains basic theoretical considerations and describes the methodology behind the design and implementation of the proposed systems.

The scientific outcome of the presented work follows in the form of self-contained chapters. Each chapter corresponds to scientific articles published in international, peer-reviewed journals. Chapters 2 - 4 denote the progress in the development and optimization of the bacteria biosensor. Chapter 5 presents the antibody biosensor, but maybe most importantly, proposes a novel technique for resolving biomolecules; a technique akin to liquid chromatography. Chapter 6 and 7 present a platform for detecting and quantifying different kinds, commercial or custom synthesised, of magnetic nanomarkers. Lastly, Chapters 8 and 9 investigate the efficacy of the proposed platforms in trapping and detecting cells for further analysis and diagnostic possibilities, such as the purification and quantification of CTCs.

1.4 Theory and Basic concepts

1.4.1 Microfluidics

Microfluidics are the systems that confine fluids and allow/sustain their flow while their characteristic dimension is between 1 to 100 µm. An identifying trait of microfluidic systems is the ratio of the surface area (SA) to volume (V). The importance of this quantity lies on the fact that many important aspects of fluid flow drastically change with the increase of the ratio. [25]

The SA term is proportional to l_c^2 whereas the V term is proportional to l_c^3, where l_c is the characteristic length of the channel. Consequently,

$$\frac{SA}{V} \propto \frac{l_c^2}{l_c^3} = \frac{1}{l_c} \tag{1.1}$$

Equation 1.1 denotes that surface phenomena and viscous effects dominate the flow for large SA/V.

The SA/V ratio consequently leads to another non-dimentional quantity defined as the ratio of inertial forces, conveyed by the momentum of the liquid, over the viscous (or frictional) forces. It is apparent that the SA/V ratio is inversely proportional to this new quantity known as the Reynolds number. The Reynolds number is used to define and characterize fluid flow regimes and is given by the equation: [26]

$$Re = \frac{\rho v l_c}{\eta} \tag{1.2}$$

where ρ is the fluid density, η is the fluid viscosity, l_c is the characteristic length for the flow, and v is the fluid velocity. As the SA/V ratio in microfluidic systems is large, Reynolds number is small, typically $Re \ll 1$. This categorizes the flow in microfluidic channels in the creeping (or Stokes) flow regime. [27]

Other important effects encountered in microfluidics systems and that differ form those in macroscale systems are: [28]

1. entrance effects are often one order of magnitude less than the channel's length. [29]

2. Surface roughness must be taken under consideration during the systems design, as it might be comparable to the characteristic dimensions of the channels and thus can cause perplexing flow profiles at the channel walls.

3. Diffusion is very important for microfluidic systems as it allows the effective mixing of fluids due to the channels' small size, which is comparable to the diffusion length. [30]

4. Capillary effects can be a major flow inducing force in microfluidics.

1.4.2 Magnetic Nanoparticles

Superparamagnetism

With the advantages of magnetic nanoparticles already demonstrated in the previous section (Section 1.1), it is relevant to examine some of their physical properties that render them invaluable to modern biotechnology and medicine. The most important among the physical properties of the magnetic nanoparticles is their superparamagnetic nature.

Magnetism is tracked down to the electronic structure and the electron spin of an atom. Individual atoms exhibit magnetic moments locally due to electron spins that remain uncompensated. [31] Multiple atomic moments with the same direction form a magnetic domain; volumes in bulk materials with the same magnetization. Magnetic domains are formed in order to fulfil the convention for minimized energy. In this case the exchange, the anisotropy and the magnetostatic energy in particular (Table 1.1). [32] The Pauli exclusion principle and the electrostatic coupling between the electrons of the atom cause the exchange interaction, which dominates magnetic ordering in microscopic distances. On the other hand, anisotropy is the interaction of electron orbitals with the potential energy deriving from the structural (crystal) lattice of the material or its shape. The potential energy condenses at areas, in the volume of the material, that coincide with the structure of the crystal lattice. This results into the formation of the easy magnetization axes of the material. These axes coincide with the orientation of the spins that is energetically

Energy term	Coefficient	Definition	Range
Exchange energy	A [J/m]	Material constant	$10^{-12} - 2 \times 10^{-12}$ J/m
Anisotropy energies	$K_s K_c ...$ [J/m^3]	Material constants	$\pm(10^{-12} - 2 \times 10^{-12})$ J/m^3
External field energy	$H_{ex} J_s$ [J/m^3]	H_{ex} = external field, J_s =saturation magnetization	open depending on field magnitude
Stray field energy	K_d [J/m^3]	$K_d = \frac{J_s^2}{2\mu_0}$	$0 - 3 \times 10^6$ J/m^3
External stress energy	$\sigma_{ex}\lambda$ [J/m^3]	σ_{ex} = external stress, λ = magnetostriction constant	open depending on stress magnitude
Magnetostrictive self energy	$C\lambda^2$ [J/m^3]	C =shear modulus	$0 - 10^3$ J/m^3

Table 1.1: The energy terms in a magnetic material.

favoured. While exchange interaction dominates short-range alignment of atomic moments, anisotropy defines their orientation along an easy magnetization axis. [33] Once these two factors are balanced the minimization of the long range magnetostatic energy becomes relevant. By that is meant the principle of avoidance of the formation of magnetic poles. Thus the magnetic lines closure is achieved in the material itself and the magnetostatic energy is minimal. This is expressed by the divergence of the magnetization being equal to zero: [34]

$$\nabla \vec{\mathbf{M}} = 0 \tag{1.3}$$

In this minimal energy arrangement, the energy is condensed on the domain walls; the areas of magnetic domain transition. [35] Scal-

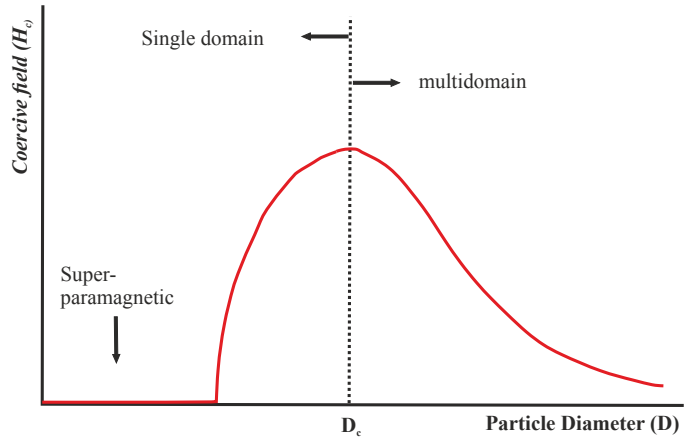

Figure 1.2: Qualitative graph of the change in the coercive field (H_c) of magnetic particles with respect to the particle size. Illustration adapted from [36].

ing down from bulk materials to single particles the magnetocrystalline anisotropy of the material is reduced to one easy axis, while the shape anisotropy vanishes. As a result the formation of multiple domains and their domain walls is energetically unfavoured. Thus there is a critical size where the formation of single domain particles is reported. [36]. Zooming in the material we can visualize the magnetic domains, now, as single atomic moments. Scaling even more down the size of the particles, the fluctuations due to the thermal energy become dominant, even in temperatures lower than the curie temperature. Thus no magnetic ordering, in the absence of external magnetic fields, can be observed. These particles are called superparamagnetic particles. Figure 1.2 shows this transition of the particles magnetism versus their size.

Supeparamagnetism is characterized mainly by two manifestations. Firstly, it exhibits a sigmoid magnetization curve without hysteresis. Secondly the magnetization M versus the H/T plots must superimpose independently of temperature, as shown in Figure 1.3.

The mechanism behind superparamagnetism is based on the net magnetization relaxation time given by the equation:

$$\tau = \tau_0 exp\left(\frac{\Delta E}{k_B T}\right) \tag{1.4}$$

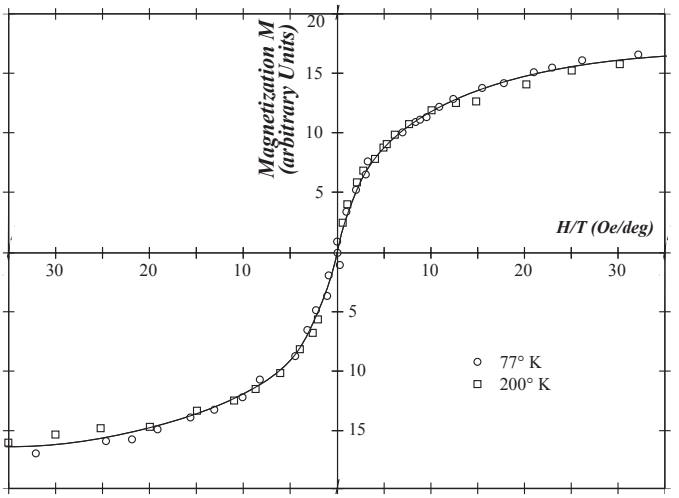

Figure 1.3: Magnetization curve of superparamagnetic iron amalgam with respect of the change of the H/T ratio. Graph adapted from [37].

where ΔE is the energy barrier to the moment reversal, and $k_B T$ is the thermal energy. For noninteracting (with each other) particles the factor τ_0 is of the order of $10^{-10} - 10^{-12}$ sec and only weakly dependent on temperature. [38] The energy barrier, having its origin in the intrinsic magnetocrystalline and the extrinsic shape anisotropy is, in its simplest form, equal to the product of the anisotropy energy density (K in $\mathrm{J/m^3}$) with the volume. It is, in room temperature, comparable to the thermal energy. The relaxation time of the net magnetization corresponds to the time needed until the loss of magnetic ordering of the atomic moments. That said superparamagnetism is a matter of reference, with the reference being, in each occasion, the mean experimental time. In other words, when the magnetization relaxation time is an order of magnitude smaller than the time the experimental arrangement requires the net magnetization to be lost, we witness superparamagnetic behaviour.

Particle functionalization

Besides their size, the property that renders nanoparticles indispensable in contemporary diagnostics and therapeutics is their potential to be multifunctionalized with different functional groups thus combining different effects in the same compound (Figure 1.4). [13] For

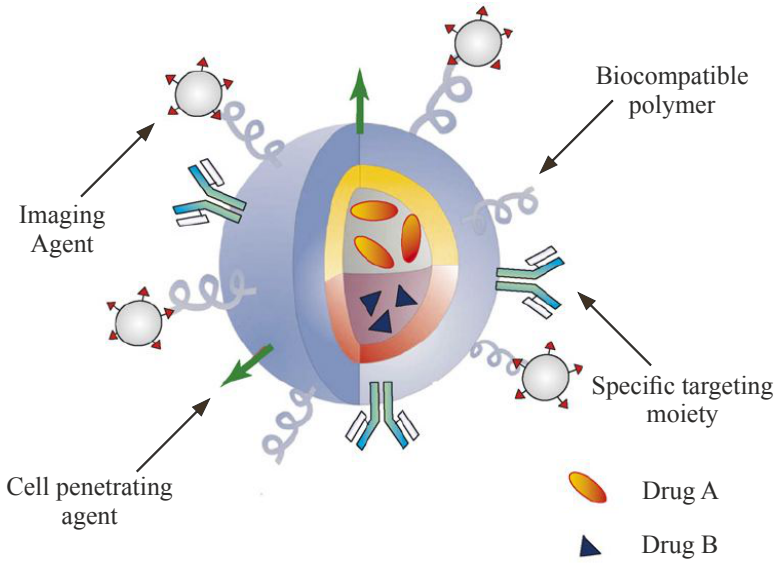

Figure 1.4: Drug delivery and imaging enhancement utilizing multifunctional nanoparticles. Specific targeting agents (typically antibodies or peptides) deliver the drug where is needed and provide information about the spatial distribution of the targeted biomolecule. Cell penetrating agents are employed for drug delivery in the cytoplasm and the biocompatible polymer as a stabilizing agent. Figure adapted from [13].

example magnetic nanoparticles, providing separation modalities, are further functionalized with polymers (e.g. PEG) to stabilize their suspensions. Furthermore biomolecules (e.g. streptavidin, antibodies etc.) can be immobilized on the polymer's surface allowing the capture of other biomolecules (e.g. biotin in the case of streptavidin) or even whole organisms (e.g. bacteria in the case of antibodies). A list of different modalities achieved with different functionalizations is shown in Table 1.2

There are two main strategies for fictionalizing nanoparticles. [39] The first approach is towards a one-step functionalization where a bifunctional molecule is conjugated with the nanoparticle. The ligand, that is then exposed on the surface of the nanoparticle, exhibits high affinity to the targeted molecule. The other approach uses a chelating agent between the nanoparticle and the functionalization ligand. The resulting structure can be defined as nanoparticle - chelating

Properties	Benefits	Function
Stability, biocompatibility	Maintain drug levels in the blood, therefore improving specificity	Polyethylene glycol, phospholipid micelles, polypeptides
Specific targeting	Increase efficiency, reduce toxicity	Antibodies, peptides, carbohydrate, folic acid
Intercellular penetration	Modify nanoparticle biodistribution, increase efficacy	Peptides, ligants, positively charged moieties
Imaging	Report real time nanoparticle biodistribution	Quantum dots, magnetic nanoparticles
Stimulus sensitive drug release	Control bioavailability, reduces toxicity	Photosensitive, thermosensitive, redox sensitive

Table 1.2: A summary of strategies for the construction of multifunctional nanoparticles.

agent - functional group. The chelating agent is a compound whose molecules bind to metal ions. [40]

In this thesis, a wide range of functionalized magnetic particles was used. Different for each system, depending on the application, the targeted biomolecule or biological entity and the materials used in the system's fabrication. More informations are presented in each chapter.

1.4.3 Giant Magnetoresistance sensors

Beyond microfluidics and nanoparticles, the other technology employed in the development of the proposed systems, is magnetic sensors technology. In particular sensors that can be integrated on microfluidic platforms and sense the stray field of magnetic nanoparti-

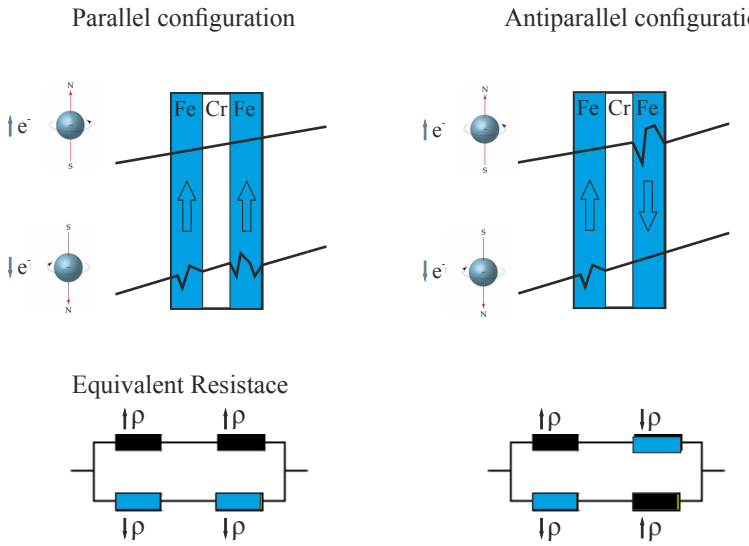

Figure 1.5: The two configurations of the basic Giant Magnetoresistance trilayer structure. In the parallel one, the configuration exhibits lower resistance because the spin up electrons encounter lower resistance, while in the antiparallel configuration the structure impedes both electron spicies (spin up and spin down) resulting to a higher resistance. The blue color denotes higher resistance whereas the black, lower resistance. Illustration adapted from [43].

cles. Undoubtedly, ideal candidates are the Giant Magnetoresistance (GMR) spin valve sensors.

Giant Magnetoresistance

Giant Magnetoresistance was discovered in the 80s by A. Fert [41] and P. Gruenberg [42]. They independently reported the variation of resistance with a changing magnetic field. This variation was reported in multilayer thin films consisting of two ferromagnetic layers and a conducting spacer in between. It was correlated to the alignment of the magnetizations of the ferromagnetic layers. The reason for the change in resistance is attributed to the quantum effect of electron spin material magnetization interaction that results in scattering and leads to significantly diverse conductivities for spin up and spin down electrons. Figure 1.5 graphically underlines this effect.

Spin Valves (SVs)

The GMR effect has been reposted in many thin film multilayer structures raising the interest for the integration of these stacks in on-chip sensing applications. The small thickness of the materials is dictated by the spontaneous antiparallel magnetization alignment in sequentially deposited thin film ferromagnetic layers with a conductive spacer in between.

Initial studies were conducted on antiferromagnetically coupled layers. These coupled layers exhibit a high lower detection limit (LDL) because the external field must cancel out the coupling field. Another proposed structure was the double coercivity structure. [44]Those structures are susceptible to the hysteresis of the ferromagnetic material.

These problems were addressed by another structure, the GMR Spin valves. The difference with the originally proposed arrangement of A. Fert and P. Gruenberg lies on the fact that one of the ferro-

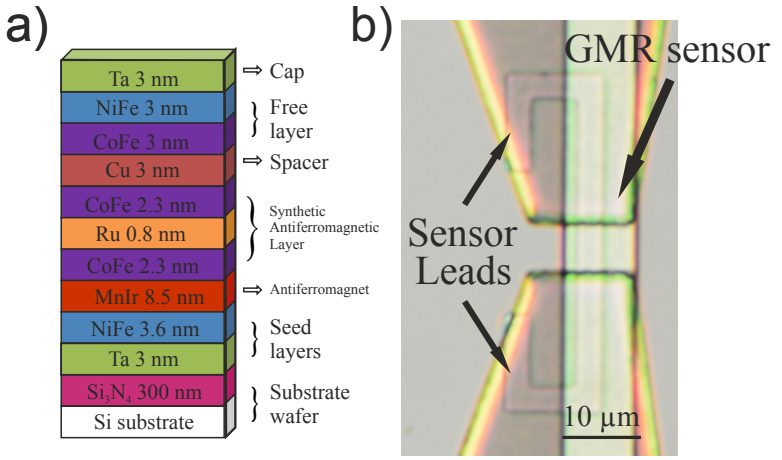

Figure 1.6: (a) Typical spin valve multilayer structure (bottom up): The wafer substrate, the seed layers, the antiferromagnet (pinning layer), the synthetic antiferromagnetic layer (SAF) or pinned layer, the conducting spacer, the free layer and the cap. Similar stuck has been eployed in the frame of this thesis. (b) microscope image under 50x magnification of an integrated spin valve sensor with its contact leads and a gold microconductor on the top produced by INESC-MN and TU Wien (Institute of Sensor and Actuator Systems).

magnetic layers' magnetization is free to rotate, whereas the other's is pinned. In its most simple implementation, this is done by an antiferromagnetic layer through the exchange interaction of the neighbouring atomic moments. With a weak coupling between the two ferromagnetic layers, the sensitivity of the sensor is greater. Buffer layers (usually NiFeCr alloys) have greatly enhanced the quality of the structure. The pinned ferromagnetic layer has become more magnetically stable through the introduction of the synthetic antiferromagnetic (SAF) pinned layer. This is typically comprised of a very thin (less than 1 nm thick) Ru layer deposited between two ferromagnetic layers. The thin Ru layer allows the antiferromagnetic coupling of the ferromagnetic layers. The resulting antiparallel magnetization of the ferromagnetic layers, minimizes the magnetostatic energy and the stray field compared to a single antiferromagnetic layer, thus reduces the lower detectable field. A typical spin valve stack with the synthetic antiferromagnetic layer, fabricated for the needs of this thesis, is shown in figure 1.6.

In order to obtain a linear sensor output a uniform magnetic field is simultaneously applied during the deposition. As a result the free and pinned ferromagnetic layers have a resulting net magnetization with a relative angle of 90°. That way, hysteresis is significantly reduced. The voltage output of a SV sensor with this stack structure is given by: [43]

$$\Delta V = \frac{1}{2}\frac{\Delta R}{R} R_0 \frac{IW}{h} \cos(\theta_f - \theta_p) \tag{1.5}$$

where $\Delta R/R$ is the maximum magnetoresistance level (5 - 20%), R_0 is the sensor's sheet resistance (15 - 20 Ω/m^2), W is its width, h is the thickness, I is the current flowing through the sensor, and θ_f and θ_p are the angle of the magnetization of the free and the pinned layer respectively (Figure 1.7). Assuming uniform magnetization for the free and pinned layers, for a linearised sensor output, $\theta_p = \pi/2$ and $\theta_f = 0$.

1.4.4 Magnetic fields and magnetophoretic force

The developed biosensors, in the frame of this thesis, utilize the magnetically induced motion of magnetic micro and nanoparticles for

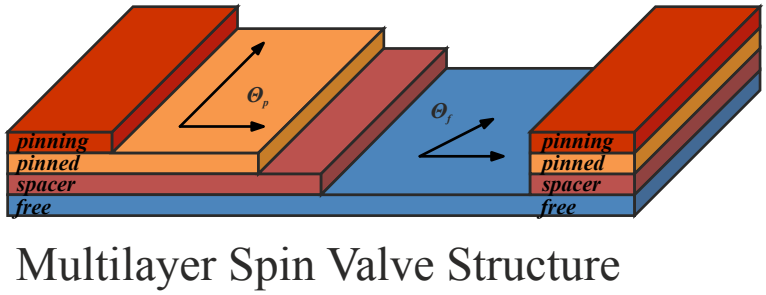

Figure 1.7: Simplified Giant magnetoresistance spin valve structure. Where θ_f and θ_p denote the angle of the magnetization of the free and the pinned layer respectively. Illustration adapted from [43]

converting (transducing) the presence of a specific analyte to an electric signal. This motion is caused by magnetic field gradients generated by integrated microconductors.

Maxwell equations

Magnetic fields generated by a current supplied conductor are accurately described by the Maxwell equations, summarized as follows: [45]

$$\nabla \cdot \vec{\mathbf{E}} = \frac{1}{\varepsilon_0}\rho \tag{1.6}$$

$$\nabla \cdot \vec{\mathbf{B}} = 0 \tag{1.7}$$

$$\nabla \times \vec{\mathbf{E}} = -\frac{\partial \mathbf{B}}{\partial t} \tag{1.8}$$

$$\nabla \times \vec{\mathbf{B}} = \mu_0 \vec{\mathbf{J}} + \mu_0 \varepsilon_0 \frac{\partial \mathbf{E}}{\partial t} \tag{1.9}$$

Proposed by Maxwell in 1896 these equations are a sufficient and systematic representation of classical electrodynamics. Except for very specific symmetrical problems, there isn't an analytical solution to these differential equations, nevertheless, approximations exist. Biot-Savart law, for instance, provides an acceptable approximation of the magnetic field generated by a current carrying conductor. The

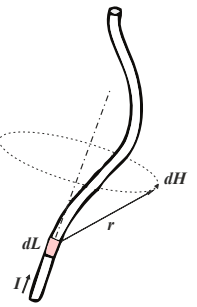

Figure 1.8: The figure shows the magnetic field ($d\mathbf{H}$) generated at a point P by an element of the current carrying conductor ($d\mathbf{L}$). I is the current's magnitude.

magnetic field intensity $d\mathbf{H}$ at a distance $\mathbf{r}$ from a segment $d\mathbf{L}$ of an arbitrarily shaped conductor carrying current I is calculated by the Biot-Savart law by Equation 1.10 (Figure 1.8):

$$d\mathbf{H} = \frac{1}{4\pi r^2} I d\mathbf{L} \times \hat{\mathbf{r}} \tag{1.10}$$

The magnetic field produced by current flow in a conductor is perpendicular to it and follows the right hand rule. Approximations are provided by the finite element method (FEM) as well; an approach discussed below in this chapter.

Magnetophoresis

Magnetophoresis is the process of manipulating soft magnetic material in a medium, utilizing magnetic fields. The magnetic force is caused by magnetic field gradients. Magnetic force is zero in homogeneous magnetic fields and depends on the magnetic field density ($\mathbf{B}$), it's gradient ($\nabla \cdot \mathbf{B}$) and the difference between the susceptibilities of the magnetic material and the medium surrounding it. It is described by the equation: [46]

$$\vec{\mathbf{F}} = \frac{V \Delta\chi}{\mu_0} (\vec{\mathbf{B}} \cdot \nabla) \vec{\mathbf{B}} \tag{1.11}$$

where V is the volume and μ_0 is the permeability of the vacuum ($\mu_0 = 1.257 \times 10^{-6}\,\mathrm{H/m}$). Equation 1.11 denotes that the application of forces larger than a few pN on superparamagnetic nanoparticles

can be challenging. [47]This is due to the very small volume. What is important to the manipulation of particles of that size is that the potential energy of the particle due to the magnetic field must be greater than the thermal energy. In such a system the thermal energy is identified with the mechanical kinetic energy and is observed in the Brownian motion of the particle. This is expressed in Equation 1.12:

$$\mid U \mid = m \cdot B = -\frac{\chi B^2 V}{\mu_0} \gg \frac{3}{2} kT \tag{1.12}$$

where U is the potential energy, m is the magnetic moment, B is the applied field and k is the Boltzman constant and T is the temperature in degrees Kelvin.

Moreover every body in suspension, moving in a liquid is subjected to a viscus, frictional in nature, drag force. It is given by Equation 1.13:

$$\vec{\mathbf{F}}_d = -3\pi D \eta \vec{\mathbf{v}} \tag{1.13}$$

where D is the diameter of the suspended body, η is the viscosity of the medium, and $\mathbf{v}$ is the relative velocity of the fluid with respect to the body. The equation only applies to spherical particles and there are several corrections proposed for different shapes. These corrections are reviewed in the following chapters. The Stokes drag is applicable to the creeping flow regime (Stokes regime) with small Reynolds numbers ($Re \ll 1$).

Nevertheless, the integration of microconductors, on-chip, induces sharp magnetic field gradients that allow the manipulation of the nanoparticles in a liquid medium, overcoming both the thermal Brownian motion and the Stoke's drag force.

Nanoparticle magnetization and stray field

The magnetic state of any object susceptible to magnetic fields is denoted by its magnetization. For single domain magnetic particles it is given by the equation [48]:

$$\vec{\mathbf{M}} = M_s \hat{\mathbf{m}} \tag{1.14}$$

where M_s is the saturation magnetization, which is an intrinsic property of the material and $\hat{\mathbf{m}}$ is the normalized vector of the magnetic moment's direction. When an external magnetic field $\mathbf{H}_{eff}$ is exerted on a bulk material, every individual atomic moment vector transposes towards the $\mathbf{H}_{eff}$'s direction following a spiral like trajectory (Figure 1.9). This is accurately described by the Landau-Liftshitz-Gilbert-Langevin equation with spin-torques:

$$\frac{\partial \hat{\mathbf{m}}}{\partial t} - \alpha \hat{\mathbf{m}} \times \frac{\partial \hat{\mathbf{m}}}{\partial t} = \gamma \hat{\mathbf{m}} \times \vec{\mathbf{H}}_{eff} \tag{1.15}$$

where α summarizes the damping mechanisms and γ is the gyromagnetic ratio. $\mathbf{H}_{eff}$ comprises of four terms:

$$\vec{\mathbf{H}}_{eff} = -\frac{2A}{\mu_0 M_s}(\nabla \hat{\mathbf{m}})^2 + \frac{\partial f_{ani}(\hat{\mathbf{m}})}{\partial \hat{\mathbf{m}}} + \vec{\mathbf{H}}_{demag} + \vec{\mathbf{H}}_{ext} \tag{1.16}$$

The first two summands denote the short term exchange or coupling interaction and the shape anisotropy respectively. As it is already shown in Section 1.4.2, below a critical length of approximately 100 nm the magnetic nanoparticles are uniformly magnetized, thus the spacial derivatives of the direction of magnetization ($\hat{\mathbf{m}}$)) can be ignored. $\mathbf{H}_{demag}$ can be obtained through the gradient of the scalar magnetic potential. The later can be calculated by solving the Laplace-Poisson inhomogeneous equation:

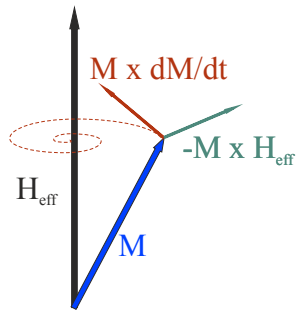

Figure 1.9: The vector analysis of the Landau-Lifshitz-Gilbert equation in the special case that the the $\mathbf{H}_{eff}$ field is constant: the precession is denoted with green color and the damping with red color, the magnetization **M** with blue color and its trajectory with a red dotted spiral.

$$\vec{\mathbf{H}}_{demag} = -\nabla\phi_{mag} \tag{1.17}$$

$$\Delta\phi_{mag} = \nabla\vec{\mathbf{M}} \tag{1.18}$$

where Δ is the Laplace operator. Yet, in the case of a uniformly magnetized sphere, the demagnetizing field is constant, equal to: $\mathbf{H}_{demag} = -1/3\mathbf{M}$ and antiparallel to the magnetization's direction. [49] Thus when substituting Equation 1.16 in Equation 1.15 the term $\mathbf{H}_{demag} \times \mathbf{M} = 0$. Taking that into consideration the $\mathbf{H}_{eff}$ (Equation 1.16) is limited to the stray field of the magnetic nanoparticle given by: [50]

$$\vec{\mathbf{H}}_{ex} = \frac{M_s V}{4\mu_0}\left(\frac{(\vec{\mathbf{r}}\cdot\hat{\mathbf{m}})\vec{\mathbf{r}}}{r^5} - \frac{\hat{\mathbf{m}}}{r^3}\right) \tag{1.19}$$

It is apparent that Equation 1.15 no longer has spatial derivatives and the partial differential equation resolves to an ordinary differential equation. In this thesis, among others magnetic nanopartilces, encapsulated into a polymer matrix forming beads, where used. This case can be considered as a system of finite particles (N). Equation 1.15 forms a systems of ordinary differential equations, writen in a matrix form as follows:

$$(Id - \alpha M)\frac{d\hat{\mathbf{m}}}{dt} = \gamma M\vec{\mathbf{H}}_{eff} \tag{1.20}$$

where Id is the identity matrix and M is the block diagonal matrix of the particles' magnetization:

$$M = \begin{pmatrix} M_1 & & \\ & \ddots & \\ & & M_N \end{pmatrix}, M_n = \epsilon_{ijk}\hat{\mathbf{m}}_{n,j}$$

$$n = 1, ..., N$$

$$\frac{d\hat{\mathbf{m}}}{dt} = \frac{d}{dt}(\hat{m}_{x,1}, \hat{m}_{y,1}, \hat{m}_{z,1}, \hat{m}_{x,2}, ...)^T$$

$$\vec{\mathbf{H}}_{eff} = (H_{eff,x,1}, H_{eff,y,1}, H_{eff,z,1}, H_{eff,x,2}, ...)^T$$

1.4.5 Flow in microfluidic channels

Navier-Stokes Differential Equation

Liquid fluids are considered continuous matter at distances less than 0.3 nm. Thus, for Lab-on-chip applications where the critical length is of the order of µm, the hypothesis holds. Continuous matter liquids in microchannels can be approached in terms of fields or in other words with spatial differential and dynamic equations. This system of partial differential equations were first introduced by Navier and Stokes and is describing an Eulerian velocity field $\mathbf{v}(r,t)$. The Navier-Stokes equations stems from the Newton's second law of motion: [51]

$$m\frac{d\mathbf{v}}{dt} = \sum_j \vec{\mathbf{F}}_j \tag{1.21}$$

In fluids, it is more convenient to work with densities. Thus dividing both sides of the equation with the volume we get the density and the force densities. For acquiring a more physical accurately equation, we substitute the time derivative with the so called material-time derivative. Equation 1.21 becomes:

$$\rho D_t \mathbf{v} = \sum_j \vec{\mathbf{F}}_j \tag{1.22}$$

with D_t being: [52]

$$D_t = \frac{\partial}{\partial t} + (\vec{\mathbf{v}} \cdot \nabla) \tag{1.23}$$

As far as the driving forces of the motion is concerned, we can divide them into three groups:

1. Body forces, acting throughout the body of the fluid, consist of mainly gravitational and electrostatic forces.
2. Frictional forces, due to the viscous nature of the fluid.
3. The pressure gradient force.

The final form of the Navier-Stokes equation for incompressible fluids is:

$$\rho\left(\frac{\partial \mathbf{v}}{\partial t}+(\vec{\mathbf{v}}\cdot\nabla)\vec{\mathbf{v}}\right)=-\nabla p+\eta\nabla^2\vec{\mathbf{v}}+\rho g+\rho_{el}\vec{\mathbf{E}} \tag{1.24}$$

The right side of the equation represents the force densities and in particular, the first term the pressure gradient force density, the second the viscous force density, the gravitational force density and the electrical force density are represented in the third and forth term respectively.

Creeping flow

The Navier-Stokes equation is very challenging to solve, both analytically and numerically. Yet, flow in microfluidic channels has some peculiarities that significantly simplify the initial equation. First, the gravity driven pressure is negligible and can be omitted. This become apparent when the pressure due to gravity in a microfluidic channel is calculated. The change in pressure due to gravity is given by:

$$\nabla p=\rho_\infty g \Rightarrow \frac{dp}{dy}=\rho_\infty g \Rightarrow p_{max}=\rho_\infty g h \tag{1.25}$$

But the hight of a microfluidic channel is usually between 10 to 100 μm. Thus the maximum pressure of water ($\rho = 1000\,\mathrm{kg/m^3}$) in a microfluidic channel is between 9.81×10^{-2} to 9.81×10^{-1} Pa which is negligible.

Other effects that modify the Navier-stokes equation and define the velocity field in microfluidics is the assumption that the material and the time derivative (for steady flow) of the velocity field is considered negligible. [53]. Thus Equation 1.24 is simplified to the Poisson equation: where driving pressure and friction force at the interface of the liquid with the channel walls are balanced.

$$\rho\left(\cancel{\frac{\partial \mathbf{v}}{\partial t}}+\cancel{(\vec{\mathbf{v}}\cdot\nabla)\vec{\mathbf{v}}}\right)=-\nabla p+\eta\nabla^2\vec{\mathbf{v}}+\cancel{\rho g}$$

$$\nabla p=\eta\nabla^2\vec{\mathbf{v}} \tag{1.26}$$

It is obvious that this simplified version of the Navier-Stokes equation is much more easier to solve and acquire the velocity field, when the pressure is given. The flow regime governed by the Poisson equation is the creeping flow regime for $Re \ll 1$.

1.4.6 Surface phenomena

Capillary effects and surface tension

Two of the most important features of microfluidics are the capillary effects and the surface tension. The first, mainly because it allows the motion of fluids without the need for pumping mechanisms, while the second defines the electrostatic interaction between water molecules and the chip's surface. Furthermore, surface tension is the causative of the capillary effects. Notions like the contact angle and hydrophilicity are interconnected with the surface tension as well.

The surface tension at the interface of two media is originating from the higher energy of the surface molecules with respect to the molecules in the bulk medium. That is because the later have all the possible chemical bonds formed with their neighbouring molecules (Figure 1.10 (a)) while the surface molecules have some of them missing. This leads to a less energetically favourable state. Surface tension is defined by the Gibbs free energy (G) over the area of the surface (A) for given temperature and pressure: [51]

$$\gamma = \left(\frac{\partial G}{\partial A}\right)_{p,T} \tag{1.27}$$

Figure 1.10 is graphically illustrating the surface tension at the interface between the liquid and the gas phase of a substance. The surface molecules remain at higher energy state, because due to the scarcity and the high kinetic energy of the gas molecules they cannot easily form bonds. This is different in the case of the interface between a solid surface and a polar liquid, such as water. The charged molecules of the surface (due to the missing bonds) give rise to coulomb electrostatic attractive interactions with the polar water molecules and they form hydrogen bonds [54]. That results to a low energy state but also to the wetting of the surface. Such surfaces,

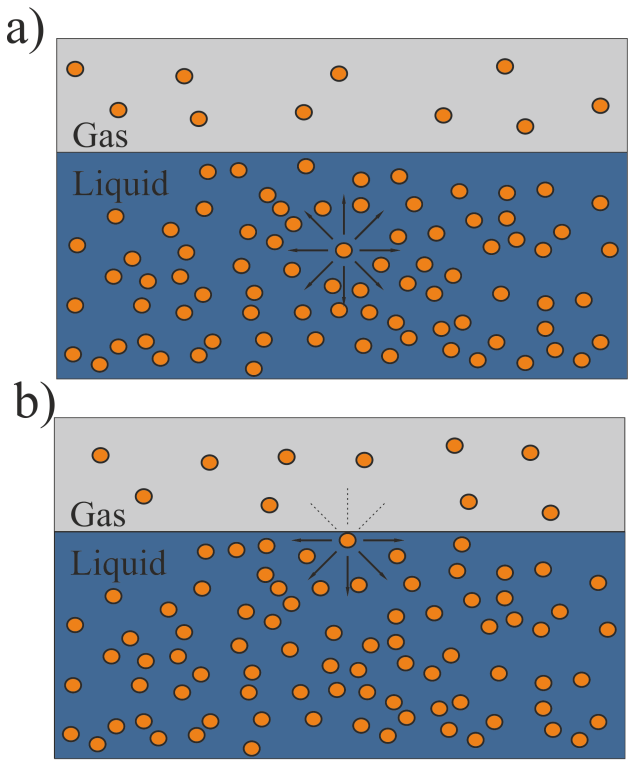

Figure 1.10: Surface tension at the interface between a gas and a liquid substance. The arrows illustrate the hydrogen bonds of the liquid molecule with its neighboring molecules and the corresponding forces exerted on it. (a) shows a molecule in the bulk liquid substance whereas (b) shows the molecules at the interface are pulled towards the bulk of the material. This is due to the absence of hydrogen bonds at the molecule's side that faces the gas. This is due to the scarcity of molecules in the gas phase of a substance.

with high Gibbs free energy per area, exhibit effects like the capillary priming, [55] the capillary channel wall rising and others.

Hydrophilic and hydrophobic surfaces

Water is an extraordinary molecule, whose properties are not yet fully understood and its charge distribution in space is not exactly defined by the proposed models. These models cannot properly explain the properties of the water molecule in all phases. One of the

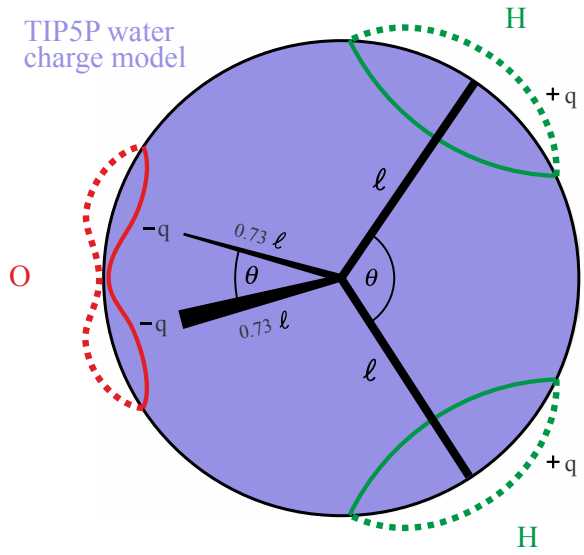

Figure 1.11: One of the over 30 proposed models for the water molecule charge spatial distribution. In the TIP5P model, charges are placed on tetrahedral arms. The specific model can account for the dielectric constant and the density at 4 °C, but not predict the expansion coefficient. Illustration adapted from [56].

more than 30 proposed models is shown in Figure 1.11. Much of water's peculiarities account on the hydrogen bonds formed between its hydrogen atoms. The hydrogen bond, an amalgam between the covalent and the ionic bond, can mediate the bonding of two electronegative atoms due to the small size of the hydrogen atoms involved. Among others, the importance of the hydrogen bond lies on the fact that it denotes the capacity of a surface to bind with the water molecules, leading to its wetting. This capacity distinguishes the characterization of a surface between hydrophilic and hydrophobic. Throughout the course of this thesis the hydrophilic or the hydrophobic property of a surface has been widely employed in order to facilitate the microfluidic channel priming (filling) or to prevent the adhesion of biomolecules.

Water molecules have the strong tendency to form hydrogen bonds with neighbouring water molecules, this largely defines the interaction of water with matter, that be other molecules or surfaces. The most energetically favourable configuration is the one that all

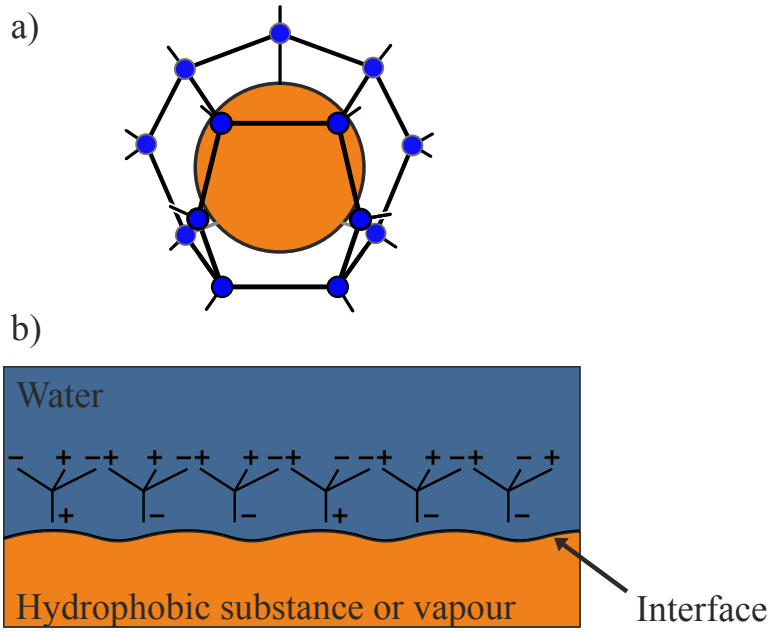

Figure 1.12: (a)Clathrate cages [57] formed around (Hydrophobic) non polar molecules. (b) Water structure at the interface with a hydrophobic substance or air vapour. In order to form the maximum allowed number of three hydrogen bonds, the water molecules become more ordered. In this structure they point either the negative or the positive charge towards the hydrophobic surface.

four charges of a water molecule (as shown in Figure 1.11) form hydrogen bonds with the neighbouring molecules. However, there are molecules such as hydrocarbons, fluorocarbons or inert air bubbles, that do not form hydrogen bonds. When water molecules interact with those substances they have to either sacrifice some of the hydrogen bonds or rearrange the bond angles in order to accommodate the hydrophobic molecule in the formed cavity. This can be achieved when the hydrophobic molecule is small enough. Such a arrangement as it is shown in Figure 1.12 (a) is not always possible. In those cases, the water molecules have to give up one or more of its hydrogen bonds leading to higher energy states. Clearly, the optimal structure is the one where each water molecule points the least number of charges towards the hydrophobic substance. In the case of water being in contact with a hydrophobic surface, the most ener-

getically favourable arrangement is the one where the least number of molecules are in contact to the surface. Thus a bubble-like droplet is formed on the surface with a large contact angle. Contact angle is the measure of the hydrophobicity of a surface. where greater hydrophobicity leads to greater contact angles. Figure 1.13 shows a SiO_2 surface before and after its modification with a perfluoroxisilane (fluorocarbon group) monolayer. Such a hydrophobic surface prevents the adhesion of hydrophilic substances, as their inclination to form hydrogen bonds favours the bonding with water molecules than with the molecules of the hydrophobic surface. For this reason such a surface was employed in the development of a biosensing systems in the framework of this thesis.

The hydrophilic effect, as suspected, describes the inclination of a substance to form hydrogen bonds with water molecules, or in other words the solubility of the substance in water. Another result of the hydrophilic effect is the strong repulsion of hydrophilic surfaces in water, as they tend to bind to water molecules rather than to each other. A special category of hydrophilic polymers or algae absorb large quantities of water, forming hydrogels. Hydrogels have been employed in the frame of this thesis as an anti-sticktion and lubricating agent. More details are presented in chapter 5. At this point it is worth to note that not every polar liquid is hydrophilic and that not every non-polar liquid is hydrophobic. Some hydrophilic and hydrophobic examples of polar and non-polar liquids are shown in Table 1.3.

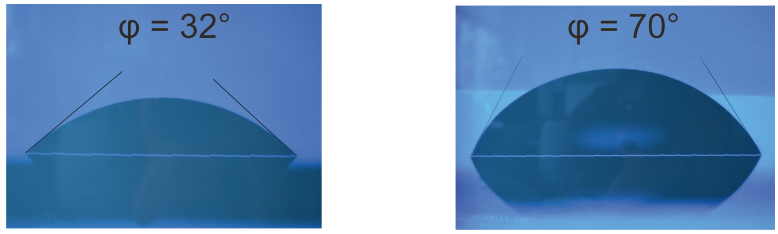

Figure 1.13: Contact angle measurements before (a) and after (b) the surface modification by grafting a fluoropolymer monolayer on the plasma treated surface; before the surface modification the SiO_2 surface yields a contact angle of 32° while after the surface modification it yields a contact angle of 70°.

Molecules and ions	Alcohols, sugars, chaotropes (urea), polyethylene oxide, polyelectrolytes, soluble proteins, nucleic acids, Na^+, Li^+, Mg^{2+}
Molecular groups	Carboxylate, sulfonate,sulfate, phosphate ester
Zwitterionic	Phosphatidylcholine (lecithin)
Cationic	Trimethyl ammonium, dimethyl ammonium
Polar (nonionic)	Amine, amine oxide, sulfoxide, phosphine oxide
Solid surfaces	Hydroxylated silica, swelling clays, chromium, gold
Hydrophobic (polar groups) (when attached to a long hydrocarbon chain)	Alcohol, ether, mercaptan, amines, amide, nitroalkanesm aldehyde, ketone

Table 1.3: Hydrophilic and hydrophobic groups and surfaces.

Surface and frictional forces

Surface and frictional forces play an important role in the development of the proposed bioMEMS. In particular the proposed systems employ the magnetically induced motion of magnetic particles for biotechnological applications. This motion, as it is explained in details in the following chapters, brings the particles in contact with the surface of the chip. At the interface, complicated forces are exerted on the particle and widely vary depending on the structure of the surfaces that are in contact. The surface and frictional forces exerted are discussed in detail for each microsystem in the corresponding chapter.

1.4.7 Finite element method (FEM)

As it was shown in this chapter the physics that govern the operation of the developed microfluidic platforms is governed by complicated differential equation:

1. The Maxwell equations for the magnetic fields.
2. The Navier-Stokes equation for the flow velocity.
3. The Newton second law of motion for the magnetic particle trajectories, while a magnetic force and a drag force are exerted on them.

The analytical solution of this system of partial differential equations, with the exceptions of very symmetrical geometries, does not exist. Nevertheless, there exist mathematical tools, that can circumvent this problems and can provide approximate solutions to the equations. The most widely used approach is the Finite Element

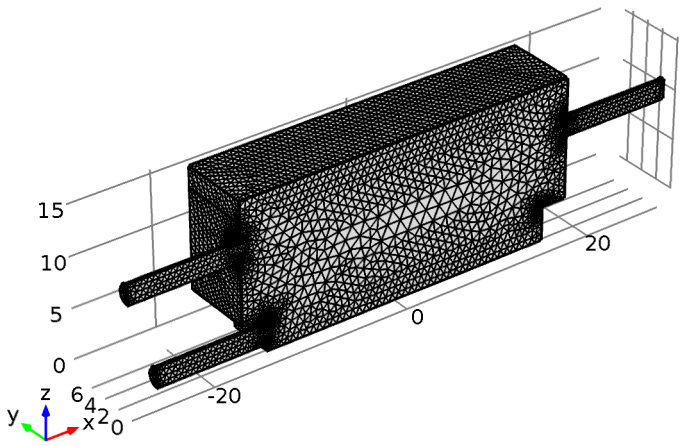

Figure 1.14: Half section of a glass chamber model discretized utilizing a fine predefined mesh in COMSOL® Multiphysics.

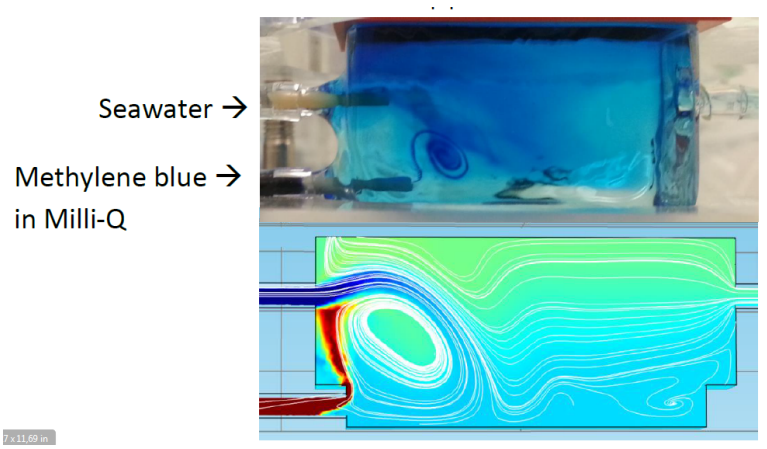

Figure 1.15: Solution of the Navier-stokes equations for the velocity field; Velocity magnitude profile and streamlines. Comparison with the real chamber and under the same conditions of flow and concentrations.

Method analysis (FEM) which is using discretization of the continuous problem and applies a set of boundary conditions.

In particular, the FEM lies on the transformation of a continuous problem into a fragmented one (discretization). Thus instead of solving continually the problem over the whole domain, a matrix problem is formulated consisting of an infinitesimally small network of nodes and links that form a mesh (Figure 1.14). This matrix is then solved by special algorithms mainly based on the Galerkin approximation. [58] The Galerkin method approaches the problem by trying to zero the integral of the product between the residual ($R(x)$ for one dimensional problems) and a weight function ($\psi_j(x)$). In other terms, the method tries to minimize the error of the approximation. This is achieved by fitting trial functions into the initial partial differential equations. Those trial functions are well defined for each set of PDE (e.g. Maxwell equations) and the residue is the resulting error. The weight functions are polynomial functions especially chosen for minimizing the error. The Galerkin method integral is shown in Equation 1.28.

$$\int_{Domain} R(x)\psi_j(x)dx = 0 \tag{1.28}$$

The FEM has been made widely accessible by commercial simu-

lation programs such as COMSOL® and ANSYS®. A sample model realized in COMSOL® is shown in Figure 1.15 In the frame of this thesis finite element analysis has been extensively employed to simulate the magnetic fields that exert the magnetic force on the particles, the flow in the microfluidic channel and the resulting trajectories of the particles. The models where realized in the COMSOL® suit and have been invaluable for providing information of a working device in terms of conductor and channel dimensions, supplied currents as well as informations over the magnitude of the particles' stray field on the sensor. The resulting particle trajectories were finally, simulated for each configuration.

Bibliography

[1] E. K. Sackmann, A. L. Fulton, and D. J. Beebe, "The present and future role of microfluidics in biomedical research," *Nature*, vol. 507, pp. 181–189, mar 2014.

[2] N.-T. and applications of microfluidics Nguyen and S. T. Wereley, *Fundamentals and applications of microfluidics*. Artech House, 2002.

[3] G. M. Walker and D. J. Beebe, "A passive pumping method for microfluidic devices," *Lab on a Chip*, vol. 2, no. 3, pp. 131–134, 2002.

[4] S. W. Rhee, A. M. Taylor, C. H. Tu, D. H. Cribbs, C. W. Cotman, and N. L. Jeon, "Patterned cell culture inside microfluidic devices," *Lab on a Chip*, vol. 5, no. 1, pp. 102–107, 2005.

[5] R. B. Fair, "Digital microfluidics: is a true lab-on-a-chip possible?," *Microfluidics and Nanofluidics*, vol. 3, no. 3, pp. 245–281, 2007.

[6] D. J. Beebe, G. A. Mensing, and G. M. Walker, "Physics and Applications of Microfluidics in Biology," *Annual Review of Biomedical Engineering*, vol. 4, pp. 261–286, aug 2002.

[7] P. Yager, T. Edwards, E. Fu, K. Helton, K. Nelson, M. R. Tam, and B. H. Weigl, "Microfluidic diagnostic technologies for global public health," *Nature*, vol. 442, no. 7101, pp. 412–418, 2006.

[8] C. D. Chin, T. Laksanasopin, Y. K. Cheung, D. Steinmiller, V. Linder, H. Parsa, J. Wang, H. Moore, R. Rouse, G. Umviligihozo, E. Karita, L. Mwambarangwe, S. L. Braunstein, J. van de Wijgert, R. Sahabo, J. E.

Justman, W. El-Sadr, and S. K. Sia, "Microfluidics-based diagnostics of infectious diseases in the developing world.," *Nature medicine*, vol. 17, no. 8, pp. 1015–1019, 2011.

[9] B. K. Van Weemen and A. Schuurs, "Immunoassay using antigenenzyme conjugates," *FEBS letters*, vol. 15, no. 3, pp. 232–236, 1971.

[10] L. Zhang, F. Gu, J. Chan, A. Wang, R. Langer, and O. Farokhzad, "Nanoparticles in Medicine: Therapeutic Applications and Developments," *Clinical Pharmacology & Therapeutics*, vol. 83, no. 5, pp. 761–769, 2007.

[11] C. Xu and S. Sun, "New forms of superparamagnetic nanoparticles for biomedical applications.," *Advanced drug delivery reviews*, vol. 65, pp. 732–43, may 2013.

[12] V. Wagner, A. Dullaart, A.-K. Bock, and A. Zweck, "The emerging nanomedicine landscape," *Nature biotechnology*, vol. 24, no. 10, pp. 1211–1217, 2006.

[13] N. Sanvicens and M. P. Marco, "Multifunctional nanoparticles properties and prospects for their use in human medicine," *Trends in Biotechnology*, vol. 26, pp. 425–433, aug 2008.

[14] I. Giouroudi and F. Keplinger, "Microfluidic biosensing systems using magnetic nanoparticles," *International Journal of Molecular Sciences*, vol. 14, pp. 18535–18556, jan 2013.

[15] M. Shinkai, "Functional magnetic particles for medical application," *Journal of Bioscience and Bioengineering*, vol. 94, pp. 606–613, dec 2002.

[16] Q. a. Pankhurst, J. Connolly, S. K. Jones, and J. Dobson, "Applications of magnetic nanoparticles in biomedicine," *Journal of physics D: ...*, vol. 167, pp. R167–R181, jul 2003.

[17] Q. A. Pankhurst, N. T. K. Thanh, S. K. Jones, and J. Dobson, "Progress in applications of magnetic nanoparticles in biomedicine," *Journal of Physics D: Applied Physics*, vol. 42, p. 224001, nov 2009.

[18] J. B. Haun, T.-J. Yoon, H. Lee, and R. Weissleder, "Magnetic nanoparticle biosensors.," *Wiley Interdisciplinary Reviews: Nanomedicine and Nanobiotechnology*, vol. 2, pp. 291–304, may 2010.

[19] I. Koh and L. Josephson, "Magnetic nanoparticle sensors.," *Sensors (Basel, Switzerland)*, vol. 9, pp. 8130–45, jan 2009.

[20] D. Issadore, C. Min, M. Liong, J. Chung, R. Weissleder, and H. Lee, "Miniature magnetic resonance system for point-of-care diagnostics," *Lab on a Chip*, vol. 11, no. 13, p. 2282, 2011.

[21] S. H. Chung, A. Hoffmann, S. D. Bader, C. Liu, B. Kay, L. Makowski, and L. Chen, "Biological sensors based on Brownian relaxation of magnetic nanoparticles," *Applied physics letters*, vol. 85, no. 14, pp. 2971–2973, 2004.

[22] D. L. Graham, H. a. Ferreira, P. P. Freitas, and J. M. S. Cabral, "High sensitivity detection of molecular recognition using magnetically labelled biomolecules and magnetoresistive sensors.," *Biosensors & bioelectronics*, vol. 18, pp. 483–8, apr 2003.

[23] G. M. Whitesides, "The origins and the future of microfluidics," *Nature*, vol. 442, pp. 368–373, jul 2006.

[24] V. Plaks, C. D. Koopman, and Z. Werb, "Circulating Tumor Cells," *Science*, vol. 341, pp. 1186–1188, sep 2013.

[25] S. Prakash and J. Yeom, "Introduction," in *Nanofluidics and Microfluidics*, pp. 1–8, Elsevier, 2014.

[26] H. A. Stone and S. Kim, "Microfluidics: basic issues, applications, and challenges," *AIChE Journal*, vol. 47, no. 6, pp. 1250–1254, 2001.

[27] B. J. Kirby, *Micro-and nanoscale fluid mechanics: transport in microfluidic devices*. Cambridge University Press, 2010.

[28] C. Kleinstreuer, *Microfluidics and nanofluidics: theory and selected applications*. John Wiley & Sons, 2013.

[29] I. Papautsky, B. K. Gale, S. Mohanty, T. a. Ameel, and a. B. Frazier, "Effects of rectangular microchannel aspect ratio on laminar friction constant," *Solutions*, no. 801, pp. 0–11, 1999.

[30] D. Brogioli and A. Vailati, "Diffusive mass transfer by nonequilibrium fluctuations: Fick's law revisited," *Physical Review E*, vol. 63, p. 012105, dec 2000.

[31] T. Shinjo, *Nanomagnetism and spintronics*. Elsevier, 2013.

[32] J. S. J. Miller and M. Drillon, *Magnetism: molecules to materials IV*, vol. 0. John Wiley & Sons, 2006.

[33] C. Binns, "Tutorial Section on Nanomagnetism," *Nanomagnetism: Fundamentals and Applications*, vol. 6, p. 1, 2014.

[34] T. Shinjo, *Overview*. Elsevier B.V., 1 ed., 2009.

[35] G. Bertotti, *Hysteresis in magnetism: for physicists, materials scientists, and engineers*. Academic press, 1998.

[36] D. L. Leslie-Pelecky and R. D. Rieke, "Magnetic Properties of Nanostructured Materials," *Chemistry of Materials*, vol. 8, no. 8, pp. 1770–1783, 1996.

[37] C. P. Bean and I. S. Jacobs, "Magnetic Granulometry and Super Paramagnetism," *Journal of applied Physics*, vol. 27, no. 12, pp. 1448–1452, 1956.

[38] V. K. Varadan, L. Chen, and J. Xie, *Nanomedicine: design and applications of magnetic nanomaterials, nanosensors and nanosystems*. John Wiley & Sons, 2008.

[39] R. Subbiah, M. Veerapandian, and K. S Yun, "Nanoparticles: functionalization and multifunctional applications in biomedical sciences," *Current medicinal chemistry*, vol. 17, no. 36, pp. 4559–4577, 2010.

[40] A. R. Fritzberg, P. G. Abrams, P. L. Beaumier, S. Kasina, A. C. Morgan, T. N. Rao, J. M. Reno, J. A. Sanderson, A. Srinivasan, and D. S. Wilbur, "Specific and stable labeling of antibodies with technetium-99m with a diamide dithiolate chelating agent," *Proceedings of the National Academy of Sciences*, vol. 85, no. 11, pp. 4025–4029, 1988.

[41] M. N. Baibich, J. M. Broto, A. Fert, F. N. Van Dau, F. Petroff, P. Etienne, G. Creuzet, A. Friederich, and J. Chazelas, "Giant magnetoresistance of (001) Fe/(001) Cr magnetic superlattices," *Physical review letters*, vol. 61, no. 21, p. 2472, 1988.

[42] G. Binasch, P. Grünberg, F. Saurenbach, and W. Zinn, "Enhanced magnetoresistance in layered magnetic structures with antiferromagnetic interlayer exchange," *Physical review B*, vol. 39, no. 7, p. 4828, 1989.

[43] C. Reig, S. Cardoso, S. C. Mukhopadhyay, and S. C. D. Freitas, *Giant Magnetoresistance (GMR) Sensors*, vol. 6 of *Smart Sensors, Measurement and Instrumentation*. Berlin, Heidelberg: Springer Berlin Heidelberg, 2013.

[44] H. Sakakima and M. Satomi, "Oscillations in low-field giant magnetoresistance in Ni-Fe-Co/Cu (/Co) superlattices," *Journal of magnetism and magnetic materials*, vol. 121, no. 1, pp. 374–377, 1993.

[45] D. J. Grifths, *Introduction to electrodynamics*, vol. 3. prentice Hall Upper Saddle River, NJ, 1999.

[46] N. Pamme, "Magnetism and microfluidics.," *Lab on a chip*, vol. 6, pp. 24–38, jan 2006.

[47] T. D. T. Meehan, *Quantitative Magnetophoresis of Micro and Nano Particles*. PhD thesis, 2007.

[48] a. Weddemann, C. Albon, a. Auge, F. Wittbracht, P. Hedwig, D. Akemeier, K. Rott, D. Meissner, P. Jutzi, and a. Hütten, "How to design magneto-based total analysis systems for biomedical applications.," *Biosensors & bioelectronics*, vol. 26, pp. 1152–63, dec 2010.

[49] J. D. Jackson, "Calssical Electrodynamics," 1975.

[50] A. Weddemann and J. Jadidian, "Ferromagnetic materials for MEMS- and NEMS-devices," *Proceedings of the COMSOL Conference in Boston*, vol. 1, 2011.

[51] H. Bruus, *Theoretical microfluidics*. New York: Oxford University Press, 2008.

[52] H. Ockendon and J. R. Ockendon, *Waves and compressible flow*, vol. 3. Springer, 2004.

[53] S. K. Mitra and S. Chakraborty, *Microfluidics and Nanofluidics Handbook: Chemistry, physics, and life science principles*. CRC Press, 2011.

[54] L. Pauling, *The nature of the chemical bond and the structure of molecules and crystals: an introduction to modern structural chemistry*, vol. 18. Cornell university press, 1960.

[55] D. Puchberger-Enengl, S. van den Driesche, C. Krutzler, F. Keplinger, and M. J. Vellekoop, "Hydrogel-based microfluidic incubator for microorganism cultivation and analyses," *Biomicrofluidics*, vol. 9, no. 1, p. 14127, 2015.

[56] J. J. N. Israelachvili, *Intermolecular and Surface forces*. Academic press, 2011.

[57] G. D. Holder, L. P. Mokka, and R. P. Warzinski, "Formation of gas hydrates from single-phase aqueous solutions," *Chemical engineering science*, vol. 56, no. 24, pp. 6897–6903, 2001.

[58] K. Atkinson and A. Bogomolny, "The Discrete Galerkin Method for Integral Equations," *Mathematics of Computation*, vol. 48, no. 178, pp. 595–616, 1987.

Chapter 2
Publication A

On-chip microfluidic biosensor using superparamagnetic microparticles

Authored by G. Kokkinis, F. Keplinger, and I. Giouroudi.
Published in *Biomicrofluidics*, **vol. 7**, p 054117, (2013).

Abstract

In this paper, an integrated solution towards an on-chip microfluidic biosensor using the magnetically induced motion of functionalized superparamagnetic microparticles (SMPs) is presented. The concept of the proposed method is that the induced velocity on SMPs in suspension, while imposed to a magnetic field gradient, is inversely proportional to their volume. Specifically, a velocity variation of suspended functionalized SMPs inside a detection microchannel with respect to a reference velocity, specified in a parallel reference microchannel, indicates an increase in their non-magnetic volume. This volumetric increase of the SMPs is caused by the binding of organic compounds (e.g. biomolecules) to their functionalized surface. The new compounds with the increased non-magnetic volume are called loaded SMPs (LSMPs). The magnetic force required for the manipulation of the SMPs and LSMPs is produced by current currying conducting microstructures, driven by a programmable microcontroller. Experiments were carried out as a proof of concept. A promising decrease in the velocity of the LSMPs in comparison to that of the SMPs was measured. Thus, it is the velocity variation which determines the presence of the organic compounds in the sample fluid.

2.1 Introduction

Integrated microfluidic platforms used in micro-total analysis systems (μTAS) have remarkable advantages over laboratory operated devices in terms of sample and reagent volume decrease, minimization of human intervention, and cost reduction. [1, 2] Labeling of biological entities or organic compounds with superparamagnetic microparticles [3] (SMPs) for biomolecular recognition is successfully implemented in bioanalytical investigations. [4, 5] Suspensions of SMPs can be magnetized by external magnetic fields enabling the controlled manipulation or related properties of SMPs like concentration, separation, trapping, and transportation as well as their detection by means of magnetic sensors. [5–8] Using magnetic methods for the aforementioned tasks has several advantages; magnetic fields can be well tuned and applied either externally or by a directly integrated solution in the microfluidic system, and SMPs are ideal candidates as the active component in miniaturized on-chip diagnostic systems due to their multifunctionality. [9–15]

Methods for magnetic manipulation of SMPs have been demonstrated in several previous studies, striving towards the production of magnetic field gradients, steep enough, to move SMPs towards a desired direction or sensing area. [16–18] Conventional methods use permanent magnets to generate the magnetic force. The main drawback of this approach is the difficulty to obtain a well-defined force. In this research work we developed an integrated solution for the application of the magnetic field gradient; parallel conducting microstructures were designed, fabricated and current was sequentially applied to them by a programmable microcontroller. This method provided adequate magnetic field gradients ensuring a better control over the SMPs motion. A novel concept is presented, which exploits the advantages of SMPs for the qualitative detection of organic compounds, e.g. biomolecules. Experiments for the proof of concept are reported and discussed.

2.2 Working principle and calculations

The proposed microfluidic biosensing method is based on the volumetric increase of functionalized SMPs due to the binding of non-

magnetic compounds onto their surface (LSMPs). This leads to a consequent decrease in the velocity of the LSMPs with respect to SMPs provided that both LSMPs and SMPs are subjected to identical magnetic forces. [10, 19] Specifically, the chip consists of a reference microchannel and a detection microchannel. In the reference microchannel plain SMPs are injected having a certain volume V and a diameter D. The fluid which contains the plain SMPs has the same viscosity as the fluid under investigation (sample fluid). In a sec-

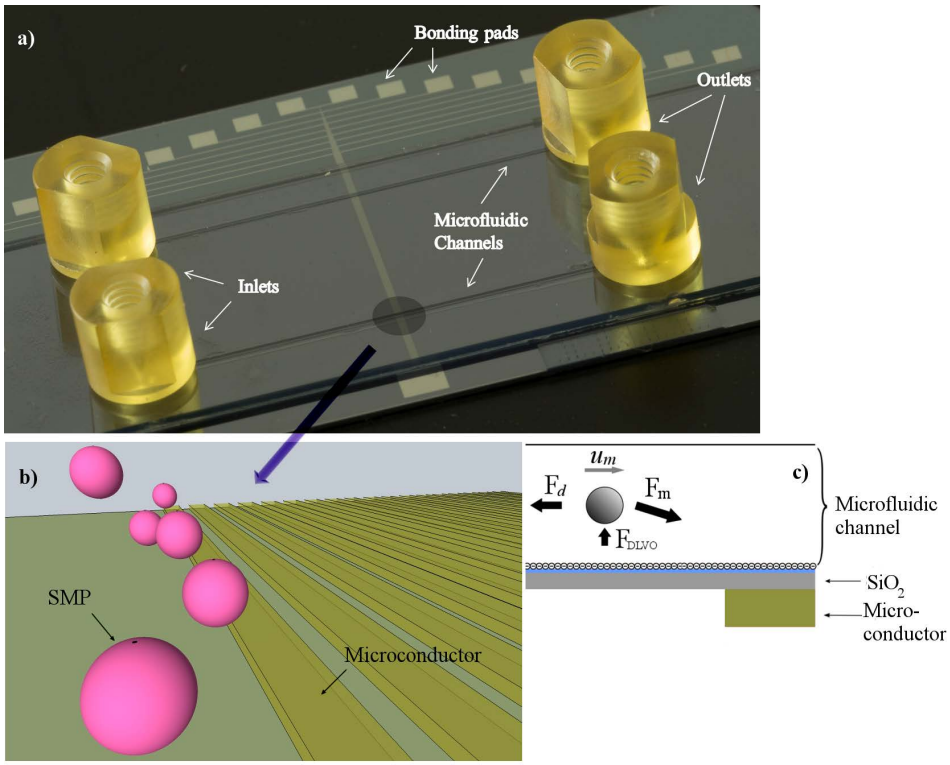

Figure 2.1: (a) Photograph of the proposed microsystem consisting of two microfluidic channels: the detection and the reference microchannels, inlet and outlet connectors and bonding pads for wire bonding. (b) Schematic illustration of the microchannel at the intersection with the parallel conducting microstructures and the SMPs. (c) Forces exerted on a single SMP: the magnetic force $\mathbf{F}_m$, the hydrodynamic drag force $\mathbf{F}_d$, and the repulsive DLVO forces (consisting mainly of the van der Waals and the electrostatic interaction forces) $\mathbf{F}_{DLVO}$. The net force defines the translational movement of the particles at the direction of the particles velocity, $\mathbf{v}_m$.

ond step the sample fluid containing the organic compounds (e.g. biomolecules) is mixed with functionalized SMPs. The resulting sample fluid contains the LSMPs which have an increased volume V' and diameter D' in comparison to the SMPs in the reference microchannel. Afterwards, the resulting sample fluid is inserted in the detection microchannel. Then, current is applied sequentially at the microstructures. This causes a magnetic force to act on the SMPs and the LSMPs, and therefore the SMPs and LSMPs move through the reference and detection microchannel along the x-axis, respectively. Figure 2.1 (b) shows the fabricated microfluidic chip.

In general, in order to use a magnetic field to move SMPs, a magnetic field gradient is required to exert a translational force. This dominant magnetic force exerted on an SMP ($\mathbf{F}_m$) is expressed as: [20]

$$\vec{\mathbf{F}}_m = \frac{V_b \Delta\chi}{\mu_0}(\vec{\mathbf{B}} \cdot \nabla)\vec{\mathbf{B}} \tag{2.1}$$

where V_b is the volume of the SMP, μ_0 is the permeability of the vacuum ($4\pi \times 10^{-7}$ H/m), $\Delta\chi$ is the difference of magnetic susceptibilities between the SMP and the surrounding medium (in our case water or buffer solutions), and $\mathbf{B}$ is the magnetic flux density.

It can be seen from Equation 2.1 that the force on an SMP is directly proportional to both the magnitude of the magnetic field and its gradient. Hence, in order to effectively manipulate the SMPs, the magnetic field can be increased given that the SMPs magnetization is not saturated and/or the magnetic gradient can be enhanced. This makes it obvious that the only realistic way of maximizing the magnetic force is by miniaturizing the magnetic field source. The small size of the conducting microstructures strongly enhances the magnetic field gradient and therefore produces large and tunable magnetic forces that can be applied on the SMPs.

There are several other forces acting on suspended particles such as colloidal, electrostatic, and hydrodynamic forces. [21, 22] Double-layer electrostatic and van der Waals forces are commonly referred to as DLVO forces, [21] named after the scientists that first described them in detail (Derjaguin, Landav, Verwey, Overbeek). According to [23] a layer of SiO_2 produces a negatively charged surface in aqueous buffer, thus producing a repulsive force between negatively charged particles and the solid surface (see Figure 2.1 (c)). In consequence,

by enhancing the electrostatic repulsive component and maintaining the van der Waals attractive force constant, the net DLVO force is a counterforce to the y-component of the magnetic force $\mathbf{F}_m$ and can be used to avoid particle-solid surface adhesion.

The hydrodynamic force is the strongest competing to the magnetic force and is, for the presented application, the one responsible for the velocity change in respect to volumetric increase. This frictional force, known as Stokes' drag, acting on the interface between the fluid and the SMP, for small Reynolds numbers and for spherical SMPs, is given by the equation 2.2: [24]

$$\vec{\mathbf{F}}_d = -3\pi D\eta\vec{\mathbf{v}} \tag{2.2}$$

where D is the diameter of the SMP, η is the viscosity of the medium, and $\mathbf{v}$ is the relative velocity of the fluid with respect to the SMP. The Stokes drag is applicable to the creeping flow regime (Stokes regime) with small Reynolds numbers ($Re < 0.5$).

As it will be shown below, the volumetric increase can be achieved by the conjugation of biomolecules or other non-magnetic particles on the surface of the functionalized SMPs. Equation 2.2 is often used to approximately calculate the drag force exerted on conjugated particles. The reason is that biomolecules rarely bind around

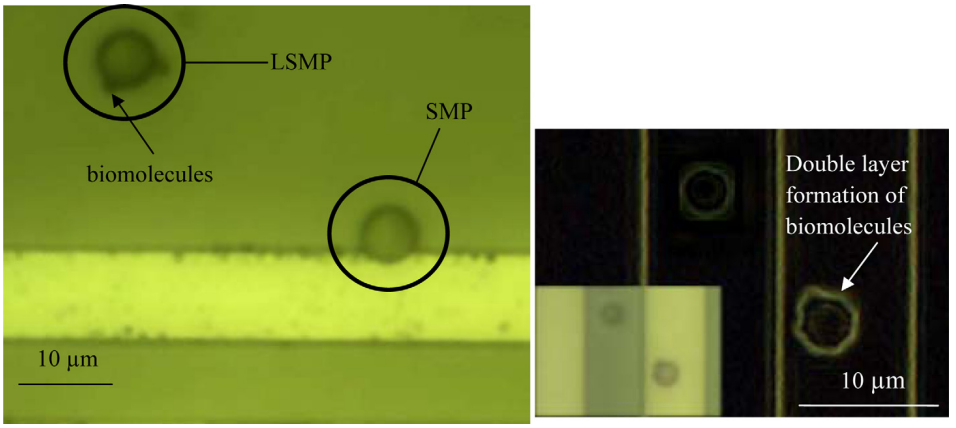

Figure 2.2: (a) Microscope photo of a 6 µm magnetic particle SMP and a compound LSMP consisting of a 6 µm functionalized SMP and 1 µm biomolecules attached to its surface. (b) Detailed photo showing the formation of a double layer of the conjugated biomolecules.

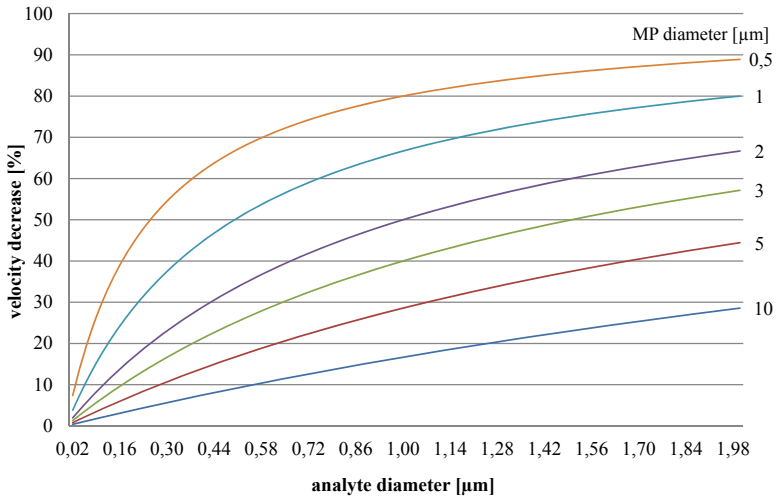

Figure 2.3: Percent velocity decrease of an LSMP compared to the plain SMP with respect to the biomolecule diameter.

the whole surface of an SMP so as to accurately apply Equation 2.2. Instead, a cluster of two or more biomolecules on the SMP is formed (as shown in Figure 2.2). Thus a more accurate form of Equation 2.2 can be used: [25]

$$\vec{\mathbf{F}}_d = -3\pi D_e \eta \vec{\mathbf{v}} K \tag{2.3}$$

where D_e is the diameter of a sphere having the same volume as the cluster of particles. That is,

$$D_e = \left(\frac{6}{\pi} Volume\right)^{1/3} \tag{2.4}$$

and K is the correction factor which for tightly packed clusters, like in our case, [26] is $K = 1.12$.

Based on Equations 2.2 - 2.4, we calculated the percent decrease of velocity for SMP of different diameters and attached biomolecules of different diameters, as shown in Figure 2.3, in order to compare it afterwards to the experimental results (Section 2.4).

An additional parameter that considers the hydrodynamic size of an SMP, apart from its physical size, is the electrical double layer around it. The electrical double layer is formed due to the surface charge acquired by a SMP through the adsorption of ions present in

the solution and/or due to the presence of charged surface groups, as well as due to the oppositely charged mobile ions that neutralize this surface charge. [27] In this work, the double layer was insignificant compared to the physical size of the SMPs (>250 nm in diameter). For the SMPs used in the presented experiments the hydrodynamic size was assumed to be equal to the physical size.

2.3 Methods and fabrication

2.3.1 Simulations

The design and the materials used for the microfluidic biosensor as well as the SMPs used for the experiments were decided upon numerical simulations of the magnetic field generated by the microstructures, the medium creeping flow, the SMP trajectories, and the thermal analysis of the device. The simulations were carried out using the commercial software COMSOL® solving the Maxwell's differential equations for the magnetic flux, the Navier-Stokes differential equations for the creeping flow wherever applicable and the Newton's second law of motion for acquiring the particle trajectories. All the studies were time dependent.

Two possible geometries of the conducting microstructures were first investigated: circular conductors and parallel conductors (see Figure 2.4). A long-range displacement of magnetic particles can be assured by arranging adjacent ring type conductors in an array with spatial overlap. [28–31] A 3D model was necessary for simulating the magnetophoretic capability of this type of circular conductors. As illustrated in Figure 2.4 (a), the advantage of the arrangement lies on concentrating the magnetic flux density at the inner side of the loop while for the parallel conductors the magnetic flux density picks at both edges (Figures 2.4 (b) and 2.5 (a)). In favour of a more simplified design the parallel conducting microstructures were investigated using a 2D model, saving both time and computing power. This parallel arrangement guarantees identical magnetic field in both channels, as well as homogeneous velocity profiles for SMPs in the same channel. Conclusively, the parallel conductor design was adapted for fabrication.

In order to evaluate different conductors width and spacing, a

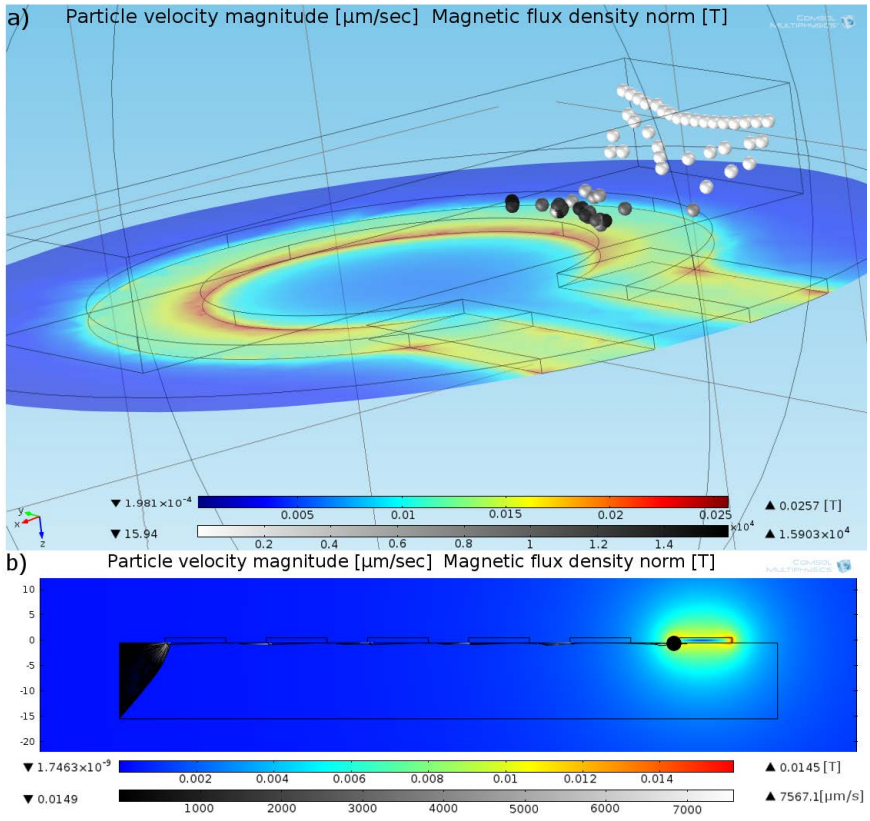

Figure 2.4: The magnetic flux density generated by the conducting microstructures carrying a current of 100 mA and the SMPs trajectories for two different designs. (a) 3D model of a single ring type conducting microstructure with magnetic particles suspended in a microfluidic channel with no flow. The image illustrates the non-uniform velocity profile of the particles as well as the concentration of the magnetic flux at the inner edge of the ring. (b) 2D model of six parallel microconductors with current sequentially applied to them, at the moment the sixth conductor is switched on. The trajectories are represented with a continuous line causing the black shape to appear at the beginning of the channel, as the particles are considered evenly distributed at the inlet.

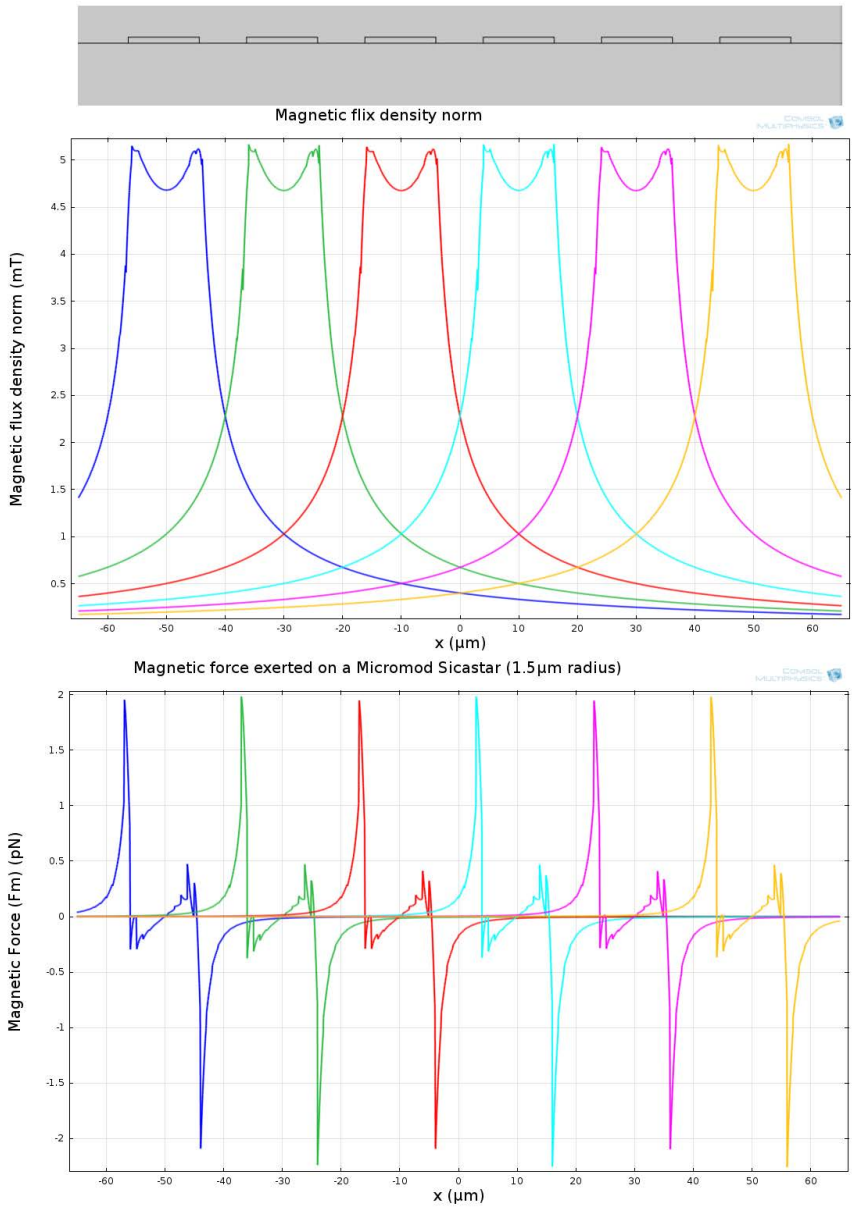

Figure 2.5: (a) Numerical results for the magnetic flux density of 6 parallel conducting microstructures (width $w = 10\,\mu m$ and spacing $s = 8\,\mu m$) along a cut line 1 µm away from the conducting microstructures. (b) The magnetic force exerted on an SMP of 1.5 µm radius and susceptibility of $\chi_m = 0.19$ along the same cut-line.

key parameter had to be kept constant. That was the current density. A silicon chip can tolerate current densities up to 10^{14} A/m^2; hence, the limiting factor in microdesign is no longer the melting point of the conducting microstructures material but rather the occurrence of electromigration, a phenomenon that occurs in conducting microstructures stressed under high current densities. This might result in a steady change of conductor dimensions, thereby causing the creation of either voids or the creation of hillocks and whiskers in the affected regions. Both can eventually lead to the failure of the circuit. In our case though, what is even more important is maintaining a low temperature on the chip, for protein and other biomolecules, denaturation prevention. For that purpose a 3D Joule heating model was designed, with a time dependent study. The time interval for which current was applied at the conducting microstructures depends on their width and spacing (see Figure 2.1 (b)). Setting an upper temperature limit at 323 °K, the numerical simulation indicated a maximum current density of 9 A/m^2.

Taking all the above into consideration as well as limitations during fabrication, the optimum dimensions for the parallel conducting microstructures made of silver (Ag) were defined as 10 µm in width, 500 nm thickness, and 8 µm spacing. For the simulations, a current of 100 mA was applied in a sequential pattern and a time dependent solution was calculated. Figure 2.5 (a) shows the distribution of the magnetic field on a cut edge of the 2D model and Figure 2.5 (b) the magnetic force acting on a Micromod Sicastar® magnetic particle of 1.5 µm radius, susceptibility of $\chi_m = 0.189$ and magnetic volume of 1.77×10^{-18} m^3. The magnetic field, which is highest at the edges, is strongly localized and drops about 83% at a distance of 10 µm from the edges. The peak force exerted on a particle is approximately 2 pN.

2.3.2 Microfluidic device fabrication

The system consisted of the Ag conducting microstructures, the microfluidic channels, the SMPs, and the LSMPs. The conducting microstructures were fabricated with standard photolithography techniques. The substrate of the device was a commercial silicon 100 mm wafer, 500 µm thick with a 1.6 µm thick layer of thermally grown ox-

ide.

First, both the wafer and the chromium pattern mask were cleaned with deionized (DI) water rinse and megasonic actuation. Then the wafer was prebaked at 120 °C for 2 min to remove water and to improve adhesion of the photoresist. Spin coating of a 1.62 µm thick layer of the AZ 5214® image reversal photoresist was achieved at 3000 rpm. A pre-bake at 107 °C for 2 min was necessary for evaporating the solvent, and a thin layer of AZ Aquatar® was spinned on to prevent reflections and stiction of the chromium mask on the wafer. An additional pre-bake step at 107 °C for 2 min was carried out. Then the wafer was exposed in a Karl Suss MA-150 Mask Aligner for 2 sec, followed by an image reversal bake at 120 °C for 2 min, 20 sec of flood exposure and development of the photoresist, using the AZ 351B® developer by spraying it on the wafer for 60 sec, while spinning at 3000 rpm. The developer was then removed by rinsing the wafer with DI water. The structured substrate was then placed into the vacuum chamber for the thermal evaporation of 50 nm titanium, 400 nm of silver, and 50 nm of chromium. Titanium was necessary for the adhesion of silver. Chromium was used for protection of the silver against corrosion caused by the following step of the lift-off process and the silicon dioxide deposition. The lift-off process took place in three successive acetone baths. A passivation layer was essential for electrical insulation, electrostatic interaction with SMPs, and future surface modifications. Silicon dioxide meets all these demands; thus, a 300 nm layer was formed on top of the structures, by employing Plasma Enhanced Chemical Vapor Deposition (PECVD). Utilizing the Oxford Plasma Lab 100 system at a low temperature (120 °C) and pressure of 6 mTorr, with a forward power of 1500 W and a gas flow rate of 40 sccm for N_2O and 5 sccm SiH_4, we obtained a SiO_2 layer with a refractive index $n = 1.426$. On the following step, the pads for wire bonding were released; a layer of positive photoresist was used as protective mask, and the whole wafer was plasma etched for 10 min, at 50 mTorr pressure and 180 V forward voltage in STS 320PC plasma etcher. The flow rates were set at 6 sccm for O_2 and at 85 sccm for CHF_3.

After the conducting microstructures were fabricated, the microfluidic channels were structured. For this purpose a 55 µm thick, negative type, dry-film, photoresist (Ordyl®) was used. First, the

wafer was cleaned, to remove any contamination from the previous treatments, by immersing it in a 10% RBS 50 basic solution in DI water at 50 °C and under ultrasonic actuation. Before lamination it was dried for 30 min at 120 °C. For the next step a standard office laminator was used, with hot rolls being set at 70 °C. A 25 sec exposure was performed using a Karl Suss MA-150 Mask Aligner followed by a 60 sec post exposure bake at 80 °C on a hot plate. The exposed photoresist was developed for 1.5 min in 3 successive baths of increasing cleanness and rinsed with isopropanol and DI water.

The final step was the sealing of the channels and the drilling of the inlet and outlet holes. For that purpose a standard 100 mm glass wafer was drilled using a Computer Numerical Control (CNC) diamond drilling system. After cleaning it, in the aforementioned solution, it was thermally bonded on the Ordyl® structures, in an EVG 501 wafer bonder, by applying a force of $60\,N/cm^2$ of photoresist. The temperature was increased to 100 °C with a 5 °C/min ramp and maintained for 30 min. Afterwards, the temperature was reduced to room temperature at 1 °C/min. To cut the bonded wafers into single chips a DAD 3220 dicing saw with a 200 µm thick diamond blade was used. The inlet and outlet holes in the glass-wafer were sealed with adhesive tape before dicing to prevent cooling water and debris from entering the chips. To free the contact pads, the glass wafer was partially removed in the areas above the pads. This was performed by dicing the chip half through; dicing only through the glass-wafer and using the Ordyl® layer as a spacer that prevented the conducting microstructures and contact pads from getting damaged.

2.4 Experiments

In order to prove the concept of velocity decrease due to volumetric increase of functionalized SMPs we used Micromer®-M-PEG-COOH (3 µm and 6 µm diameter, respectively) magnetic microparticles with carboxyl groups (-COOH) protruding from the surface and Micromer®-NH_2 (500 nm and 1 µm diameter, respectively) non-magnetic polymer particles with amino groups (-NH_2) protruding from the surface. The particles were mixed following the protocol given by the provider, and a bond was achieved between magnetic,

carboxyl group coated SMPs and non-magnetic, amino group coated polymer particles (as shown in Figure 2.6). This way, LSMPs were formed leading to an increased volume of the carboxyl group coated SMPs. It was found that the particle-particle bonding worked quite well.

The movement of the LSMPs in comparison to the movement of the SMPs caused by the applied magnetic field from the conducting microstructures was demonstrated optically by means of a microscope with a mounted CCD camera. [21] Several images and movies of the experiments were obtained. 50 mA current was applied sequentially to the conducting microstructures, employing a programmable microcontroller utilized to drive power MOSFETs; the actuation time depends on the size of the SMP.

Three sets of experiments were carried out; during the first set we confirmed the motion of SMPs without flow and only by application of a magnetic field generated from the Ag conducting microstructures. Specifically, Figure 2.7 shows the movement of a 10 µm SMP from micromer® along the x-axis of the detection microchannel with a determined actuation time of 1.2 sec. The position of the SMP is

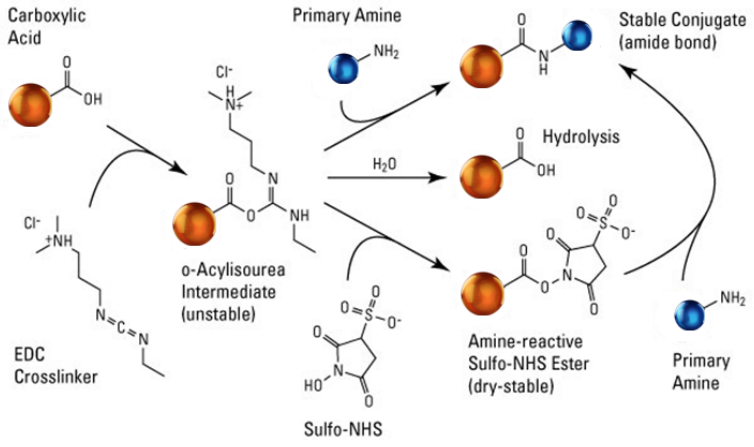

Figure 2.6: Carboxyl-to-amine crosslinking reaction scheme using the carbodiimide EDC and sulfo-NHS. Addition of NHS or Sulfo-NHS to EDC reactions (bottom-most pathway) increases efficiency and enables the SMP with the carboxylic acid group to be activated for storage and later use.

pictured every 0.6 sec travelling a distance of 108 µm with a mean velocity of 15 µm/sec.

During the second set, we proved the velocity change due to volumetric change. Specifically, 3 µm in diameter carboxyl group coated SMPs were injected in the reference microchannel and were moved towards the outlet with an actuation time of 3.8 sec resulting to a mean velocity of 5.3 µm/sec. Then the LSMPs (micromer®-M-PEG-COOH conjugated with 500 nm non-magnetic particles) were

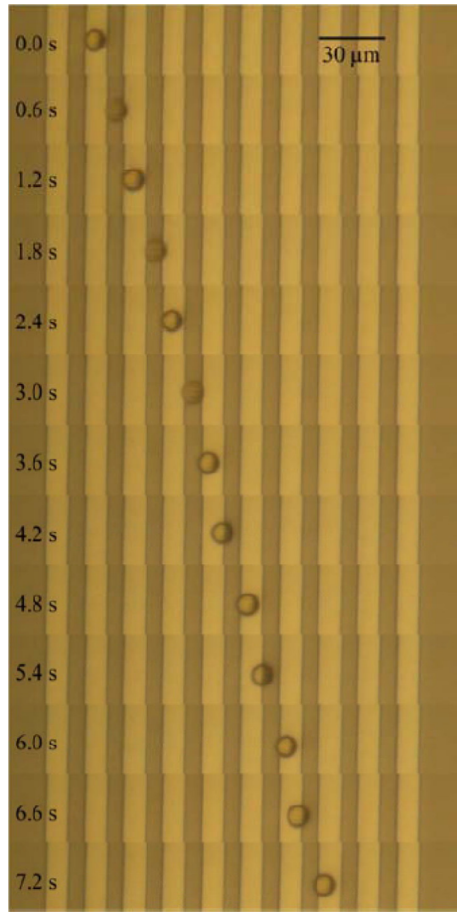

Figure 2.7: Movement of a micromer®10 µm SMP along the microfluidic channel with an actuation time of 1.2 sec per conducting microstructure (geometry: width = 10 µm, spacing = 8 µm). The current was I = 50 mA. The SMP covered a distance of 108 µm with a mean velocity of 15 µm/sec.

inserted in the detection microchannel. The predetermined actuation time was not adequate to transport the LSMPs; thus, it had to be increased to 6.8 sec leading to a mean velocity of 2.94 µm/sec. The optical realization of the experiment is shown in Figure 2.8.

The experiment showed a velocity reduction of about 44% for the LMNP against the plain MNP, while the theoretical velocity reduction was calculated to be 25% for an LMNP consisting of a 3 µm MNP plus attached 500 nm analyte compared to a plain 3 µm MNP. This relatively great deviation from the theoretical value can be attributed to the large number of nonmagnetic particles conjugated to the magnetic one. As Figures 2.2 (b) and 2.8 demonstrate there are double layers of conjugated non-magnetic particles increasing even more the volume as well as several points of contact between the par-

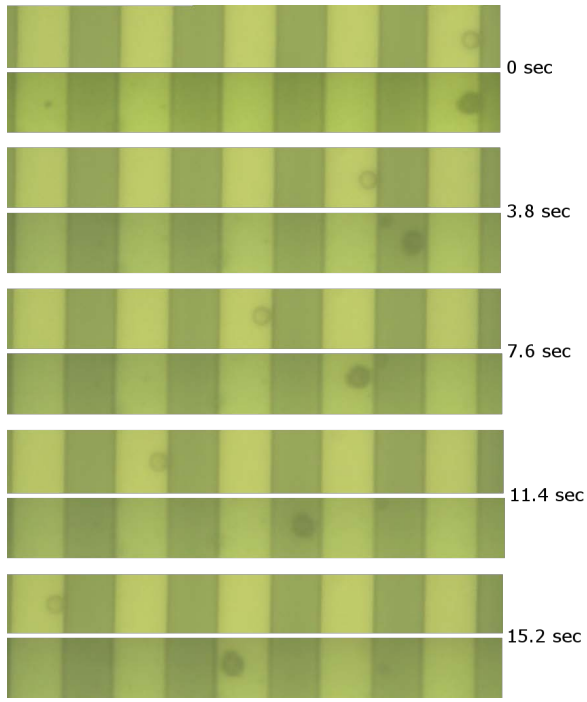

Figure 2.8: Comparison of the plain Micromer®-M-PEG-COOH 3 µm SMP in the reference channel and the LSMP consisting of 3 µm SMP conjugated with 500 nm non-magnetic particles travelling in the detection channel, actuated by a current of $I = 50$ mA. Actuation times are 2.3 sec for the SMP and 3 sec for the Loaded SMP.

ticles and the conductor's surface aggravating friction and possibly colloidal forces.

During the third set of experiments we proved that, regardless the size of the SMPs, if non-magnetic biomolecules are attached to their surface causing a volumetric increase a velocity decrease will always occur, if accelerated by a magnetic field without flow. Specifically, we used plain micromer®-M-PEG-COOH 6 µm SMPs and injected them in the reference microchannel. Afterwards, by sequen-

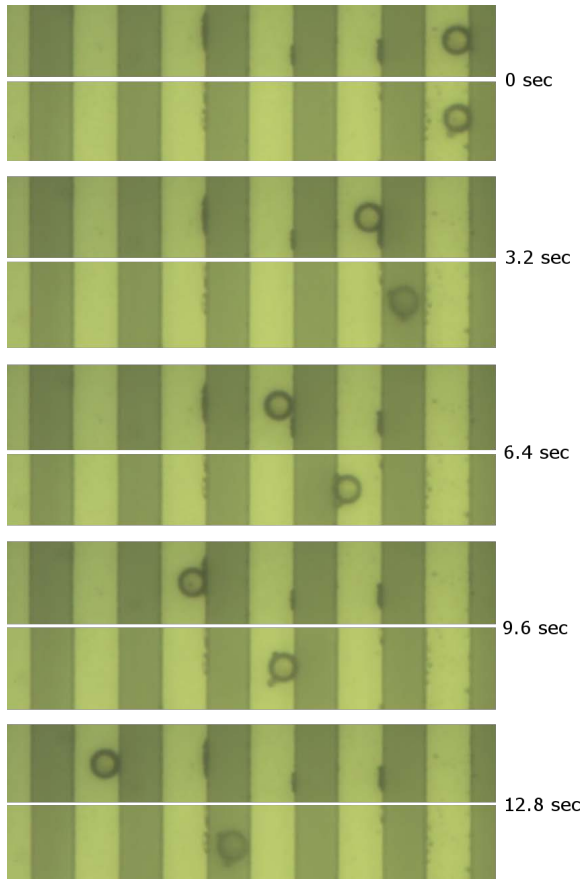

Figure 2.9: Comparison of the plain micromer®-M-PEG-COOH 6 µm SMP in the reference channel and the LSMP consisting of 6 µm SMP conjugated with 1 µm non-magnetic particles travelling in the detection channel, actuated by a current of $I = 50\,\text{mA}$. Actuation times are 3.3 sec for the SMP and 5 sec for the LSMP.

tially applying current to the conducting microstructures we moved them towards the outlet with an actuation time of 3.2 sec resulting to a mean velocity of 6.25 µm/sec (similarly to the second set of experiments). Then LSMPs (consisting of 6 µm micromer®-M-PEG-COOH conjugated with 1 µm non-magnetic particles) were inserted in the detection microchannel. The predetermined actuation time was not adequate to transport the LSMPs; thus, it had to be increased to 5 sec leading to a mean velocity of 4 µm/sec. The optical realization of the experiment is seen in Figure 2.9.

The experiment showed a velocity reduction of about 36% for the LSMP against the reference SMP. The theoretically calculated velocity reduction was 28% for an LSMP consisting of a 6 µm SMP plus 1 µm attached biomolecule compared to a plain 6 µm SMP. In that case, as Figures 2.2 (a) and 2.9 demonstrate, the deviation from the theoretical value is not that great since a lesser percentage of the outer surface is covered by non-magnetic particles.

In order to ensure that regardless the number of repetitions, the velocity of the SMPs always decreases when biomolecules are attached to their surface, thus increasing their nonmagnetic volume, we repeated the measurements for several counts and calculated the

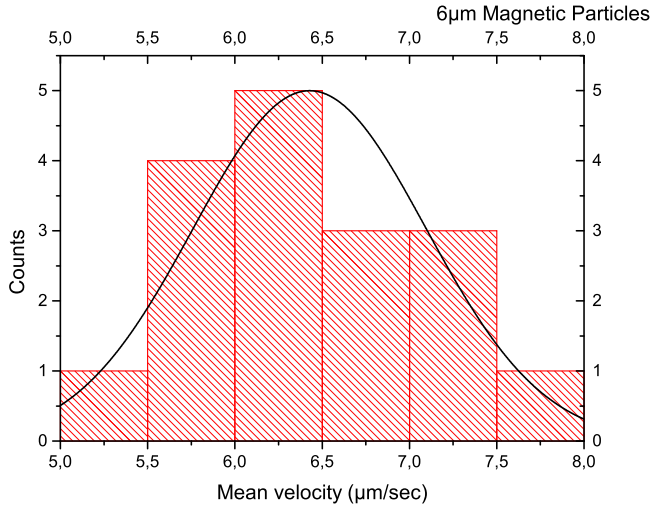

Figure 2.10: Graph showing the mean velocity of magnetic particles, SMPs, with a diameter of 6 µm versus the counts.

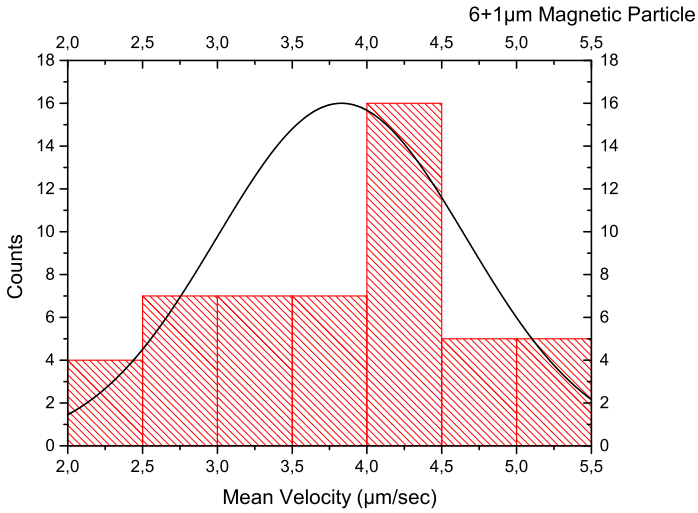

Figure 2.11: Graph showing the mean velocity of magnetic particles, SMPs, with a diameter of 6 + 1 µm versus the counts.

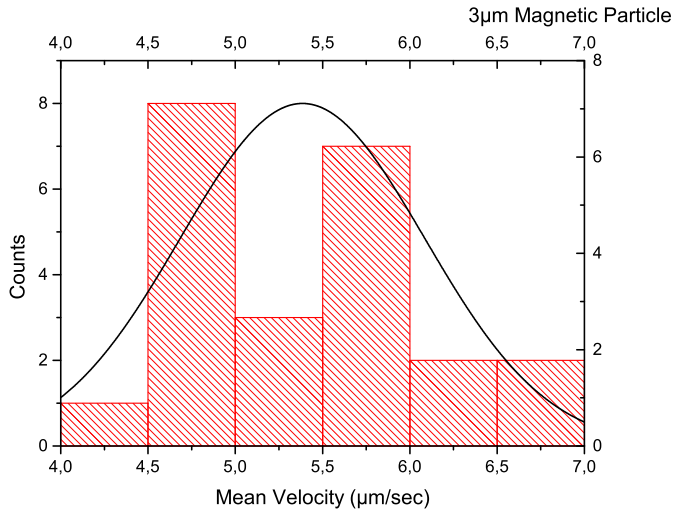

Figure 2.12: Graph showing the mean velocity of magnetic particles, SMPs, with a diameter of 3 µm versus the counts.

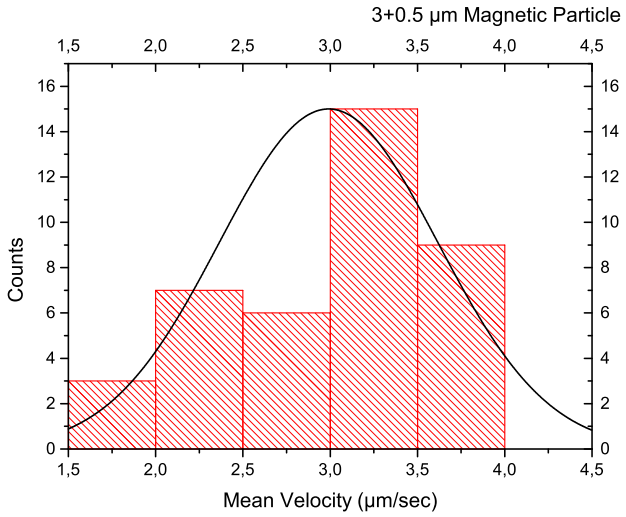

Figure 2.13: Graph showing the mean velocity of magnetic particles, SMPs, with a diameter of 3 + 0.5 µm versus the counts.

mean velocity of the SMPs without and with increased volume (as shown in Figures 2.10 - 2.13). Specifically, Figure 2.10 shows that for 6 µm SMPs, after 17 repetitions of the experiment, the statistical mean of the mean velocity was approximately 6.43 µm/sec with a standard deviation of ≈ 0.67 and the median value equal to 6.25 µm/sec. Figure 2.11 shows that for LSMPs consisting of 6 µm SMPs and 1 µm non-magnetic attached particles, after 50 repetitions the statistical mean of the mean velocity was approximately 3.83 µm/sec with a standard deviation of ≈ 0.83 and the median value equal to 4 µm/sec. The same set of repetitive experiments was carried out for 3 µm SMPs (after 23 repetitions), as shown in Figure 2.12, and for LSMPs consisting of 3 µm SMPs and 0.5 µm nonmagnetic attached particles (after 40 repetitions), as shown in Figure 2.13. Table 2.1 shows the conclusive results of the aforementioned experiments.

Taking these results into consideration we can safely state that a non-magnetic volumetric increase of SMPs always leads to a velocity decrease. Therefore, by using our biosensing method, once a velocity decrease of the functionalized SMPs occurs when accelerated inside a microfluidic channel by an externally applied magnetic field without flow, it is the indication of the presence (detection) of analyte

	Magnetic Particles	Statistical Mean	Standard Deviation	Min.	Median	Max.
Mean Velocity (μm/sec)	6 μm	6.4280	0.6675	5.4054	6.25	7.6923
	$6 + 1$ μm	3.8294	0.8349	2.2222	4	5.1282
	3 μm	5.3848	0.7002	4.4444	5.3333	6.6667
	$3 + 0.5$ μm	2.9907	0.6269	1.5778	3.1688	3.9026

Table 2.1: The values of the statistical mean, the standard deviation, the minimum, the median, and the maximum value of the mean velocity (in μm/sec) for the 6 μm and 3 μm Superparamagnetic Microparticles (SMPs) as well as for the $6 + 1$ μm and the $3 + 0.5$ μm Loaded SMPs (LSMPs).

(e.g. biomolecules) in the fluid under investigation. This percentage velocity decrease can be optimized if microparticles of smaller diameter (nm range) are utilized. Finally, one important factor of on chip particle manipulation. devices that is often overlooked is the colloidal and surface forces acting among particles, defining whether a solution is stable or not, and between particles and surfaces. These forces are adequately defined by the DLVO interaction theory which suggests that the stability of a colloidal system is determined by the sum of the van der Waals attractive and electrical double layer repulsive forces that exist between particles as they approach each other. In our experiments, enhancement of the electrostatic interaction was achieved by decreasing the electrolyte and the hydrogen ion concentration, meaning adjusting the solution at a pH 9 or higher. Although a steric stabilization approach is often preferable, for the described application a more basic solution is not inhibiter. The pH of the solution was adjusted by adding Hellmanex® at a dilution ratio 1:50 in DI water.

2.5 Conclusions

The presented experiments proved that the proposed system can be successfully used for the detection of organic compounds conjugated with superparamagnetic particles. The possibility of using magnetic sensors for the detection of the movement of the magnetic micropar-

ticles instead of optical detection is currently being investigated. Additionally, the possibility to use the principal of operation of the presented device as a filtering mechanism that would separate SMPs and LSMPs when inside the same microfluidic channel will be considered for future investigations. Setting up an actuation time adequate for the size of the SMPs, the LSMPs will fall back, thus separating them.

Acknowledgements

The authors would like to acknowledge the financial support of the Austrian Science Fund (FWF) with Project No. P 24372-N19. The authors are grateful to Mr. Dietmar Puchberger-Enengl for the technical support.

Bibliography

[1] A. Arora, G. Simone, G. B. Salieb-Beugelaar, J. T. Kim, and A. Manz, "Latest Developments in Micro Total Analysis Systems," *Analytical Chemistry*, vol. 82, pp. 4830–4847, jun 2010.

[2] M. L. Kovarik, P. C. Gach, D. M. Ornoff, Y. Wang, J. Balowski, L. Farrag, and N. L. Allbritton, "Micro Total Analysis Systems for Cell Biology and Biochemical Assays," *Analytical Chemistry*, vol. 84, pp. 516–540, jan 2012.

[3] G. S. E. Antipas, E. Statharas, P. Tserotas, N. Papadopoulos, and E. Hristoforou, "Experimental and First-Principles Characterization of Functionalized Magnetic Nanoparticles," *ChemPhysChem*, vol. 14, pp. 1934–1942, jun 2013.

[4] D. L. Graham, H. a. Ferreira, and P. P. Freitas, "Magnetoresistive-based biosensors and biochips.," *Trends in biotechnology*, vol. 22, pp. 455–62, sep 2004.

[5] M. a. M. Gijs, "Magnetic bead handling on-chip: new opportunities for analytical applications," *Microfluidics and Nanofluidics*, pp. 22–40, oct 2004.

[6] P. Kemidis, C. Orfanidou, and E. Hristoforou, "Position sensors based on the delay line principle," *Journal of Optoelectronics and Advanced Materials*, vol. 4, no. 2, pp. 347–352, 2002.

[7] E. Hristoforou and A. Ktena, "Magnetostriction and magnetostrictive materials for sensing applications," *Journal of Magnetism and Magnetic Materials*, vol. 316, pp. 372–378, sep 2007.

[8] B. Dufay, S. Saez, C. Cordier, C. Dolabdjian, C. Dubuc, E. Hristoforou, and S. Ubizskii, "2D hybrid yttrium iron garnet magnetic sensor noise characterization," *Sensors Journal, IEEE*, vol. 11, no. 12, pp. 3211–3215, 2011.

[9] I. Giouroudi, G. Kokkinis, C. Gooneratne, and J. Kosel, "Microfluidic biosensing device for controlled trapping and detection of magnetic microparticles," in *Proceedings - 29th Southern Biomedical Engineering Conference, SBEC 2013*, (Miami, FL), pp. 1–2, 2013.

[10] A. Dangl, G. Kokkinis, F. Keplinger, and I. Giouroudi, "In vitro biosensing based on magnetically induced motion of magnetic nanoparticles," in *Technical Proceedings of the 2013 NSTI Nanotechnology Conference and Expo, NSTI-Nanotech 2013*, vol. 3, pp. 135–138, 2013.

[11] A. Sofla, B. Cirkovic, A. Hsieh, J. W. Miklas, N. Filipovic, and M. Radisic, "Enrichment of live unlabelled cardiomyocytes from heterogeneous cell populations using manipulation of cell settling velocity by magnetic field," *Biomicrofluidics*, vol. 7, no. 1, p. 14110, 2013.

[12] D. Puchberger-Enengl, S. Podszun, H. Heinz, C. Hermann, P. Vulto, and G. A. Urban, "Microfluidic concentration of bacteria by on-chip electrophoresis," *Biomicrofluidics*, vol. 5, no. 4, p. 44111, 2011.

[13] H.-S. Moon, K. Kwon, K.-A. Hyun, T. S. Sim, J. C. Park, J.-G. Lee, and H.-I. Jung, "Continual collection and re-separation of circulating tumor cells from blood using multi-stage multi-orifice flow fractionation," *Biomicrofluidics*, vol. 7, no. 1, p. 14105, 2013.

[14] L. Liang, J. Zhu, and X. Xuan, "Three-dimensional diamagnetic particle deflection in ferrofluid microchannel flows," *Biomicrofluidics*, vol. 5, no. 3, p. 34110, 2011.

[15] I. Cima, C. W. Yee, F. S. Iliescu, W. M. Phyo, K. H. Lim, C. Iliescu, and M. H. Tan, "Label-free isolation of circulating tumor cells in microfluidic devices: Current research and perspectives," *Biomicrofluidics*, vol. 7, no. 1, p. 11810, 2013.

[16] C. Liu, L. Lagae, and G. Borghs, "Manipulation of magnetic particles on chip by magnetophoretic actuation and dielectrophoretic levitation," *Applied physics letters*, vol. 90, no. 18, p. 184109, 2007.

[17] N. Z. Danckwardt, M. Franzreb, A. E. Guber, and V. Saile, "Pump-free transport of magnetic particles in microfluidic channels," *Journal of Magnetism and Magnetic Materials*, vol. 323, pp. 2776–2781, nov 2011.

[18] R. Wirix-Speetjens and J. De Boeck, "On-chip magnetic particle transport by alternating magnetic field gradients," *Magnetics, IEEE Transactions on*, vol. 40, no. 4, pp. 1944–1946, 2004.

[19] I. Giouroudi, S. van den Driesche, J. Kosel, R. Grossinger, and M. J. Vellekoop, "On-chip bio-analyte detection utilizing the velocity of magnetic microparticles in a fluid," *Journal of Applied Physics*, vol. 109, no. 7, p. 07B304, 2011.

[20] N. Pamme, "Magnetism and microfluidics.," *Lab on a chip*, vol. 6, pp. 24–38, jan 2006.

[21] P. C. Hiemenz, *Principles of colloid and surface chemistry*, vol. 188. M. Dekker New York, 1986.

[22] N.-T. Nguyen and S. T. Wereley, *Fundamentals and applications of microfluidics*. Artech House, 2002.

[23] C. Liu, L. Lagae, R. Wirix-Speetjens, and G. Borghs, "On-chip separation of magnetic particles with different magnetophoretic mobilities," *Journal of Applied Physics*, vol. 101, no. 2, p. 024913, 2007.

[24] C. Derec, C. Wilhelm, J. Servais, and J.-C. Bacri, "Local control of magnetic objects in microfluidic channels," *Microfluidics and Nanofluidics*, vol. 8, pp. 123–130, aug 2009.

[25] G. M. Hidy, "Aerosols: an Industrial and Environmental ScienceAcademic Press," *New York*, 1984.

[26] A. Lerman, *Geochemical processes. Water and sediment environments.* John Wiley and Sons, Inc., 1979.

[27] J. J. N. Israelachvili, *Intermolecular and Surface forces*. Academic press, 2011.

[28] I. Giouroudi and F. Keplinger, "Microfluidic biosensing systems using magnetic nanoparticles," *International Journal of Molecular Sciences*, vol. 14, pp. 18535–18556, jan 2013.

[29] C. P. Gooneratne, I. Giouroudi, and J. Kosel, "A Planar Conducting Micro-Loop Structure for Transportation of Magnetic Beads: An Approach Towards Rapid Sensing and Quantification of Biological Entities," *Sensor Letters*, vol. 10, pp. 770–774, mar 2012.

[30] C. P. Gooneratne, C. Liang, I. Giouroudi, and J. Kosel, "An integrated micro-chip for rapid detection of magnetic particles," *Journal of Applied Physics*, vol. 111, no. 7, p. 07B327, 2012.

[31] A. Rida, V. Fernandez, and M. a. M. Gijs, "Long-range transport of magnetic microbeads using simple planar coils placed in a uniform magnetostatic field," *Applied Physics Letters*, vol. 83, no. 12, p. 2396, 2003.

Chapter 3
Publication B

Microfluidics for the Rapid Detection of Pathogens Using Giant Magnetoresistance Sensors

Authored by G. Kokkinis, S. Cardoso, F. Cardoso, and I. Giouroudi. Published in *IEEE Transactions on Magnetics*, **vol.50**, p 4401304, (2014).

Abstract

This paper presents an integrated solution toward an on-chip microfluidic diagnostic system using the magnetically induced motion of functionalized magnetic microparticles (MPs) in combination with giant magnetoresistance (GMR) sensors. The innovative aspect of the proposed method is that the induced velocity on MPs in suspension, while imposed to a magnetic field gradient, is inversely proportional to their volume. Specifically, a velocity variation of suspended functionalized MPs inside a detection microchannel with respect to a reference velocity, specified in a parallel reference microchannel, indicates an increase in their nonmagnetic volume. This volumetric increase of the MPs is caused by the binding of pathogens (e.g. bacteria) to their functionalized surface. The new formed compounds, which have an increased nonmagnetic volume, are called loaded MPs (LMPs). Experiments with functionalized MPs and LMPs with Escherichia coli attached to their surface were conducted as a proof of concept. Their movement was demonstrated optically by means of a microscope with a mounted CCD camera as well as by measuring the resistance change of the integrated GMR sensors.

Index terms: Biosensor, diagnostics, giant magnetoresistance (GMR).

3.1 Introduction

The remarkable promise of microfluidics in combination with magnetic methods opens the path to exceptional advances in point-of-care pathogen diagnostics and on-site food and water quality control.

Pathogens are infectious microorganisms that cause diseases to their host, e.g. bacteria, viruses, fungi, and parasites [1,2,3,4]. Most of the existing laboratory techniques to identify suspected pathogens use culturing of these microorganisms to grow colonies large enough to identify. Nevertheless, there exist methods which do not require a large amount of sample and provide rapid identification, such as immunological tests (e.g. ELISA immunoassays), nucleic-acid-based diagnostics and microfluidics[5,6]. [1–4] Yet, these methods can be technologically complex, require established laboratory infrastructure and well-trained personnel, or do not provide information on the pathogen load. Moreover, even though they are highly sensitive and specific, false positive and negative results may occur. These results may be caused by improper sample storage or treatment, improper washing methods, or reagent deterioration. The reported microfluidic diagnostic systems up to date either require complex on-chip designs, fluorescence or quantum dot labeling, nucleic acid amplification, or continuous flow. [5–7]

In this paper, we propose a simple microfluidic diagnostic platform which combines magnetic isolation (filtering mechanism) and magnetic detection of pathogens without flow, without the need to use fluorophores or quantum dot labels, and without complicated microfluidic structures.

[1] http://www.unaids.org/en/
[2] http://www.preventchildhoodinfluenza.org
[3] http://globalviral.org
[4] http://www.un-influenza.org
[5] http://www.alere.com
[6] http://www.micronics.net

3.2 Working principle

Our microfluidic system consists of two microfluidic channels; reference and detection channel. The sample under investigation (e.g. water) is mixed with antibody functionalized microparticles (MPs) (which are commercially available, see [8]). The bacteria (e.g. *Escherichia coli*) are specifically captured by the MPs due to the affinity between the antibodies and the surface antigens of the bacteria forming compounds-loaded MPs (LMPs). Afterwards, the resulting fluid is transported into the detection channel. The reference channel is filled with the same, plain (nonfunctionalized) MPs. The magnetically tagged bacteria and the plain MPs are accelerated inside the detection and reference microchannels by embedded aluminum conducting microstructures, which are controlled by a programmable microprocessor. [9–13] The advantage of these microstructures over an external permanent magnet is that they ensure a better control of the magnetic field (by controlling the applied current), hence allowing uniformity regarding the acceleration of the MPs and LMPs. This way, a fully automated solution for the application and control of the magnetic field is also offered, since the current power supply can be controlled by a PC and the relevant software. In addition to that, the position of the conductive microstructures, coated with a thin passivation layer, can be controlled in the micrometer range.

Two giant magnetoresistance (GMR) sensors are located near the inlet and outlet of the reference and the detection microchannels. When MPs and LMPs are introduced in the microchannels a change in the electrical resistance of the first GMR sensor, located near the inlet, occurs. Then, the MPs and LMPs are accelerated by means of the externally applied magnetic force through the conducting microstructures. When the MPs and LMPs exit the reference and detection microchannels, respectively, the second GMR sensor located near the outlet registers a change in its electrical resistance. The time difference between the detection of the resistance change on the first GMR sensor and the detection of the resistance change on the second GMR sensor is measured. Then, the velocity of the MPs within the microfluidic channels is calculated. Thus, it is the velocity variation which determines the presence of pathogens in the sample fluid.

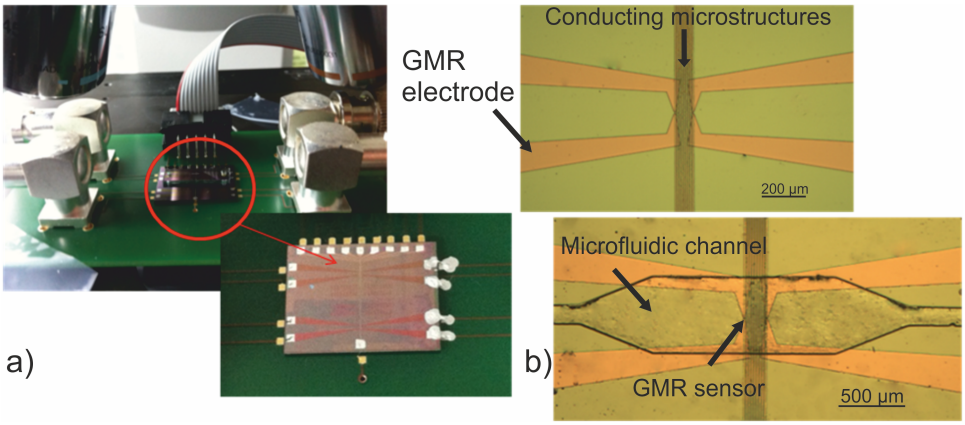

Figure 3.1: (a) Photograph of the developed diagnostic microsystem consisting of the GMR sensors, the conducting microstructures, and the microfluidic channels. (b) Microscope photograph of the GMR sensor with the conducting microstructures and the microfluidic channel.

3.3 Fabrication

To prove the concept of manipulating and detecting MPs inside microfluidic channels, we fabricated two GMR sensors with the following spin valve structure: Si (substrate)/ Al_2O_3 100 nm/ Ta 2 nm/ NiFe 3.6 nm/ CoFe 2.3 nm/ Cu 2.3 nm/ CoFe 2.3 nm/ MnIr 8 nm/ Ta 30 nm/ $TiWN_2$ 15 nm [14], with 6 µm length and 2 µm width. 300 nm GMR electrodes were sputtered to provide in-plane current flow to the sensing structures and a 300 nm silicon nitride passivation layer was deposited. On top of the passivated sensors, we fabricated aluminum conducting microstructures using a photolithography and sputtering deposition technique having a 10 µm width, a spacing of 8 µm, and a thickness of 500 nm. The conducting microstructures were passivated with a 350 nm thick silicon dioxide layer allowing further surface modification and providing protection from corrosion.

Finally, the two microfluidic channels were fabricated on top of the conducting microstructures using a dry photoresist thin film (Ordyl® SY355) of 55 µm thickness as a mold, structuring it with standard photolithography process and pouring on top of it the organic polymer polydimethylsiloxane. The developed microfluidic system with the integrated GMR sensors and conducting microstructures is

shown in Figure 3.1.

3.4 Experiments

To prove the concept of the MPs movement by the conducting microstructures and their detection by the GMR sensors, the following experiments were carried out: an indefinite number of *E. coli* K12 wild-type bacteria were conjugated with rabbit polyclonal antibodies covalently coupled with the N-hydroxysuccinimide ester of biotin, after being centrifuged and resuspended in lesser volume to increase the concentration. They were coupled with Dynabeads® M-280 superparamagnetic particles of 2.8 µm in diameter with a monolayer of recombinant streptavidin covalently coupled to the surface. The coupling between the particles and the antibodies (attached to the bacteria) was highly effective due to the strong affinity between streptavidin and biotin. Later on, secondary goat antirabbit IgG antibodies conjugated with a fluorophore were attached to the primary antibodies to confirm the binding of the primary antibodies to the antigen on the bacteria. An alternative approach to the attachment of beads to the bacteria suggests initially the functionalization of the particles with primary and secondary antibodies. The functionalized MNPs are shown in Figure 3.2 (a). Afterwards, the functionalized MNPs (without the secondary fluorescent antibodies) were incubated with

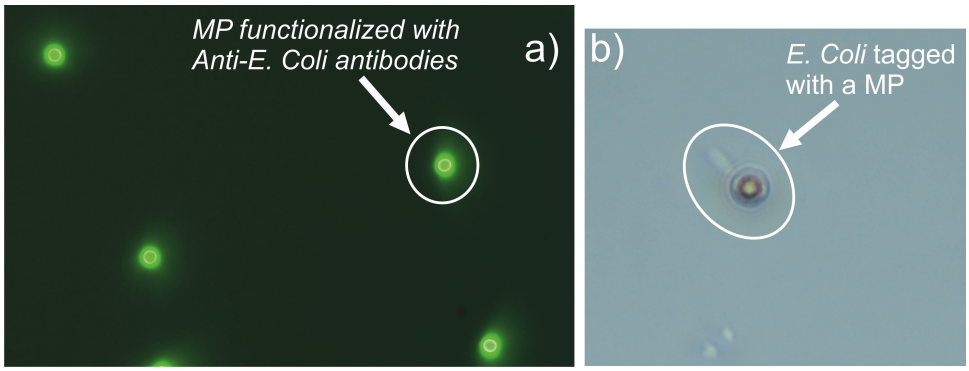

Figure 3.2: (a)2.8 µm Dynabeads® covered with Rabbit polyclonal *E. coli* antibodies and fluorescent Goat antirabbit IgG. (b) Magnetically labeled *E. coli*.

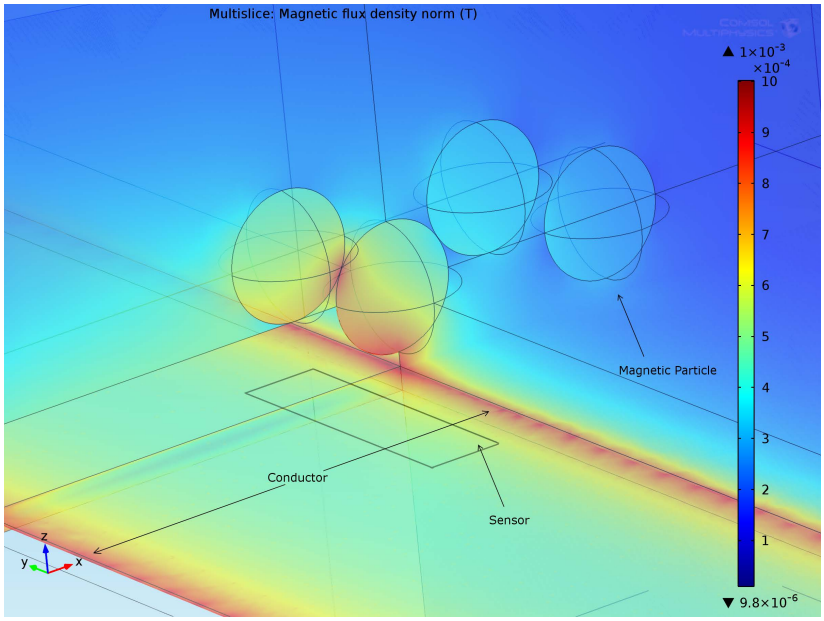

Figure 3.3: COMSOL simulation, the magnetic-flux density generated by the current of the conducting microstructure, and the stray magnetic-flux density of the MPs averaged over the volume of the GMR sensor.

E. coli for 30 min and the bacteria were successfully labeled by the MNPs, as shown in Figure 3.2 (b).

To estimate the output of the sensor, the magnetic-flux density generated by the current of the conducting microstructure and the stray magnetic-flux density of the MPs averaged over the volume of the GMR sensor had to be determined. Thus, a finite element simulation using COMSOL Multiphysics was carried out, as shown in Figure 3.3. The susceptibility of the MPs was set at 0.8 (SI, value taken from the data sheet). In the model, the conducting microstructure, the sensor, and the separation between the GMR sensors and the particles (passivation layers) have the same dimensions, as described in Section 3.3.

For the detection of the MPs, an AC (I_M) at a frequency over 1 kHz (f_M) was conducted through the conducting microstructures to magnetize the superparamagnetic beads. An AC (I_s) of lower frequency (f_s) was conducted through the sensor. The first, higher frequency current provides the carrier signal over which the modulating, lower

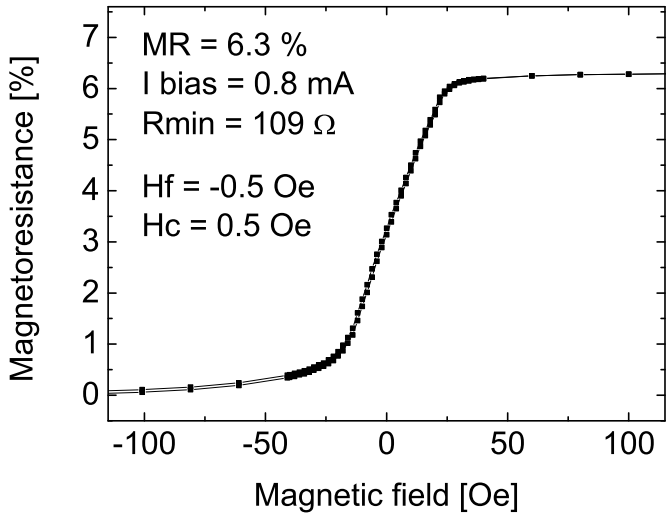

Figure 3.4: Sensor transfer curve, showing the magnetoresistance MR = 6.3%, the ferromagnetic coupling field from the pinned layer $H_f = 0.5\,\mathrm{Oe}$, and the coercivity $H_c = 0.5\,\mathrm{Oe}$.

frequency signal of the sensor will be distinguished from $1/f$ noise which is dominant at lower frequencies. To acquire a measurement the signal has to be demodulated. This is achieved by a lock-in amplifier. To avoid the induction of a crosstalk voltage due to alternating magnetic field of the conductor and the parasitic inductance of the sensor, the demodulation had to be done at the sum of the two frequencies $f_M + f_s$.

Thus the output of the lock-in amplifier is the RMS value of the voltage component at the frequency of $f_M + f_s$: [15]

$$V_{out} = \frac{1}{2\sqrt{2}} I_s R_0 \delta (H_M + H_{stray}) \tag{3.1}$$

where R_0 is the resistance of the sensor at the absence of magnetic field, H_M is the magnetic field amplitude due to the current of the conductor, and the H_{stray} is the magnetic field amplitude of the MPs.

3.5 Results and discussion

Initially, the resistance change and the magnetoresistance ratio of the GMR sensors versus an externally applied field was measured without the presence of MPs and LMPs, showing a field sensitivity of 0.12 %/Oe (Figure 3.4).

Then, an ac I_s(rms) = 10 mA is fed through the conducting microstructure. According to the finite element simulation this generates a magnetic field with an amplitude of $H_M = 4.974$ Oe. Using Equation 3.1, we acquire the theoretical output of the sensor $V_{out} = 339$ µV. As Figure 3.5 implies, the output of the sensor due to the magnetic field generated by the conducting microstructure corresponds to the flat region of the graph (plotting the voltage output versus the time). The value that we acquire by the graph equals to 358 µV, which adequately matches the theoretical value.

Afterward, the magnetically tagged *E. coli* bacteria were inserted in the detection microchannel. Figure 3.6 shows them inside the channel while accumulating at the vicinity of the GMR sensor while attracted by the conducting microstructure. The images were taken under the fluorescent microscope (LMPs are the green dots on the image with the bacteria being denoted by the areas of greater intensity). The simulations mentioned in Section 3.4 were also carried out for that same case shown in Figure 3.6.

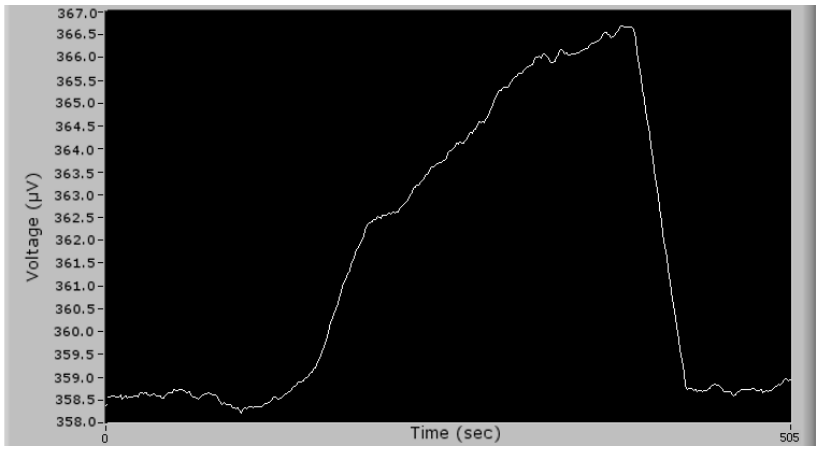

Figure 3.5: Sensor output when the magnetically tagged bacteria (LMPs) pass by it.

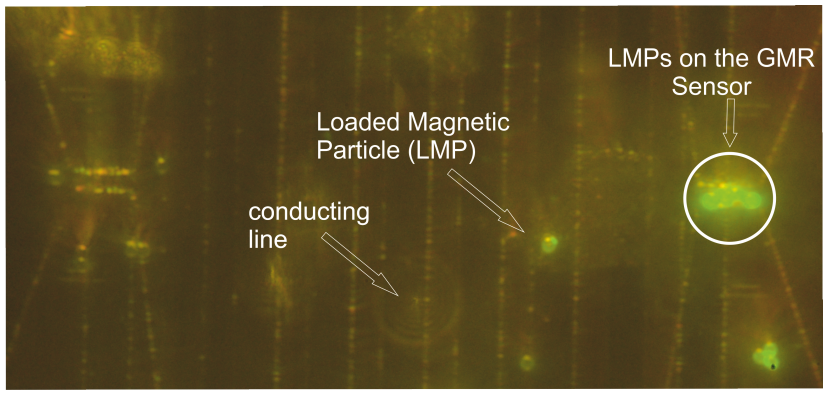

Figure 3.6: Fluorescent microscope images of the magnetically tagged *E. coli* bacteria inside the detection microchannel.

The magnetic field averaged over the volume of the GMR sensor is equal to $H_M + H_{stray} = 5.0817\,\text{Oe}$ that equals to $H_{stray} = 0.1076\,\text{Oe}$, which is used in Equation 3.1, leads to a theoretical change of voltage due to the stray field of the four LMPs equal to 6 µV. Figure 3.5 shows the sensor output difference due to the stray filed equal to approximately 8 µV that is again adequately near the theoretical value. The magnetically tagged bacteria (LMPs) move on to the next conductor attracted by a DC magnetic field. This is when the lock-in amplifier's output settles back to its original value.

3.6 Conclusion

In this paper, a simple method for the detection of pathogens using microfluidics and GMR sensors was presented. The advantages of the proposed system are that neither flow, nor the use of fluorophores or quantum dot labels, nor complicated microfluidic structures is required.

The detection of bacteria is based on the velocity difference between plain magnetic particles and magnetically tagged bacteria. Magnetically tagged *E. coli* was successfully detected by the GMR sensors.

The chances of acquiring false (negative/positive) results are strongly decreased by the fact that a reference channel is always used to define the velocity of plain magnetic particles (when no pathogens

are attached). Further investigations will be carried out in future studies.

The proposed system can be used for food and quality control as well as for medical diagnostics. The integration of a micromixer before the detection microchannel, to mix the functionalized MPs with the sample fluid, is currently being investigated.

Acknowledgement

This work was supported by the Austrian Science Fund under Project P 24372-N19.

Bibliography

[1] D. Mabey, R. W. Peeling, A. Ustianowski, and M. D. Perkins, "Tropical infectious diseases: diagnostics for the developing world," *Nature Reviews Microbiology*, vol. 2, no. 3, pp. 231–240, 2004.

[2] R. M. Lequin, "Enzyme immunoassay (EIA)/enzyme-linked immunosorbent assay (ELISA)," *Clinical chemistry*, vol. 51, no. 12, pp. 2415–2418, 2005.

[3] B. Vuylsteke, "Current status of syndromic management of sexually transmitted infections in developing countries," *Sexually Transmitted Infections*, vol. 80, no. 5, pp. 333–334, 2004.

[4] D. Nichols, "Cultivation gives context to the microbial ecologist," *FEMS microbiology ecology*, vol. 60, no. 3, pp. 351–357, 2007.

[5] J. Ruelle, K. Jnaoui, I. Lefèvre, N. Lamarti, and P. Goubau, "Comparative evaluation of the VERSANT HIV-1 RNA 1.0 kinetic PCR molecular system (kPCR) for the quantification of HIV-1 plasma viral load," *Journal of Clinical Virology*, vol. 44, no. 4, pp. 297–301, 2009.

[6] M. Usdin, M. Guillerm, and A. Calmy, "Patient needs and point-of-care requirements for HIV load testing in resource-limited settings," *Journal of infectious diseases*, vol. 201, no. Supplement 1, pp. S73–S77, 2010.

[7] S. Wang, F. Xu, and U. Demirci, "Advances in developing HIV-1 viral load assays for resource-limited settings," *Biotechnology advances*, vol. 28, no. 6, pp. 770–781, 2010.

[8] A. A. Neurauter, M. Bonyhadi, E. Lien, L. Nøkleby, E. Ruud, S. Camacho, and T. Aarvak, "Cell isolation and expansion using Dynabeads," in *Cell Separation*, pp. 41–73, Springer, 2007.

[9] I. Giouroudi and F. Keplinger, "Microfluidic biosensing systems using magnetic nanoparticles," *International Journal of Molecular Sciences*, vol. 14, pp. 18535–18556, jan 2013.

[10] F. Li, I. Giouroudi, and J. Kosel, "A biodetection method using magnetic particles and micro traps," *Journal of Applied Physics*, vol. 111, no. 7, p. 07B328, 2012.

[11] I. Giouroudi, S. van den Driesche, J. Kosel, R. Grossinger, and M. J. Vellekoop, "On-chip bio-analyte detection utilizing the velocity of magnetic microparticles in a fluid," *Journal of Applied Physics*, vol. 109, no. 7, p. 07B304, 2011.

[12] A. Dangl, G. Kokkinis, F. Keplinger, and I. Giouroudi, "In vitro biosensing based on magnetically induced motion of magnetic nanoparticles," in *Technical Proceedings of the 2013 NSTI Nanotechnology Conference and Expo, NSTI-Nanotech 2013*, vol. 3, pp. 135–138, 2013.

[13] G. Kokkinis, F. Keplinger, and I. Giouroudi, "On-chip microfluidic biosensor using superparamagnetic microparticles.," *Biomicrofluidics*, vol. 7, p. 054117, jan 2013.

[14] P. P. Freitas, R. Ferreira, S. Cardoso, and F. Cardoso, "Magnetoresistive sensors," *Journal of Physics: Condensed Matter*, vol. 19, no. 16, p. 165221, 2007.

[15] F. Li and J. Kosel, "A Magnetic Biosensor System for Detection of E. coli," *Magnetics, IEEE Transactions on*, vol. 49, pp. 3492–3495, jul 2013.

Chapter 4
Publication C

Magnetic-based biomolecule detection using giant magnetoresistance sensors

Authored by G. Kokkinis, M. Jamalieh, S. Cardoso, F. Cardoso, F. Keplinger and I. Giouroudi.
Published in *Journal of Applied Physics,* **vol. 117**, p 17B731, (2015).

Abstract

This paper presents a novel microfluidic chip for *in vitro* detection of biomolecules tagged by magnetic microparticles (MAPs) suspended in a static fluid. The system consists of two microfluidic channels: a reference channel in which bare MAPs are suspended and a detection channel in which magnetically tagged biomolecules are suspended (LMAPs). The LMAPs are functionalized MAPs (of the same magnetic volume as the ones in the reference channel) with attached biomolecules. The overall, non-magnetic volume of the LMAPs is greater than that of the bare MAPs. Current carrying microconductors are positioned underneath the channels in order to impose a magnetic field gradient to the MAPs and LMAPs and move them from the inlet to the outlet of the channels without flow. The innovative aspect of the proposed method is that the induced velocity on the MAPs and LMAPs, while imposed to the same magnetic field gradient, is inversely proportional to their overall, non-magnetic volume. This is due to the enhanced Stokes' drag force exerted on the LMAPs, resulting from the greater volume and altered hydrodynamic shape. This induced velocity is measured by utilizing Giant Magnetoresistance (GMR) sensor pairs fabricated underneath the first and the last microconductors. Detected differences in velocity

between the LMAPs and the reference MAPs indicate the presence of biomolecules in the static liquid sample. We also present a novel method for signal acquisition and demodulation: expensive function generators, data acquisition devices, and lock-in amplifiers were substituted by a generic PC sound card and an algorithm combining the Fast Fourier Transform of the signal with a peak detection routine. Experiments with functionalized MAPs and magnetically tagged *Escherichia Coli* (representing the LMAPs) were carried out as a proof of concept. In order to identify the detection limit of the GMR sensor, single MAP (2.8 µm diameter) detection was performed.

4.1 Introduction

The development of portable, sensitive, and fully automated biochips that directly translate the presence of certain biomolecules (e.g. pathogens, cells, and viruses) into an electronic signal gains interest increasingly. [1] All necessary sample handling and analysis steps are performed within the biochip without the need for established laboratory infrastructure or well-trained personnel. [2] Microfluidic biochips are ideal candidates for such applications. [3–9] They usually consist of a set of units which guarantee the manipulation, detection, and recognition of biomolecules in a reliable and flexible manner. Additionally, the use of magnetic methods for performing the aforementioned tasks has been steadily gaining interest. The typical working principle of other systems that were reported in the literature and use magnetic particles in combination with magnetic sensors for biomolecule detection is based on functionalization of the sensors surface, e.g. with antibodies. Once the magnetically tagged biomolecules are inserted in the microfluidic channel, they are immobilized on the sensors surface. This creates a sandwich structure on top of the magnetic sensor consisting of antibodies, biomolecules and magnetic particles. After rinsing the microfluidic system, the magnetic sensor measures the magnetic field, which is a function of the magnetic particles, and the result is compared to a reference sensor. If biomolecules are present in the liquid sample, the two sensors will produce different signals. [10–16] The greatest disadvantage of this type of biochips is that they are prone to time dependent changes of

this functionalization layer, such as aging and contamination. Long-term stability is therefore an issue with those types of biosensors. Moreover, most of the reported magnetic detection methods require flow which complicates on-chip integration such as additional units, e.g. micropumps are needed. [11,17,18]

In this paper, we present a simple microfluidic chip based on magnetic tagging of biomolecules and magnetic detection without flow, without functionalizing the sensors surface, and without complicated microfluidic structures. The detection unit of the biochip consists of four Giant Magnetoresistance (GMR) spin valve sensors [19, 20] while the infectious agents are tagged with magnetic microparticles (MAPs) using antibodies. With the proposed chip, access is granted to the biomolecules in the whole liquid sample as compared to the sandwich techniques, which have access only to biomolecules, which are in contact with the functionalized surface. *Escherichia Coli* K12 wild type was used to prove the detection principle.

4.2 Experimental

The bare MAPs in the reference channel and the magnetically tagged biomolecules (LMAPs) in the detection channel are manipulated from the inlets towards the outlets only by the magnetic force ($\mathbf{F}_m$) produced by the integrated microconductors. [21–23] Apart from the $\mathbf{F}_m$, other forces are exerted on the MAPs and LMAPs: surface forces (DLVO forces) [24] and the Stokes', drag force, $\mathbf{F}_d$. [25] It is this drag force that depends on the overall, non-magnetic volume of the particle and its hydrodynamic shape. A change in the overall volume of the particle, due to the binding of the biomolecules to its surface, leads to an increased radius ($r' = r_p + d$) and altered hydrodynamic shape. When the fluid is static, $\mathbf{F}_d$ equals $\mathbf{F}_m$, which is constant. This consequently leads to a reduction in the induced velocity as previously proven in: [26]

$$\vec{\mathbf{v}}_p = \frac{r_p^3 \chi}{9\mu_0 \eta r'} \nabla \vec{\mathbf{B}}^2 \tag{4.1}$$

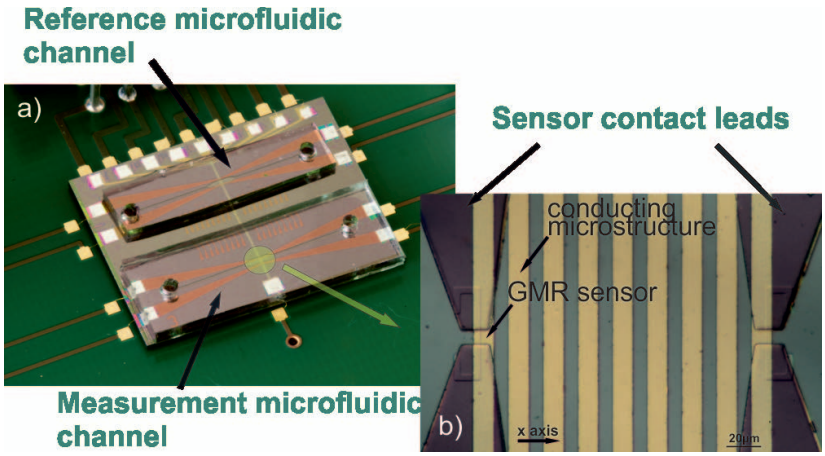

Figure 4.1: (a) Photograph of the proposed lab-on-a-chip pathogen detection system mounted and wirebonded on a PCB board. The reference and measurement microfluidic channels are shown. (b) Microscope image of the GMR sensors with their contact leads and the conducting microstructures.

where r_p is the radius of a spherical particle, χ is the susceptibility of the MAP (assuming the susceptibility of the surrounding medium zero), η is the dynamic viscosity of the medium in which MAPs are suspended, d is the diameter of the attached biomolecule, and $\mathbf{B}$ is the magnetic field density.

Figure 4.1 illustrates the proposed microfluidic biosensor; it consists of two microfluidic channels, one for loading the liquid sample (referred to as the detection channel) and one serving as a reference channel. Both channels were identical. Gold microconductors were fabricated perpendicular to the x direction (Figure 4.1 (b)). A passivation bilayer was protecting the conductors from corrosion and served as surface modification base. The microconductors, which were sequentially switched on and off using a programmable microcontroller, were responsible for the acceleration of the MAPs and LMAPs from the inlet to the outlet of both channels. Underneath the first (inlet) and the last (outlet) microconductors of each channel, GMR, spin valve sensors were fabricated. By measuring the time interval between the resistance change of the inlet sensors and the outlet sensors, the mean velocity of the MAPs and LMAPs during their motion can be calculated.

Figure 4.2 is a schematic representation of the working principle.

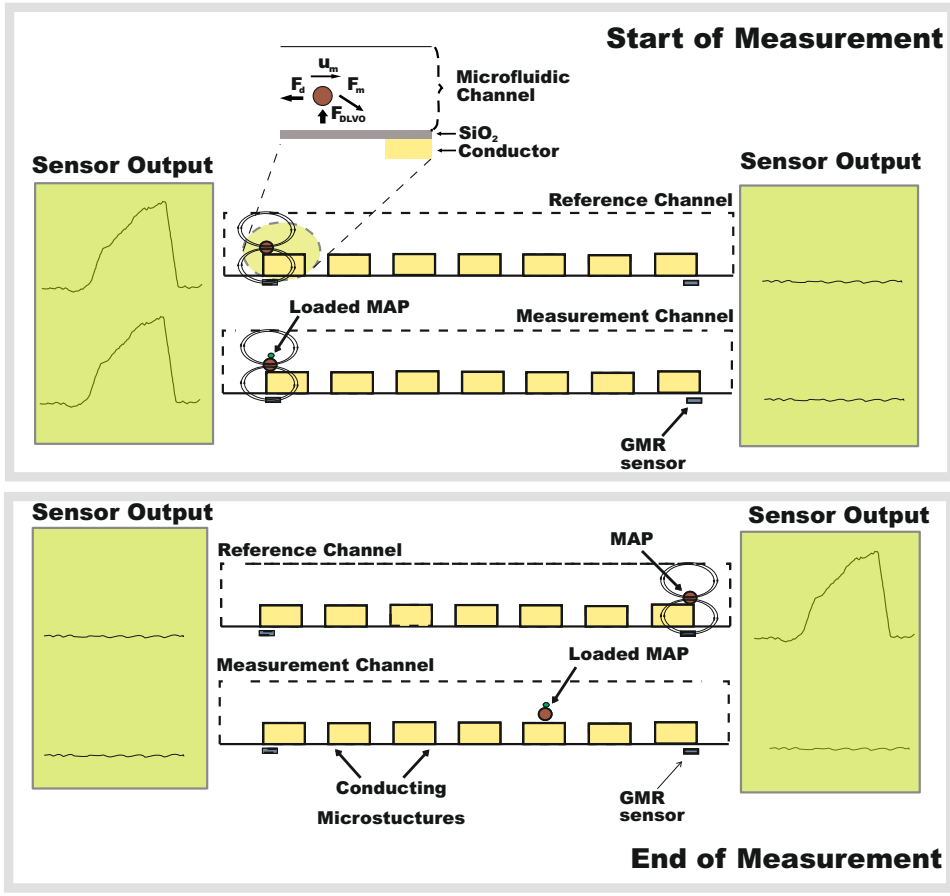

Figure 4.2: The proposed device operation and detection principle and illustration of the forces exerted on the particle.

All four sensors have zero output before the liquid sample with the magnetically tagged biomolecules and the reference suspension of MAPs are introduced into the channels using a pipette. Once the liquids are introduced, a change of signal at the inlet sensors of both channels indicates the presence of MAPs on top of them, thus the initialization of the measurements. Afterwards, the conducting microstructures are sequentially switched on and off accelerating the particles towards the outlet. The actuation time is optimized for continuous motion of bare, unloaded MAPs while LMAPs will fall behind due to their smaller mobility. When the output of the outlet sensor of the reference channel changes from zero the measurement

ends. If the output of the outlet sensor of the detection channel remains zero, it is proven that the reference, bare MAPs travelled the same distance faster than the functionalized MAPs inside the detection channel. This demonstrates that the non-magnetic volume of the functionalized MAPs increased through the binding of biomolecules.

The four GMR spin valve elements were deposited by Ion Beam Deposition (Nordiko 3600 tool) on a silicon 4 in. wafer with a 250 nm SiO_2 and 80 nm Si_3N_4 insulation bilayer, with the following structure: Ta 3 nm/ NiFe 3.6 nm/ MnIr 8.5 nm/ CoFe 2.3 nm/ Ru 0.8 nm/ CoFe 2.3 nm/ Cu 2 nm/ CoFe 3 nm/ NiFe 3.6 nm/ Ta 5 nm. Their dimensions were 6 µm $\times$ 2 µm with the smaller dimension along the sensitive axis. Aluminum sensor contact pads 300 nm in thickness were sputtered in order to provide electrical connection to the sensors. The microconductors were fabricated on top of the sensors, employing standard photolithography and gold evaporation. The resulting thickness was 500 nm with 10 µm width and 10 µm spacing (Figure 4.1 (b)).

Ordyl® SY335 dry negative photoresist was utilized as the mold of the microfluidic channels, upon which a polymeric organosilicon compound, Polydimethylsiloxane (PDMS), was poured, degassed, and cured, resulting into the approximately 25 µm deep channels, as shown in Figure 4.1 (a).

For the experiments presented in this paper *Escherichia Coli* K12 wild type gram negative bacteria were used. They are the perfect candidates for proving the detection principle since they have the

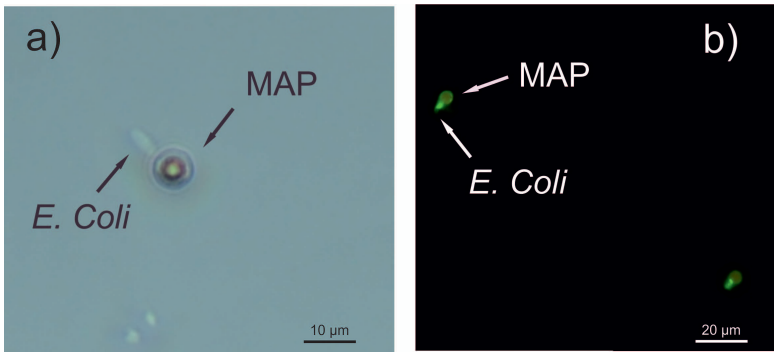

Figure 4.3: Microscope images of loaded MAPs: (a) bright field microscopy image and (b) fluorescent microscopy image.

same size and shape as the pathogenic *E. coli* expressing the enterohemorrhagic serotype O157:H7, one of the most profound food contaminating bacteria. [1] One colony-forming unit of *E. coli* was conjugated with IgG rabbit polyclonal antibodies, specific for the O and K antigenic serotypes of the bacteria. The antibodies were biotinylated through amine-reactive crosslinker chemistry, so that further conjugation to MAPs could take place. Due to very high binding affinity of the streptavidin-biotin interaction ($K_d = 10^{-15}$), commercially available superparamagnetic particles, 2.8 µm in diameter, with a monolayer of recombinant streptavidin covalently coupled to the surface (Dynabeads® M-280 Streptavidin [1]) were chosen. After 30 min of incubation in room temperature the bacteria were attached to the MAPs forming the LMAPs with increased non-magnetic volume (Figure 4.3 (a)). Afterwards, donkey polyclonal secondary antibodies, specific for Rabbit IgG, conjugated with a fluorophore (Alexa Fluor® 488) were incubated for 30 min with the LMAPs' sample for visualization purposes (Figure 4.3 (b)).

The described chip was wire-bonded on a custom made PCB board with BNC connectors for coaxial shielded wiring and placed

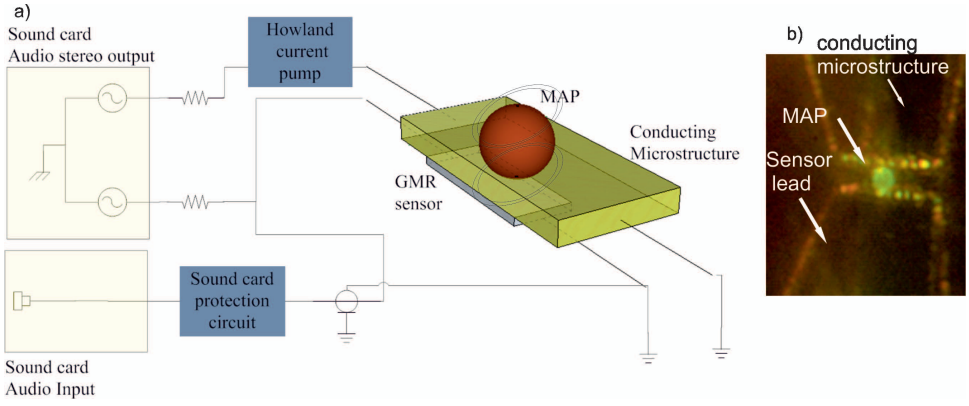

Figure 4.4: (a) Schematic illustration of the measurement and acquisition experimental set-up (not in scale). (b) Combined dark field and fluorescent microscopy image of a MAP attracted by the conducting microstructure and detected by the spin valve GMR sensor.

[1] See https://www.lifetechnologies.com/order/catalog/product/11205D/ for details on the magnetic beads

in such a manner that the sensitive axis of the magnetic sensor is perpendicular to the earth's magnetic field (see Figure 4.1). No additional noise reduction scheme was employed. The PCB was then placed under a fluorescence microscope microscope to observe the course of the experiments.

For the detection of single MAPs, the double frequency modulation technique was used. Even though it is a well established method of detection of MAPs with GMR, spin valve sensors [23,27] it requires expensive and bulky equipment for signal generation, acquisition, and demodulation. In the presented set-up function generators, data acquisition hardware and lock-in amplifiers were substituted by a generic PC sound card and an algorithm combining the Fast Fourier Transform (FFT) of the signal with a peak detection routine. The schematic illustration of the set-up is shown in Figure 4.4. Specifically, the microconductor on top of the sensor was supplied with a current of 20 mA at 234 Hz (f_m). The resulting magnetic field, circumferential to the conductor, magnetized the superparamagnetic MAPs and contributed to the field measured by the GMR sensor together with the stray magnetic field of the MAPs. In order to keep the current constant against thermal fluctuations that would deteriorate the measurement, a Howland current pump [28] was designed and used. The sensor was supplied with a current of 1 mA at 1.234 kHz (f_s), which provided the carrier signal for the modulation of the signal to be measured. This way the latter was moved higher at the spectrum of the sensor making it distinguishable from the flicker ($1/f$) noise, which dominated the lower frequencies. Both currents were provided by a generic PC sound card and the 2 channels stereo output, in particular.

The modulated signal must be demodulated in order to acquire the magnitude of the field generated by the conducting microstructure and the MAP. Typically, this is done by a lock-in amplifier. In our case, the signal from the sensor was supplied to the Line-in input of the sound card, through an overvoltage protection circuit. An algorithm implemented in MATLAB® imported the data stored in soundcard's buffer after the analog to digital conversion. Then, single-sided FFT was performed to the digital signal and a unit conversion to voltage. Further on, the algorithm isolated the peak of the spectrum at the sum of the two frequencies ($f_s + f_m$) in order to

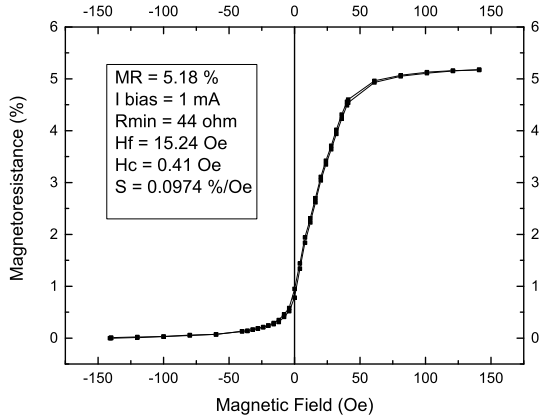

Figure 4.5: Sensors transfer curve, showing the magnetoresistance MR = 5.18%, the magnitude of the current supplied to the sensor during the characterization $I_{bias} = 1\,mA$, the resistance of the sensor at an absence of magnetic field, the ferromagnetic coupling field from the pinned layer $H_f = 15.24\,\text{Oe}$, and the coercivity $H_c = 0.41\,\text{Oe}$.

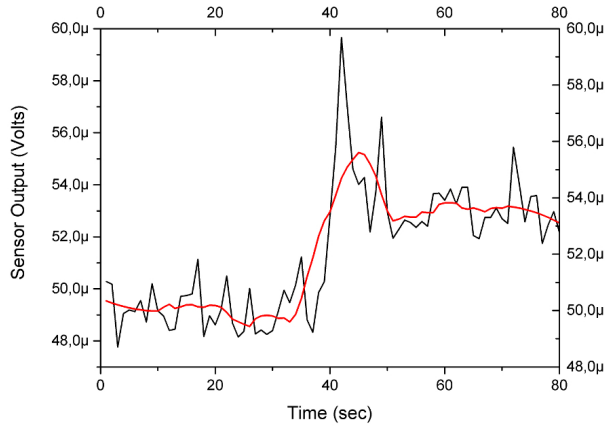

Figure 4.6: Graph acquired during the detection of a single MAP showing the sensors output over time. The red line is a second order polynomial fitting to the raw data.

avoid crosstalk, [29] and plotted it over time. Once the plotted value surpassed a predetermined threshold corresponding to the magnetic field of the conductor alone, the program terminated and a control signal was send to the microcontroller in order for the acceleration of the MAPs and LMAPs to start (through the sequential switching of 7 microconductors). 50 mA DC current was passed through the conductors. The duration that each conductor remained switched on was decided upon the mean time a non-loaded MAP needed to travel from one conductor to the next; in our case, for the 2.8 μm particles, it was set at 3.81 sec, corresponding to a mean velocity of 3.25 μm/sec.

4.3 Results and discussion

For a current of 20 mA amplitude, the x component (with x being the sensitive axis of the sensor) of the magnetic field averaged on the sensor's volume was $H_{cond,x} = 9.948$ Oe without the presence of a MAP. A MAPs stray field (x component) was evaluated at $H_{stray,x} = 0.1934$ Oe.

The GMR sensors were characterized using Helmholtz coils, which provided the magnetic field parallel to the sensor's sensitive axis; the acquired transfer curve is shown in Figure 4.5. It is apparent that the sensor exhibits a relatively big ferromagnetic coupling field from the pinned layer [30] ($H_f = 15.24$ Oe) or offset. Although this is not a desirable trait, it was still adequate for our sensing method. Since the AC magnetic field from the conducting microstructure was evaluated at approximately 10 Oe(x component), we conclude that the sensor was saturated, which induced harmonics to the spectrum of the sensor, but did not prevent the detection of a single MAP as seen in Figure 4.6. The lower plateau of the graph corresponds to the approximately 10 Oe(x component) magnetic field exerted from the microconductor. The average value is V_{out} = 49.25 μV. When a single MAP is attracted by the magnetic field gradient and immobilized directly above the sensor, the average value of the sensor's output increases to V_{out} = 53.35 μV, suggesting a change of 4.1 μV (or 8.33%) due to the MAP's stray field, which was evaluated at $H_{stray,x} = 0.1934$ Oe. After detection of particles from the inlet sensors of both channels, the acceleration process took place with a

switching interval set at 3.81 sec. The MAPs in the reference channel indeed traveled through all the conductors reaching the outlet sensor (where they were again detected signifying the end of the process), while the loaded MAPs would need a time interval of 6.15 sec.

4.4 Conclusion

In this work, a novel microfluidic chip with integrated GMR sensors for *in vitro* detection of biomolecules attached to magnetic microparticles (MAPs) was presented. Single MAPs were successfully detected from the GMR sensor. A velocity change between magnetically tagged *E. coli* bacteria and bare MAPs was also successfully recorded. It has to be mentioned that this method is not used to quantify the biomolecules in the sample under investigation but rather to prove the presence of the biomolecules.

Acknowledgements

ISAS acknowledges the financial support of the Austrian Science Fund (FWF) with Project No. P 24372- N19. INESC-MN acknowledges FCT funding through the IN Associated Laboratory.

Bibliography

[1] W.-C. W. Tian and E. Finehout, "Microfluidic Diagnostic Systems for the Rapid Detection and Quantification of Pathogens," in *Microfluidics for Biological Applications*, pp. 271–322, Springer, 2008.

[2] J. Mairhofer, K. Roppert, and P. Ertl, "Microfluidic systems for pathogen sensing: A review," *Sensors (Switzerland)*, vol. 9, no. 6, pp. 4804–4823, 2009.

[3] K.-K. Liu, R.-G. Wu, Y.-J. Chuang, H. S. Khoo, S.-H. Huang, and F.-G. Tseng, "Microfluidic systems for biosensing.," *Sensors (Basel, Switzerland)*, vol. 10, pp. 6623–61, jan 2010.

[4] J. Loureiro, C. Fermon, M. Pannetier-Lecoeur, G. Arrias, R. Ferreira, S. Cardoso, and P. Freitas, "Magnetoresistive Detection of Magnetic

Beads Flowing at High Speed in Microfluidic Channels," *IEEE Transactions on Magnetics*, vol. 45, pp. 4873–4876, oct 2009.

[5] A. K. Balasubramanian, A. Beskok, and S. D. Pillai, "In situ analysis of bacterial capture in a microfluidic channel," *Journal of Micromechanics and Microengineering*, vol. 17, pp. 1467–1478, aug 2007.

[6] J. Chen, D. Chen, Y. Xie, T. Yuan, and X. Chen, "Progress of Microfluidics for Biology and Medicine," *NANO-MICRO LETTERS*, vol. 5, no. March, pp. 66–80, 2013.

[7] K.-S. Yun, D. Lee, H.-S. Kim, and E. Yoon, "A microfluidic chip for measurement of biomolecules using a microbead-based quantum dot fluorescence assay," *Measurement Science and Technology*, vol. 17, pp. 3178–3183, dec 2006.

[8] L. Y. Yeo, H.-C. Chang, P. P. Y. Chan, and J. R. Friend, "Microfluidic devices for bioapplications.," *Small (Weinheim an der Bergstrasse, Germany)*, vol. 7, pp. 12–48, jan 2011.

[9] K. S. Kim and J.-K. Park, "Magnetic force-based multiplexed immunoassay using superparamagnetic nanoparticles in microfluidic channel.," *Lab on a chip*, vol. 5, pp. 657–64, jun 2005.

[10] M. Mujika, S. Arana, E. Castaño, M. Tijero, R. Vilares, J. M. Ruano-López, a. Cruz, L. Sainz, and J. Berganza, "Magnetoresistive immunosensor for the detection of Escherichia coli O157:H7 including a microfluidic network.," *Biosensors & bioelectronics*, vol. 24, pp. 1253–8, jan 2009.

[11] S.-Y. Yang, K.-Y. Lien, K.-J. Huang, H.-Y. Lei, and G.-B. Lee, "Micro flow cytometry utilizing a magnetic bead-based immunoassay for rapid virus detection," *Biosensors and Bioelectronics*, vol. 24, pp. 855–862, dec 2008.

[12] L. Xu, H. Yu, M. Akhras, and S. Han, "Giant magnetoresistive biochip for DNA detection and HPV genotyping," *Biosensors & Bioelectronics*, vol. 24, no. 1, pp. 99–103, 2008.

[13] C. S. Lee, H. Lee, and R. M. Westervelt, "Microelectromagnets for the control of magnetic nanoparticles," *Applied Physics Letters*, vol. 79, no. 20, p. 3308, 2001.

[14] A. Rida, V. Fernandez, and M. a. M. Gijs, "Long-range transport of magnetic microbeads using simple planar coils placed in a uniform

magnetostatic field," *Applied Physics Letters*, vol. 83, no. 12, p. 2396, 2003.

[15] T. Deng, G. M. Whitesides, M. Radhakrishnan, G. Zabow, and M. Prentiss, "Manipulation of magnetic microbeads in suspension using micromagnetic systems fabricated with soft lithography," *Applied Physics Letters*, vol. 78, no. 12, p. 1775, 2001.

[16] J. Schotter, P. B. Kamp, A. Becker, A. Pühler, G. Reiss, and H. Brückl, "Comparison of a prototype magnetoresistive biosensor to standard fluorescent DNA detection.," *Biosensors & bioelectronics*, vol. 19, pp. 1149–56, may 2004.

[17] A. C. Fernandes, C. M. Duarte, F. a. Cardoso, R. Bexiga, S. Cardoso, and P. P. Freitas, "Lab-on-chip cytometry based on magnetoresistive sensors for bacteria detection in milk.," *Sensors (Basel, Switzerland)*, vol. 14, pp. 15496–524, jan 2014.

[18] A. C. Mak, S. J. Osterfeld, H. Yu, S. X. Wang, R. W. Davis, O. a. Jejelowo, and N. Pourmand, "Sensitive giant magnetoresistive-based immunoassay for multiplex mycotoxin detection.," *Biosensors & bioelectronics*, vol. 25, pp. 1635–9, mar 2010.

[19] P. Freitas, F. Silva, N. Oliveira, L. Melo, L. Costa, and N. Almeida, "Spin valve sensors," *Sensors and Actuators A: Physical*, vol. 81, pp. 2–8, apr 2000.

[20] G. Li, S. Sun, R. J. Wilson, R. L. White, N. Pourmand, and S. X. Wang, "Spin valve sensors for ultrasensitive detection of superparamagnetic nanoparticles for biological applications," *Sensors and Actuators A: Physical*, vol. 126, pp. 98–106, jan 2006.

[21] C. Liu, L. Lagae, R. Wirix-Speetjens, and G. Borghs, "On-chip separation of magnetic particles with different magnetophoretic mobilities," *Journal of Applied Physics*, vol. 101, no. 2, p. 024913, 2007.

[22] H. Watarai, M. Suwa, and Y. Iiguni, "Magnetophoresis and electromagnetophoresis of microparticles in liquids," *Analytical and Bioanalytical Chemistry*, vol. 378, no. 7, pp. 1693–1699, 2003.

[23] G. Kokkinis, S. F. Cardoso, F. A. Cardoso, and I. Giouroudi, "Microfluidics for the Rapid Detection of Pathogens Using Giant Magnetoresistance Sensors," *IEEE Transactions on Magnetics*, vol. 50, pp. 2–5, nov 2014.

[24] J. J. N. Israelachvili, *Intermolecular and Surface forces*. Academic press, 2011.

[25] B. J. Kirby, *Micro-and nanoscale fluid mechanics: transport in microfluidic devices*. Cambridge University Press, 2010.

[26] I. Giouroudi, S. van den Driesche, J. Kosel, R. Grossinger, and M. J. Vellekoop, "On-chip bio-analyte detection utilizing the velocity of magnetic microparticles in a fluid," *Journal of Applied Physics*, vol. 109, no. 7, p. 07B304, 2011.

[27] F. Li and J. Kosel, "A Magnetic Biosensor System for Detection of E. coli," *Magnetics, IEEE Transactions on*, vol. 49, pp. 3492–3495, jul 2013.

[28] J. J. Carr, *Linear IC Applications: A Designer's Handbook*. Newnes, 1996.

[29] B. M. de Boer, J. a. H. M. Kahlman, T. P. G. H. Jansen, H. Duric, and J. Veen, "An integrated and sensitive detection platform for magneto-resistive biosensors.," *Biosensors & bioelectronics*, vol. 22, pp. 2366–70, apr 2007.

[30] M. Joodaki, *Selected advances in nanoelectronic devices: logic, memory and RF*, vol. 175. Springer Science & Business Media, 2012.

Chapter 5
Publication D

A microfluidic, dual-purpose sensor for *in vitro* detection of Enterobacteriaceae and biotinylated antibodies

Authored by G. Kokkinis, B. Plochberger, S. Cardoso, F. Keplinger and I. Giouroudi.
Published in *Lab on a Chip*, **vol. 16**, pp 1261 - 1271, (2016).

Abstract

In this paper, we present a versatile, dual-purpose sensor for *in vitro* detection of Enterobacteriaceae (e.g. *Escherichia coli*) and biotinylated antibodies (e.g. IgG rabbit polyclonal antibodies), based on different detection principles for each bioanalyte. These bioanalytes are tagged individually with functionalized magnetic microparticles, suspended into a static fluid and injected into a microfluidic channel. Without the need for bulk or complicated pumping systems, the functionalized microparticles are set in motion by a magnetic force exerted on them by integrated microconductors. The fundamental detection principle is the decrease in the velocity of the microparticles that are loaded with the respective bioanalyte, due to factors inhibiting their motion. The velocity of the unloaded, bare microparticles is used as a reference. We discovered a novel mechanism on which the constrained particle motion is based; in the case of *E. coli*, the inhibiting factor is the enhanced Stokes' drag force due to the greater volume and altered hydrodynamic shape, whereas in the case of biotinylated antibodies, it is the increased friction force at the interface between the modified microparticle and the biosensor's surface. Friction force is for the first time employed in a scheme

for resolving biomolecules. Integrated magnetic microsensors are used for the velocity measurements by detecting the microparticles' stray field. Moreover, we developed a biocompatible, easy to implement and reliable surface modification that practically diminishes the problem of bioadhesion on the sensor's surface.

5.1 Introduction

Enterobacteriaceae (e.g. *E. coli*) are considered to be the most common causative agents of food and waterborne diseases. Enterobacter infections are responsible for thousands of deaths annually, [1] while prominent health institutions like the World Health Organization (WHO)[1] are trying to tackle the increasing antimicrobial resistance (AMR), by means of the appropriate use of antimicrobials and adequate diagnostics. Rapid diagnostics can substantially address those issues. [2]

Another analyte gaining considerable attention in diagnostics are the serum auto-antibodies due to their biomedical relevance. Systemic auto-antibody detection would facilitate the diagnostics of autoimmune disorders and evaluate their treatment and the sustained damage in organs. [3] More interestingly, the presence of certain antibodies in the system is considered an increasingly important expression of diseases such as some types of cancer. [4]

Most of the existing laboratory techniques to identify suspected pathogens use culturing techniques to grow colonies large enough to identify. Other diagnostic methods such as flow cytometry, fluorescence probe detection and optical particle detection employ microscopy or fluorescence microscopy which is expensive and time consuming.[2] [5, 6] Nevertheless, there exist methods which do not require a large amount of sample and provide rapid identification, without the disadvantages of microscopy such as immunological tests (e.g. ELISA immunoassays) and nucleic acid based diagnos-

[1] World Health Organization, Fact Sheet for Antimicrobial Resistance, http://www.who.int/mediacentre/factsheets/fs194/en/, 2015.

[2] BD Biosciences, Instrument Brochure, http://www.bdbiosciences.com/eu/s/flowcytometry, 2015

tics.[3,4] [7–10] Yet, these methods either require established laboratory infrastructure and well-trained personnel or are technologically complex and expensive to fabricate. Moreover, even though they are highly sensitive and specific, false positive and negative results may occur. These results can be caused by improper sample storage or treatment, improper washing methods or reagent deterioration. As far as antibody detection is concerned, ELISA is again the technique mostly used to detect and quantify those antibodies, manifesting the same limitations.

Therefore, the development of portable, sensitive and fully automated biosensors that directly translate the presence of certain analytes into an electronic signal gains increasing interest. [11] All necessary sample handling and analysis steps are performed within the biosensor without the need for established laboratory infrastructure or well-trained personnel.

Microfluidic biosensing platforms are ideal for addressing the demand for such systems. Several biosensors utilizing different physical properties and detection principles have been proposed, [12–18] with magnetic biosensors yielding promising results. [19–23] However, the main disadvantages of these platforms are low flexibility, complicated microfluidic structures and pumping mechanics.

Our microfluidic biosensor, contrary to culture methods, can accurately and rapidly identify only a small number (e.g. a few tens) of pathogens due to magnetic labelling and the novel detection mechanism (section 4). Moreover, the detection procedure (using magnetic microsensors) eliminates the disadvantages of microscopy.

The main advantage of our approach over other cheap and fast diagnostic platforms lies on the fact that there is no specific molecular interaction that provides the results, such as that obtained by using ELISA, but instead the quantitative results are obtained by magnetically driven motion and its alternation (velocity change). Thus, our biosensor is insusceptible to common problems occurring in biosensing techniques such as wrong concentrations, buffer solutions or nonspecific interactions.

[3] Alere Inc., Rapid diagnostic test developer, http://www.alere.com, 2013.

[4] Micronics Inc., Developer of near patient *in vitro* diagnostic products, www.micronics.net, 2013.

Specifically, the presented microfluidic biosensor combines labeling of the analytes with magnetic microparticles (MPs), [22] magnetophoretic manipulation of the tagged bioanalytes suspended in a static fluid (without flow) through integrated microconductors (MCs) and indirect evaluation of their velocity utilizing spin valve (giant magnetoresistance, GMR) sensors. [24] Any difference in the evaluated velocity of the microparticles conjugated with the analytes (henceforth referred to as loaded microparticles, LMPs) due to factors hindering their motion with respect to a reference velocity, evaluated for unloaded MPs, yields positive results. The factors hindering the MPs' motion are different for each type of bioanalyte.

Capturing of *E. coli* is achieved using specific antibodies which are then conjugated to the MPs, while the detection of antibodies requires their biotinylation and immobilization on the MPs' surface through the streptavidinbiotin interaction. The conjugation process will be described in detail in Section 5.3. When injected into the microfluidic channel and in the absence of flow, the MPs are manipulated by sequentially actuated MCs inducing a traveling magnetic field gradient, attracting the MPs and moving them along the channel. In the case of *E. coli* conjugated to the MPs (henceforth referred to as bacteria loaded magnetic particles, BLMPs), the greater hydrodynamic volume (while the magnetic volume remains constant) and the altered shape result in an enhanced Stokes' drag force [25] and thus to a reduction in their velocity while in suspension. In the case of biotinylated antibodies conjugated to the MPs (henceforth referred to as antibody loaded magnetic particles, ALMPs), the overall volume of the compound also increases but to a negligible extent. The effect that slows down the ALMPs with respect to bare MPs in this case is the increased friction force between the ALMPs and the chip's surface. This effect is explained theoretically in Section 5.2 and proven experimentally through atomic force microscopy (AFM) measurements in Section 5.5.

Among others, the significance of the presented work lies on the fact that for the first time we present an alternative method for resolving biomolecules (i.e. biotinylated antibodies) based on the frictional interaction between tagged biomolecules and surfaces, a principle that could lead to the development of methods akin to chromatography and capillary electrophoresis. [26, 27]

Friction forces are critical for the development of microelectromechanical systems (MEMS) and biosensors. [28] A lot of the proposed systems are based on the manipulation of particles, biological entities etc. Several particle manipulation techniques bring the suspended particles in contact with the chip's surface, while exerting magnetic forces on them. [29,30] Unfortunately, the most commonly used materials, such as silicon dioxide (SiO_2) or silicon nitride (Si_3N_4), exhibit bioadhesion making them inappropriate for such applications. Another innovation of the presented work is the development of a biocompatible, easy to implement and reliable surface modification that practically diminishes the problem of biological entities being immobilized on the biosensor's surface which otherwise would render it inadequate for MPs' manipulation and multiple diagnostic tests.

5.2 Theoretical analysis

A better understanding of the detection principle is achieved by analysing the forces that act on a single particle (MP). Figure 5.1 (c) shows the forces exerted on a single particle by a single MC. The magnetic force is given by the following equation: [31]

$$\vec{\mathbf{F}}_m = \frac{V_b \Delta\chi}{\mu_0}(\vec{\mathbf{B}} \cdot \nabla)\vec{\mathbf{B}} \tag{5.1}$$

where V_b is the volume of the MP, μ_0 is the permeability of the vacuum ($4\pi \times 10^{-7}$ H/m), χ is the magnetic susceptibility of the MP, and $\mathbf{B}$ is the magnetic flux density. The equation neglects the magnetic susceptibility of the medium in which the MPs are suspended as well as the initial magnetization of the MPs as they exhibit superparamagnetic behavior according to the manufacturer's magnetization curve. [32] The small size of the MCs, as shown in Figure 5.1 (b), is ideal for inducing sharp magnetic field gradients, thus enhancing the magnetic force exerted on the MPs, as well as for tuning the magnitude of the force with restrictions due to temperature and electromigration. [33]

The main force opposing the movement of the MPs in suspension is the frictional Stokes' drag force, deriving from the Navier - Stokes differential equation for small Reynold's numbers and small spheri-

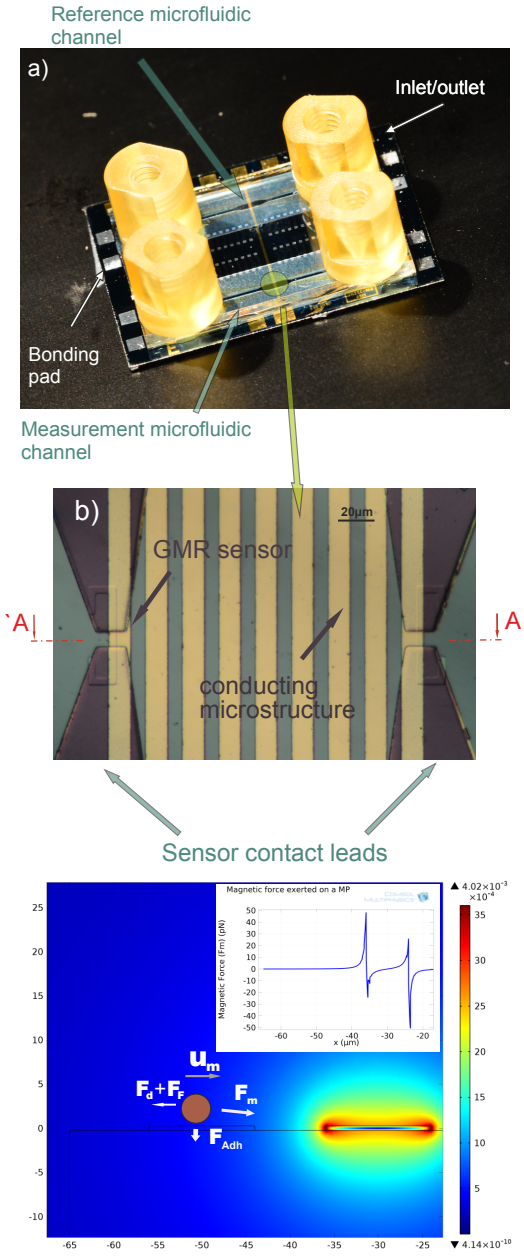

Figure 5.1: (a) The developed biosensor with the integrated microfluidic channels, (b) microscopy image upon 20x magnification; the sensor contact leads, the GMR elements and the sequential MCs are shown. (c) Force analysis on a single MP, finite element analysis of the magnetic field imposed by the current carrying MC, which attracts the MP. The view is the hypothetical cross section (A'A) of the biosensor as seen in (b). (Inset) A graph of the magnetic force exerted on the MP along the axis of motion (x). The peaks are located at the edges of the MC.

cal particles, acting on the interface between the fluid and the MP. It is given by the following equation: [34]

$$\vec{\mathbf{F}}_d = -3\pi D\eta\vec{\mathbf{v}} \tag{5.2}$$

where D is the diameter of the MP, η is the viscosity of the medium, and $\mathbf{v}$ is the relative velocity of the fluid with respect to the MP. While the equation adequately approximates the force acting on the spherical MPs (like the ones in the reference channel), it fails to do so for the LMPs. Thus, a shape correction factor should be introduced. An eccentricity approximation is also not favorable, whereas the Corey shape function performs best. [35] The correction factor is given by:

$$f_{shape} = \left(\frac{d_{max}d_{med}}{d_{min}}\right) \tag{5.3}$$

where d is the LMPs' dimensions: the particle's longest dimension (d_{max}), the shortest dimension (d_{min}), and the intermediate or medium dimension (d_{med}).

During the sliding of the MPs on the chip's surface, a friction force is exerted on them. Friction between two solid surfaces on the microscale and nanoscale involves complicated physical phenomena that are beyond the scope of this paper and are extensively reported in the literature. [36–39] In the present work, we focus on providing the necessary elements for a qualitative analysis of the friction based on recently proposed models. The friction in the developed system can be modeled as two solid surfaces in sliding, relative motion with a molecularly thin film (the surface modification) confined between them, with low shear rates and smooth asperities. Such conditions classify the interfacial friction to the boundary tribological regime. [40,41] As AFM experiments show (Section 5.5), the two surfaces are in adhesive contact. Consequently, Amonton's law cannot sufficiently describe the friction; therefore, a more appropriate approach is given by the cobblestone model where friction force is evaluated as follows: [42]

$$F = F_F = S_c A + \mu L \tag{5.4}$$

where S_c is the critical shear stress (assumed to be constant), A is the contact area, μ is the friction coefficient and L is the load. The

equation implies that there are two contributors to the forces between the two surfaces: the externally applied load and the intrinsic intermolecular forces that define the adhesion between the two surfaces.

The surfaces involved in relative motion in the developed system are quite complex: on the one hand, a protein (streptavidin or antibodies) covered sphere and, on the other hand, a hydrogel flat surface. As it can easily be deducted, the definition of the intermolecular forces at the interface cannot be solely explained with the DLVO theory (named after Derjaguin and Landau, Verwey and Overbeek). [43, 44] For the qualitative study and the proof of concept of the biosensor, the determination of the adhesive nature of the interaction is sufficient and accurate. Further analysis of the additional forces involved which sum up to the principally adhesive forces, such as solvation, entropic, hydrophobic forces etc., is out of the scope of this paper. [45]

5.3 Material and methods

5.3.1 Device fabrication

Figure 5.1 shows the developed biosensor with the integrated microfluidic channels and the integrated GMR sensors. The GMR sensors were fabricated as follows: a thin film spin valve stack was deposited in a Nordiko 3000 Ion Beam Deposition device. The stack had the following structure (thickness in nm, compositions in atomic percentage): Ta 3.0/ $Ni_{80}Fe_{20}$ 3.6/ $Mn_{76}Ir_{24}$ 8.5/ $Co_{80}Fe_{20}$ 2.3/ Rn 0.8/ Cu 3.0/ $Co_{80}Fe_{20}$ 3.0/ $Ni_{80}Fe_{20}$ 3.6/ Ta 5.0. A 3 mT magnetic field was applied during the deposition in order to induce a parallel anisotropy for the free and pinned layer easy axis. [46] The final structures as shown in Figure 5.1 were defined using standard photolithography and an ion milling etching process carried out using a Nordiko 3600 device. 300 nm aluminum contact leads to the sensors were fabricated using again photolithography and an aluminum spattering process with the latter carried out using a Nordico 7000 device. The sensors were then passivated with a 15 nm thick TiW layer deposited in the aforementioned device. The MC fabrication and the finalization of the chips' surface have been reported in detail. [24]

The microfluidic channels were fabricated as follows: the wafer was immersed in a 10% RBS 50 basic solution in deionized (DI) water and in an ultrasonic bath for 2 hours to remove potential contaminants present from the previous steps and dried for 30 min at 120 °C. Then, a 55 µm thick, negative type, dry-film, photoresist (Ordyl®) was laminated using a standard office laminator and exposed for 21 sec using a Karl Suss MA-150 Mask Aligner; a 60 sec post exposure bake at 85 °C on a hot plate followed. The exposed photoresist was developed for 1.5 min in 3 successive developer baths of increasing cleanness and rinsed with isopropanol and DI water. For the sealing of the channels, a cleaned (in the aforementioned solution) and cut glass slide was used, in which inlet and outlet holes were opened using a sand blasting device (BEGO Inc., Duostar®). The chip and the sealing slide were then bonded by applying a force of $60\,N$ per cm^2 of photoresist. The temperature was increased to 100 °C with a 5 °C/min ramp and maintained for 30 min. Then, the temperature was reduced to room temperature at 1 °C/min. A DAD 3220 dicing saw with a 200 µm thick diamond blade was used to cut the bonded wafers into single chips. The inlet and outlet holes in the glass wafer were sealed with adhesive tape before dicing to prevent cooling water and debris from entering the chips. To free the contact pads, the glass wafer was partially removed in the areas above the pads. This was performed by dicing the chip halfway through, dicing only through the glass wafer and using the Ordyl® layer as a spacer that prevented the MCs and the contact pads from getting damaged.

5.3.2 Antibody loaded magnetic particle preparation

Life Technologies® Dynabeads® M-280 with covalently coupled recombinant streptavidin and a tosyl-activated, hydrophobic surface functionality have served as the basis for analyte (i.e. antibodies, *E. coli*) conjugation and sample preparation throughout the experiments. 100 µl of Dynabeads® M-280 (10 mg/ml concentration) was mixed with 900 µl of 0.01 M phosphate-buffered saline (PBS) - Tween (0.01% v/v) buffer, then washed 3 times with magnetic separation and resuspended in 1 ml of PBS - Tween. 7 µl of rabbit polyclonal antibodies to *E. coli* (Abcam® ab20640) covalently coupled with the

N-hydroxysuccinimide ester of biotin was added and incubated for 30 min at room temperature. Then, the particles conjugated with the IgG were washed 5 times by magnetic separation and resuspended in 1 ml of 0.01 M PBS - BSA (0.1% w/v). 3 µl of donkey polyclonal secondary antibody to rabbit IgG H&L (conjugated with the fluorophore Alexa Fluor® 488) was added and incubated for 30 min at room temperature for visualization purposes.

5.3.3 Bacteria loaded magnetic particle preparation

One colony-forming unit (CFU) of *Escherichia coli* of the K12 wild type strain was suspended in 1 ml of 0.01 M PBS - Tween 20 (0.01% v/v), washed 3 times utilizing centrifugal separation and resuspended in the original volume. 7 ml of ab20640 antibodies with a concentration of 4 mg/ml was added and incubated for 30 min at room temperature, washed 5 times by centrifugal separation and resuspended in 100 µl of 0.01 M PBS - BSA (0.1% w/v). The Dynabeads® M-280 were washed using the same process as the one described in the ALMP preparation section and condensed in 100 µl of 0.01 M PBS - Tween 20 (0.01% v/v). 40 µl of the *E.coli* (conjugated with antibodies) solution was mixed with 1 µl of the Dynabeads® M-280 washed solution and was incubated for 30 min at room temperature. 200 µl of 0.01 M PBS - BSA (0.1% w/v) was added and then washed once by magnetic separation. 1 µl of donkey polyclonal secondary antibody to rabbit IgG H&L (conjugated with the fluorophore Alexa Fluor®488) was added and incubated for 30 min at room temperature for visualization purposes.

5.3.4 Surface modification

A single chip was washed by three consecutive rinses with acetone, isopropanol and DI water to remove any contaminants. Then, it was left to dry on a hot plate for 30 min at 150 °C. Oxygen plasma was employed for the hydroxylation of the SiO_2 surface (30 sec oxygen plasma, 100 watt forward power, 30 sccm O_2). Afterwards, the chip was dipped for 10 min in a 2 g/l branched, polyethyleneimine (Mw $\approx$ 24.000 by LS, Sigma - Aldrich®) solution in DI water and then rinsed with DI water. Another dip for 10 min in 2 g/l sodium alginate

(alginic acid sodium salt, Sigma-Aldrich®) followed by a DI water rinse finalizes the antifouling surface modification.

5.3.5 AFM tip functionalization

Si_3N_4 cantilever tips were stepwise chemically modified for friction and adhesion measurements. Commercially available silicon AFM cantilevers (MSNL-10, Veeco Instruments) were cleaned with chloroform (3 times), dried with N_2 and stored in PBS buffer (tip 1: Si_3N_4 tip). The cleaned silicon AFM cantilevers were additionally amino-functionalized via gas-phase silanization with aminopropyltriethoxysilane (APTES) as described in reference [47]. A heterobifunctional linker (aldehydebiotin) was prepared as described in reference [48]. Briefly, 3.3 mg of a linker (Nanocs, Biotin-PEG-NHS, MW 3400) was dissolved in 0.5 ml of chloroform and transferred into a small glass reaction chamber. 30 µl of trimethylamine was added, and the ethanolamine-coated AFM tips were immediately immersed for two hours. Subsequently, the tips were washed with chloroform and dried with N_2 gas. After rinsing with chloroform and drying, the tips were immersed for 60 min in a 50 µg/ml streptavidin solution, then washed and stored in PBS buffer (tip 2: streptavidin (SA) tip). Finally, streptavidin coated tips were incubated for 60 min with biotinylated antibodies, washed and stored in PBS buffer (tip 3: antibody tip).

5.3.6 Combined fluorescence microscopy and atomic force microscopy

The sample was sealed in a home-built chamber and rinsed with PBS. AFM measurements were performed using a Nano - Wizard 3 (JPK Instruments AG, Germany) system mounted on an Axiovert 200 inverted microscope (Carl Zeiss AG, Germany). The microscope is equipped with a 100x NA = 1.46 oil-immersion Plan-Apochromat TIRFM objective (Olympus, Japan). Samples were illuminated in objective-type, total internal reflection (TIR) configuration via the epiport using 488 nm (250 nW) and 647 nm (250 mW) light from a diode laser (Toptica 250 mW, Toptica Photonics, Germany) or 532 nm light from a solid state laser (Millennia X, Spectra Physics, USA),

with intensities of 310 kW/cm^2. After appropriate filtering, emitted signals were imaged using a back-illuminated, TE-cooled CCD camera (Andor iXon Du-897 BV, UK). For the precise control of the illumination timings, we used acousto-optical modulators (1205C, Isomet, USA). Timing protocols were generated by an in-house program package implemented in LABVIEW (National Instruments, USA). Illumination times were adjusted to values between 1 and 5 msec. The particle on the apex of the tip was first imaged using a fluorescence microscope to determine the lateral movement of the bead during scanning. Topographical and friction images were recorded in contact mode by keeping the vertical deflection constant and analyzed. Adhesion and elasticity measurements were recorded in quantitative imaging mode (QI mode) at room temperature in liquid (PBS) at a resolution of 128×128 pixels. The maximum force applied for adhesion measurements, determined by the vertical deflection of the cantilever, was set to 300 pN. Force distance cycles (scan rates) were controlled by the z length (250 nm), extension time (10 msec) and retraction time (50 msec). We used uncoated silicon cantilevers (MSNL-10, Bruker Corporation, USA) with a nominal spring constant in the range of 0.01 0.03 N/m. The spring constant for each cantilever was calibrated using the thermal noise method. [49–52] JPK data processing (JPK Instrument, Germany) software was used for image processing and estimation of the adhesion force and indentation. The height, adhesion and slope of the force curve were collected simultaneously in both trace and retrace directions. Height images were line-fitted as required. Isolated scan lines were occasionally removed. The Young's modulus was estimated from the force curve by using the JPK data processing software with the following settings: model (cantilever tip): cone; opening angle (cantilever tip): 35°, Poisson ratio: 0.5; method: Hertz model.

5.4 Experimental

The microfluidic channel walls were fabricated utilizing standard photolithography techniques on a negative dry photoresist laminated on the biosensor's surface (Ordyl® 350Y) with 50 µm thickness while the length of the channel was 10 mm and the width var-

ied between 90 µm and 500 µm. The maximum feature size of the microfluidic channel is dictated by the surface area of the developed photoresist so as to not inhibit or impede the bonding. [53] As a final step, a glass slide with sand-blasted inlets and outlets was bonded on the photoresist sealing the channels. This fabrication technique provides the significant advantage of automatic, pump-less priming over polydimethylsiloxane (PDMS) channels, due to the hydrophilicity of the glass and the biosensor's surface. Thus, the channels are being filled solely due to capillary forces. [54]

The commercially available magnetic microparticles, Dynabeads® M-280 which were used for the preliminary experiments, are uniform, superparamagnetic, porous polystyrene spheres with an even dispersion of magnetic material throughout the particle. The magnetic material within the Dynabeads is a mixture of two iron oxides, maghemite (gamma - Fe_2O_3) and magnetite (Fe_3O_4), which is encased in the bead matrix by an additional thin polymer shell (monodispersity: SD 0.04 - 0.05 µm and CV 1.6 - 1.8%, density: 1.6 g/cm^3).[5] These MPs, with a layer of covalently coupled recombinant streptavidin to the surface, are an ideal candidate for conjugation processes due to the high affinity of streptavidin to biotin ($K_d = 10^{-15}$) while their superparamagnetic properties allow for high magnetophoretic mobility and rules out particle agglomeration.

The developed biosensor consists of two microfluidic channels; one is the measurement channel where the sample with the LMPs is injected and another is used as the reference channel, where the reference sample is injected. The reference sample is ALMPs when we want to detect *E. coli* and plain unloaded MPs for the detection of biotinylated antibodies. Once the samples are inserted into the channels, the magnetophoretic manipulation of the particles (MPs and LMPs) takes place. Superparamagnetic particles single or engulfed in a polymer matrix move towards an increasing magnetic flux density gradient.

This gradient is provided by integrated planar microconductors (MCs) fabricated perpendicular to the MPs' motion as shown in Figure 5.1 (b). Since this gradient is especially sharp, as finite element method simulations suggest (Figure 5.1 (c), inset), it can effectively

[5] ThermoFisher Scientific, Dynabeads® M-280 Streptavidin, https://www.thermofisher.com/order/catalog/product/11205D, 2015.

move the MP over a limited distance of a few micrometers. Hence, an array of 9 conductors was fabricated to move the MPs over a distance of 180 µm, the manipulation area (MA), by switching OFF a current of 50 mA when the MPs reach the edge of one conductor and switching ON the consequent conductor. Four GMR spin valve microsensors fabricated underneath the MCs are situated as follows: two underneath the first MCs and two underneath the last MCs.

Sensing the stray fields of the MPs in both channels provides information about their presence or absence on top of the first and last MCs. For the detection, we utilized the double frequency modulation technique, [55] substituting the lock-in amplifier with a spectral analysis algorithm described in reference [56]. Since we proved the successful performance of our microfluidic sensing system using uncoated MPs, we proceeded to determine the magnetophoretic behav-

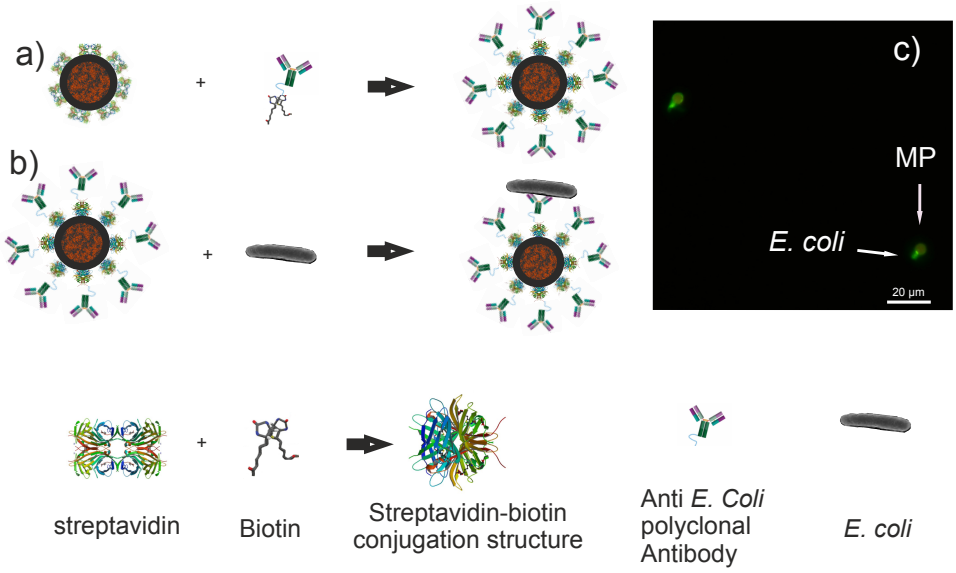

Figure 5.2: Conjugation processes for the capturing of *E. coli* and biotinylated antibodies on MPs: (a) streptavidin coated MPs conjugated with biotinylated anti-*E. coli* polyclonal antibodies. (b) Consequently, the antibody loaded magnetic particles are conjugated with *E. coli* (whole organism). (c) Fluorescence microscopy images of BLMPs, (d) graphic illustration of the stereochemical structure of streptavidin and biotin with the resulting conjugate, and e) graphic illustration of an anti-*E. coli* polyclonal antibody and a whole *E. coli* organism.

ior for the chemically modified ones.

In order to study the effects on MPs coated with bioanalytes (e.g. *E. coli* and antibodies) but also characterize the interaction forces between the sample and the surface, IgG rabbit polyclonal antibodies were conjugated to the MPs. These antibodies are specific for the O and K antigenic serotypes of *E. coli* gram negative bacteria and they are biotinylated through the amine-reactive cross-linker chemistry, [57] (Figure 5.2 (a)). Subsequently, a part of the ALMPs was conjugated with *E. coli* K12 wild type gram negative bacteria. The common K12 strain was chosen for its equivalence to the pathogenic *E. coli* expressing the enterohemorrhagic serotype O157:H7, a profound food contaminant [58] (Figure 5.2 (b)).

As stated in the introduction, biological entities on the surface of the particles exhibit adhesion with common materials used in MEMS technology. Preliminary experiments showed complete adhesion of the streptavidin coated particles on the biosensor's SiO_2 surface. For that reason, a surface modification was developed, based on the layer-by-layer (LbL) electrostatic self-assembly (ESA) technique. [59] Two biocompatible polyelectrolytes, polyethyleneimine (PEI) and sodium alginate (SAl), were sequentially immobilized on the biosensor's surface forming a bilayer. First, the SiO_2 passivation layer of the biosensor was treated with oxygen plasma so as to enhance its negative charge; then PEI, a polycation, was attracted on the surface, and lastly, SAl, a polyanion, was electrostatically coupled with the PEI. With SAl having the properties of absorbing water molecules, the antifouling property of the final surface are greatly enhanced, while the overall thickness, as AFM measurements suggest, increases slightly (Figure A.1).

5.4.1 Measurement process

For the measurement process, both the test and the reference samples are injected into the channels using pipets. Then, the excess liquid is removed from the inlets with fine swabs. This asserts that the level of liquid in the inlet and the outlet is equal and there is no gravity induced flow in the channel. With the injection of the samples, the MA is covered with scattered MPs and LMPs. In order to avoid false readings, the area has to be free of MPs. Therefore, we sequentially

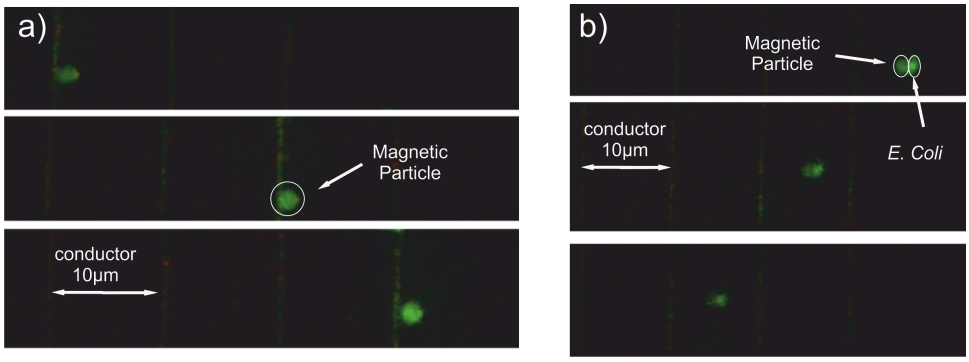

Figure 5.3: Video stills from the manipulation of (a) *E. coli* loaded magnetic particles (BLMPs) and (b) antibody loaded magnetic particles (ALMPs). The video was acquired in a combined dark field and fluorescence microscopy arrangement so that both the BLMP and the MCs (utilized in the analysis as a reference for the velocity measurement) are illuminated. Both BLMPs and ALMPs are labeled with secondary antibodies conjugated with a fluorophore for visualization purposes.

actuate the MCs from the last to the first with a time interval that allows even the slowest particle to move from one MC to the next. All the current switching sequences are operated by a programmable microcontroller. Subsequently, if the first spin valves in both channels detect one or more MPs, we again sequentially actuate the MCs this time in the opposite direction, from first to last (Figure 5.3). The time each MC is ON is determined by the time the MPs in the reference channel (unloaded MPs) were required to move from one conductor to the next and has to be defined experimentally before the sensing procedure, as a calibration step. This certifies that the sensor underneath the last MC in the reference channel will give a signal change at the end of the sequential actuation. Simultaneously, in the measurement channel (in the presence of the analyte at the MPs' surface), the slower LMPs will fall behind or arrive with a delay at the vicinity of the sensor. That way, we deduct the test results.

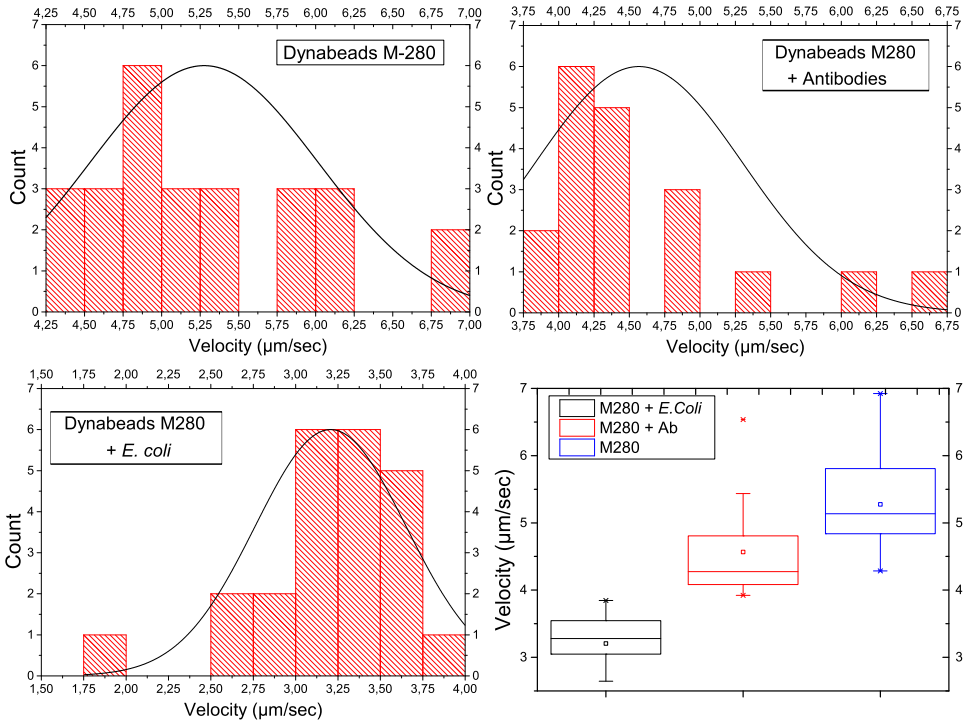

Figure 5.4: Graph showing the mean velocity of magnetic particles: plain Dynabeads® M-280, antibody loaded magnetic particles, and bacteria loaded magnetic particles. Candlestick graph of previous experimentally obtained data, suggesting a distinct change in velocity between the different MPs manipulated under the same conditions.

	Magnetic Particles	Statistical Mean	Standard Deviation	Min.	Median	Max.
Mean Velocity (µm/sec)	MPs	5.2757	0.7408	4.2857	5.1355	6.9230
	ALMPs	4.5676	0.7374	3.9216	4.2735	6.5360
	BLMPs	3.2064	0.4459	1.7668	3.2787	3.8462

Table 5.1: The values of the statistical mean, the standard deviation as well as the minimum, the median, and the maximum value in µm/sec for Plain Dynabeads® M-280 (MPs), Antibody Loaded Magnetic Particles (ALMPs) and *E. coli* (Bacteria) Loaded Magnetic Particles (BLMPs).

5.5 Results and discussion

In order to prove the concept of the microfluidic biosensor, we had to show that the velocity of the MPs in suspension throughout the (on chip) magnetophoretic procedure was lower for ALMPs with respect to plain MPs (in the reference channel) and even lower when the antibody had captured an *E. coli* bacterium (e.g. BLMPs).

To do so, the magnetophoretic procedure was filmed using a 50x microscope lens. The videos were then analyzed, and the velocities were deducted. The results are shown in Figure 5.4. In order to cross-check the results and to test the biosensor's efficiency, the samples were again injected into the channels; this time the microcontroller was programmed to maintain each conductor ON for a period of time equal to the mean velocity value for each sample type, as the previous experiments suggested (values are presented in the table shown in Figure 5.4).

The results were verified with the GMR sensors that could register a measurement at the end of the magnetophoretic procedure (Figure 5.5). Such a registered signal by the GMR sensor means that at least one MP could travel with the mean velocity from one conductor to the other provided that they were carrying current (exerting magnetic field gradient) for the time interval corresponding to the ve-

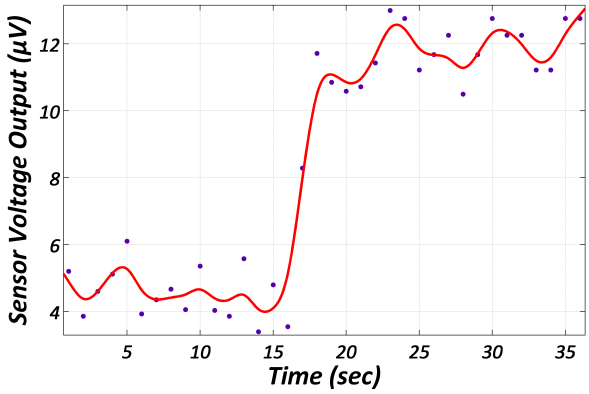

Figure 5.5: Graph acquired during the detection of a single MAP by the GMR sensor showing the sensor's voltage output over time. The red line is a second order polynomial fitting to the raw data.

locity measured for each sample type. The reason for the decrease in velocity of the BLMPs has been sufficiently analyzed in reference [24] and is based on the overall volumetric increase while the magnetic volume remains constant; the same does not apply for the ALMPs.

The ratio of gyration for the IgG antibodies conjugated with biotin molecules is of the order of a few nanometers. That can cause, considering the size of the MPs, an insignificant velocity decrease. Since it is not the Stokes' drag force that is significantly altered and the magnetic force remains constant, we conclude that the causes of this decrease in the velocity are the friction and the adhesion surface forces. As equation 5.4 suggests, the friction and the adhesion are interconnected; thus, it is justified to assume that the change in velocity for the ALMPs with respect to plain, streptavidin coated MPs is due to enhanced friction forces. In order to experimentally prove this assumption, we conducted adhesion and friction force measurements utilizing an AFM device with a functionalized tip. As a first approach, we directly linked paramagnetic particles with different functionalities to the AFM tip apex. However, none of the used approaches, neither the linkage via biotin nor via antibody linkage, showed the expected performance. In both cases, we observed a visible lateral movement of the particle on the apex of the tip by scanning on a glass surface, which we imaged by the combined atomic force and fluorescence microscopy (Figure A.2). Therefore, we changed the approach and directly chemically functionalized the AFM tip (Figure 5.6 (a)). In particular, we started by using a cleaned Si_3N_4 tip, followed by further functionalization processes as described in section 5.3 and measured the interaction between various functionalized tips and different surfaces.

Figure 5.6 (b) and 5.6 (c) summarize the adhesion and friction force study. Three different tip surfaces were tested on two different chip surfaces: a SiO_2 surface (dark grey) and the PEI/SAl modified surface (light grey). It is apparent that the unmodified chip's surface could not be used to manipulate streptavidin coated (plain) MPs or ALMPs as the adhesion forces are an order of magnitude greater than the magnetophoretic force exerted on the MPs by the conductors. The study also suggests that the adhesion force is greater for the antibody coated tip than the streptavidin coated one. This implies, due to the first term of the friction force equation in section 5.2 (Equation

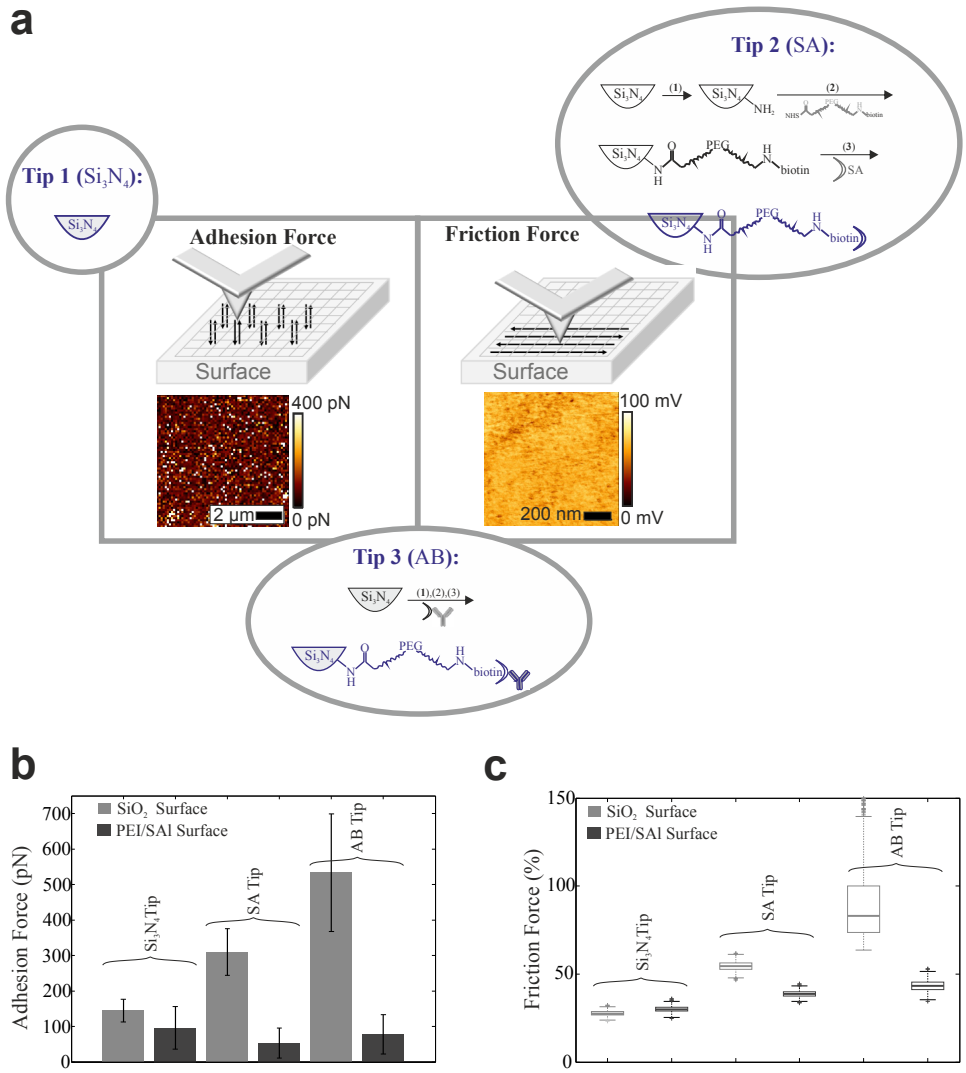

Figure 5.6: (a) Chemical methods for conjugating a streptavidin (SA) monolayer and subsequently antibodies (AB) on an atomic force microscope tip, in order to simulate the motion of the MPs on the modified chip's surface and measure adhesion and friction forces. The methods for acquiring the measurements for the different forces and the raw data in the form of images are displayed. (b) Adhesion force measurements with a silicon nitride tip (tip 1), a streptavidin coated tip (tip 2) and an antibody coated tip (tip 3) on a SiO_2 and a polyethyleneimine/sodium alginate modified surface. The figure clearly demonstrates the stiction of the MPs on the unmodified surface. (c) Friction force measurements using the same 3 tips and surfaces. The demonstrated difference in friction between the streptavidin coated tip and the antibody coated one translates into velocity difference for the respective MPs during magnetophoresis.

5.4), that the friction force could be greater for the antibody coated tip as well. Indeed, friction force measurements showed that the friction force exerted on a moving tip (with a velocity of 5 µm/sec) on the modified PEI/SAl surface was significantly greater for the antibody coated tip than the streptavidin coated one.

The results lead to the assumption that frictional interactions between biomolecules and surfaces could be utilized to differentiate biomolecules with a distinct spatial structure, provided that this translates into different friction forces. Of course, the same principle could apply for differentiating the same protein but with different or incorrect folding.

5.6 Conclusions

The AFM friction force measurements proved the original assumption. The observed decrease in the mean velocity during the magnetophoretic manipulation of ALMPs with respect to plain, streptavidin coated MPs is due to the enhanced friction of the ALMPs. The actual nature of the enhanced friction is unclear but most probably linked to the 3D protein structure of the IgGs and their spatial orientation, protruding out of the MP surface.

Thus, we demonstrated the potential efficiency of the developed microfluidic sensor in detecting *E. coli*, as a whole organism, by using the change in velocity measured indirectly with integrated GMR sensors, due to the enhanced Stokes' drag force exerted on the BLMPs because of their volumetric increase with respect to plain MPs. We also demonstrated the possibility of using the same biosensor for the detection of biotinylated antibodies. Again, a decrease in velocity is utilized for the detection scheme. However this time, the decrease is due to the enhanced friction exerted on the ALMPs.

Other members of the family Enterobacteriaceae (e.g. Salmonella and Klebsiella) are currently being measured with the presented microfluidic biosensor in order to prove that it can be used as a general pathogen sensor. In parallel, experiments are conducted with other molecules in order to demonstrate the possibility of using the same biosensor for the detection of smaller entities other than biotinylated antibodies, for example proteins and even non-organic substances as

polymers.

Acknowledgements

The research at the Vienna University of Technology was supported by the Austrian Science Fund (FWF) with Project No. P 24372-N19. INESC-MN acknowledges FCT funding through the IN Associated Laboratory (Pest-OE/CTM/LA0024/ 2011) and Project EXCL/CTM-NAN/0441/2012.

Bibliography

[1] W.-C. W. Tian and E. Finehout, "Microfluidic Diagnostic Systems for the Rapid Detection and Quantification of Pathogens," in *Microfluidics for Biological Applications*, pp. 271–322, Springer, 2008.

[2] P. Yager, G. J. Domingo, and J. Gerdes, "Point-of-care diagnostics for global health.," *Annual review of biomedical engineering*, vol. 10, pp. 107–144, 2008.

[3] A. Schlichtiger, P. Luppa, D. Neumeier, and M. Thaler, "Biosensor approaches for the detection of autoantibodies in human serum," *Bioanalytical Reviews*, vol. 4, no. 2-4, pp. 75–86, 2012.

[4] D. M. Goldenberg, "Monoclonal antibodies in cancer detection and therapy," *The American Journal of Medicine*, vol. 94, pp. 297–312, mar 1993.

[5] J. Moldenhauer, "Rapid microbiological methods and the PAT initiative," *Biopharm international*, vol. SEP, pp. 11–20, 2005.

[6] J. P. Jiang, "Instantaneous microbial detection using optical spectroscopy," *Encyclopedia of rapid microbiological methods*, vol. 3, pp. 121–141, 2005.

[7] O. Lazcka, F. J. D. Campo, and F. X. Muñoz, "Pathogen detection: A perspective of traditional methods and biosensors," *Biosensors and Bioelectronics*, vol. 22, pp. 1205–1217, feb 2007.

[8] D. Nichols, "Cultivation gives context to the microbial ecologist," *FEMS microbiology ecology*, vol. 60, no. 3, pp. 351–357, 2007.

[9] R. M. Lequin, "Enzyme immunoassay (EIA)/enzyme-linked immunosorbent assay (ELISA)," *Clinical chemistry*, vol. 51, no. 12, pp. 2415–2418, 2005.

[10] B. Vuylsteke, "Current status of syndromic management of sexually transmitted infections in developing countries," *Sexually Transmitted Infections*, vol. 80, no. 5, pp. 333–334, 2004.

[11] M. L. Y. Sin, K. E. Mach, P. K. Wong, and J. C. Liao, "Advances and challenges in biosensor-based diagnosis of infectious diseases," *Expert review of molecular diagnostics*, vol. 14, pp. 225–244, mar 2014.

[12] J. Loureiro, R. Ferreira, S. Cardoso, P. P. Freitas, J. Germano, C. Fermon, G. Arrias, M. Pannetier-Lecoeur, F. Rivadulla, and J. Rivas, "Toward a magnetoresistive chip cytometer: Integrated detection of magnetic beads flowing at cm/s velocities in microfluidic channels," *Applied Physics Letters*, vol. 95, no. 3, p. 034104, 2009.

[13] A. K. Balasubramanian, A. Beskok, and S. D. Pillai, "In situ analysis of bacterial capture in a microfluidic channel," *Journal of Micromechanics and Microengineering*, vol. 17, pp. 1467–1478, aug 2007.

[14] J. Chen, D. Chen, Y. Xie, T. Yuan, and X. Chen, "Progress of Microfluidics for Biology and Medicine," *NANO-MICRO LETTERS*, vol. 5, no. March, pp. 66–80, 2013.

[15] K.-S. Yun, D. Lee, H.-S. Kim, and E. Yoon, "A microfluidic chip for measurement of biomolecules using a microbead-based quantum dot fluorescence assay," *Measurement Science and Technology*, vol. 17, pp. 3178–3183, dec 2006.

[16] L. Y. Yeo, H.-C. Chang, P. P. Y. Chan, and J. R. Friend, "Microfluidic devices for bioapplications.," *Small (Weinheim an der Bergstrasse, Germany)*, vol. 7, pp. 12–48, jan 2011.

[17] J. Mairhofer, K. Roppert, and P. Ertl, "Microfluidic systems for pathogen sensing: A review," *Sensors (Switzerland)*, vol. 9, no. 6, pp. 4804–4823, 2009.

[18] K. S. Kim and J.-K. Park, "Magnetic force-based multiplexed immunoassay using superparamagnetic nanoparticles in microfluidic channel.," *Lab on a chip*, vol. 5, pp. 657–64, jun 2005.

[19] P. Kinnunen, I. Sinn, B. H. McNaughton, D. W. Newton, M. a. Burns, and R. Kopelman, "Monitoring the growth and drug susceptibility of

individual bacteria using asynchronous magnetic bead rotation sensors.," *Biosensors & bioelectronics*, vol. 26, pp. 2751–5, jan 2011.

[20] M. Mujika, S. Arana, E. Castaño, M. Tijero, R. Vilares, J. M. Ruano-López, a. Cruz, L. Sainz, and J. Berganza, "Magnetoresistive immunosensor for the detection of Escherichia coli O157:H7 including a microfluidic network.," *Biosensors & bioelectronics*, vol. 24, pp. 1253–8, jan 2009.

[21] O. Laczka, J.-M. Maesa, N. Godino, J. del Campo, M. Fougt-Hansen, J. P. Kutter, D. Snakenborg, F.-X. Muñoz-Pascual, and E. Baldrich, "Improved bacteria detection by coupling magneto-immunocapture and amperometry at flow-channel microband electrodes.," *Biosensors & bioelectronics*, vol. 26, pp. 3633–40, apr 2011.

[22] J. B. Haun, T.-J. Yoon, H. Lee, and R. Weissleder, "Magnetic nanoparticle biosensors.," *Wiley Interdisciplinary Reviews: Nanomedicine and Nanobiotechnology*, vol. 2, pp. 291–304, may 2010.

[23] A. Sandhu, "Biosensing: New probes offer much faster results," *Nature Nanotechnology*, vol. 2, pp. 746–748, dec 2007.

[24] G. Kokkinis, F. Keplinger, and I. Giouroudi, "On-chip microfluidic biosensor using superparamagnetic microparticles," *Biomicrofluidics*, vol. 7, p. 054117, jan 2013.

[25] M. Y. Okiishi, B. Munson, and D. Young, *Fundamentals of Fluid Mechanics*. John Wiley & Sons, Inc, 2006.

[26] G. R. Bartlett, "Phosphorus assay in column chromatography.," *Journal of Biological Chemistry*, vol. 234, pp. 466–468, 1959.

[27] J. W. Jorgenson and K. D. Lukacs, "Capillary zone electrophoresis," *Science (Washington, DC);(United States)*, vol. 222, no. 4621, 1983.

[28] B. Bhushan, "Micro/nanotribology and its applications to magnetic storage devices and MEMS," *Tribology International*, vol. 28, pp. 85–96, mar 1995.

[29] M. Suwa and H. Watarai, "Magnetoanalysis of micro/nanoparticles: a review.," *Analytica chimica acta*, vol. 690, pp. 137–47, apr 2011.

[30] R. Ganguly and I. K. Puri, "Microfluidic transport in magnetic MEMS and bioMEMS," *Wiley Interdisciplinary Reviews: Nanomedicine and Nanobiotechnology*, vol. 2, no. 4, pp. 382–399, 2010.

[31] N. Pamme, "Magnetism and microfluidics.," *Lab on a chip*, vol. 6, pp. 24–38, jan 2006.

[32] T. Quang-Hung, K. Dong-Young, R. B. Parvatheeswara, K. Cheolgi, T. Hung, D. Kim, B. Rao, and C. Kim, "Novel Planar Hall Sensor for Biomedical Diagnosing Lab-on-a-Chip," in *State of the Art in Biosensors - General Aspects*, pp. 197–239, Toonika Rinken, 2013.

[33] K. N. Tu, "Recent advances on electromigration in very-large-scale-integration of interconnects," *Journal of Applied Physics*, vol. 94, no. 9, p. 5451, 2003.

[34] S. S. Shevkoplyas, A. C. Siegel, R. M. Westervelt, M. G. Prentiss, and G. M. Whitesides, "The force acting on a superparamagnetic bead due to an applied magnetic field.," *Lab on a chip*, vol. 7, pp. 1294–302, oct 2007.

[35] E. Loth, "Drag of non-spherical solid particles of regular and irregular shape," *Powder Technology*, vol. 182, no. 3, pp. 342–353, 2008.

[36] E. Meyer, *Nanoscience: friction and rheology on the nanometer scale*. World Scientific, 1998.

[37] B. Bhushan, J. N. Israelachvili, and U. Landman, "Nanotribology: friction, wear and lubrication at the atomic scale," *Nature*, vol. 374, no. 6523, pp. 607–616, 1995.

[38] R. W. Carpick and M. Salmeron, "Scratching the surface: fundamental investigations of tribology with atomic force microscopy," *Chemical Reviews*, vol. 97, no. 4, pp. 1163–1194, 1997.

[39] J. Van Alsten and S. Granick, "Molecular tribometry of ultrathin liquid films," *Physical review letters*, vol. 61, no. 22, p. 2570, 1988.

[40] S. Granick, "Motions and Relaxations of Confined Liquids," *Science*, vol. 253, pp. 1374–1379, sep 1991.

[41] M. L. Gee, P. M. McGuiggan, J. N. Israelachvili, and A. M. Homola, "Liquid to solidlike transitions of molecularly thin films under shear," *The Journal of Chemical Physics*, vol. 93, no. 3, pp. 1895–1906, 1990.

[42] M. Ruths and J. N. Israelachvili, "Nanotribology and Nanomechanics II," ch. Surface Fo, Berlin, Heidelberg: Springer Berlin Heidelberg, 2011.

[43] E. J. W. Verwey and J. T. G. Overbeek, *Theory of the stability of lyophobic colloids*. Courier Corporation, 1999.

[44] B. V. Derjaguin, "Theory of the stability of strongly charged lyophobic sols and the adhesion of strongly charged particles in solutions of electrolytes," *Acta Physicochim. USSR*, vol. 14, pp. 633–662, 1941.

[45] J. J. N. Israelachvili, *Intermolecular and Surface forces*. Academic press, 2011.

[46] V. Gehanno, P. P. Freitas, A. Veloso, J. Ferreira, B. Almeida, J. B. Sousa, A. Kling, J. C. Soares, and M. F. Da Silva, "Ion Beam Deposition of Mn-Ir Spin Valves," *IEEE TRANSACTIONS ON MAGNETICS*, vol. 35, no. 5, 1999.

[47] A. Ebner, P. Hinterdorfer, and H. J. Gruber, "Comparison of different aminofunctionalization strategies for attachment of single antibodies to AFM cantilevers," *Ultramicroscopy*, vol. 107, pp. 922–927, oct 2007.

[48] L. Wildling, B. Unterauer, R. Zhu, A. Rupprecht, T. Haselgrübler, C. Rankl, A. Ebner, D. Vater, P. Pollheimer, E. E. Pohl, P. Hinterdorfer, and H. J. Gruber, "Linking of Sensor Molecules with Amino Groups to Amino-Functionalized AFM Tips," *Bioconjugate Chemistry*, vol. 22, pp. 1239–1248, jun 2011.

[49] R. Levy and M. Maaloum, "Measuring the spring constant of atomic force microscope cantilevers: thermal fluctuations and other methods," *Nanotechnology*, vol. 13, no. 1, p. 33, 2002.

[50] M.-S. Kim, J.-H. Choi, J.-H. Kim, and Y.-K. Park, "Accurate determination of spring constant of atomic force microscope cantilevers and comparison with other methods," *Measurement*, vol. 43, no. 4, pp. 520–526, 2010.

[51] R. W. Stark, T. Drobek, and W. M. Heckl, "Thermomechanical noise of a free v-shaped cantilever for atomic-force microscopy," *Ultramicroscopy*, vol. 86, no. 1, pp. 207–215, 2001.

[52] J. L. Hutter and J. Bechhoefer, "Calibration of atomic force microscope tips," *Review of Scientific Instruments*, vol. 64, no. 7, pp. 1868–1873, 1993.

[53] T. Huesgen, G. Lenk, B. Albrecht, P. Vulto, T. Lemke, and P. Woias, "Optimization and characterization of wafer-level adhesive bonding with patterned dry-film photoresist for 3D MEMS integration," *Sensors and Actuators A: Physical*, vol. 162, pp. 137–144, jul 2010.

[54] D. Puchberger-Enengl, S. Podszun, H. Heinz, C. Hermann, P. Vulto, and G. A. Urban, "Microfluidic concentration of bacteria by on-chip electrophoresis," *Biomicrofluidics*, vol. 5, no. 4, p. 44111, 2011.

[55] F. Li and J. Kosel, "A Magnetic Biosensor System for Detection of E. coli," *Magnetics, IEEE Transactions on*, vol. 49, pp. 3492–3495, jul 2013.

[56] G. Kokkinis, M. Jamalieh, F. Cardoso, S. Cardoso, F. Keplinger, and I. Giouroudi, "Magnetic-based biomolecule detection using giant magnetoresistance sensors," *Journal of Applied Physics*, vol. 117, p. 17B731, may 2015.

[57] G. G. T. Hermanson, *Bioconjugate techniques*. Academic press, 1996.

[58] P. M. Griffin and R. V. Tauxe, "The epidemiology of infections caused by Escherichia coli O157: H7, other enterohemorrhagic E. coli, and the associated hemolytic uremic syndrome," *Epidemiologic reviews*, vol. 13, no. 1, pp. 60–98, 1991.

[59] Q. Zhao, J. Qian, Q. An, and B. Du, "Speedy fabrication of free-standing layer-by-layer multilayer films by using polyelectrolyte complex particles as building blocks," *Journal of Materials Chemistry*, vol. 19, no. 44, p. 8448, 2009.

Chapter 6
Publication E

A novel approach for detection and quantification of magnetic nanomarkers using a spin valve GMR integrated microfluidic sensor

Authored by J. Devkota[1], G. Kokkinis[1], T. Berris, M. Jamalieh, S. Cardoso, F. Cardoso, H. Srikanth, M. H. Phan and I. Giouroudi.
Published in *RSC Advances,* **vol. 6**, pp 31135 - 31135, (2016).

Abstract

We demonstrate the application of a spin valve giant magnetoresistance (GMR) integrated microfluidic sensor for the detection and quantification of superparamagnetic nanomarkers. A microfluidic channel containing the magnetic fluid, micro-conductors (MCs) for collection of magnetic markers and a spin valve GMR sensor for detecting the presence of magnetic stray field were integrated into a single chip and employed for detection of various concentrations of Nanomag-D beads of 250 nm diameter. The results show that the sensor is capable of detecting concentrations as low as 500 pg/µl of Nanomag-D beads and quantifying them in a linear scale over a wide particle concentration range (1-500 ng/µl). Our study provides a novel platform towards the development of a portable lab-on-a-chip sensor.

[1] These authors contributed equally to this work

6.1 Introduction

Epidemic and public health care around the globe has an increasing demand of a cost-effective, portable, and userfriendly diagnostic system for an accurate, reliable, and rapid analysis of biological entities to control infectious diseases and pathogens. [1–3] While optical and electrochemical techniques have long been used for medical diagnosis, they are sometimes complex for integration into a chip, require a relatively large amount of reagents, and may possess autofluorescence, absorption, scattering, and possible unwanted reactions. [1–6] A combination of magnetic sensors with magnetic nanoparticles has provided a promising alternative that can fulfill the increasing requirements of such a portable robust device. [5–13] These biosensors, in general, utilize the stray fields [8,9] or relaxation time [5,14] of functionalized magnetic nanoparticles (also known as magnetic markers) to detect and quantify the bioanalytes tagged to them. Giant magnetoresistance (GMR) biosensors, [8,9] based on the former principle, have emerged as excellent biosensing techniques for room temperature detection and quantification of biological entities due to their high sensitivity, less complex instrumentation, compact size, and integration flexibility. Current efforts are to integrate these sensors within microfluidic devices to develop a cost-effective, sensitive, and portable device for rapid diagnosis of diseases. [2,15]

GMR, which refers to a large change in the resistivity of a layered ferromagnetic material subject to an applied DC magnetic field, [16,17] is being widely exploited in hard disk drives. However, its applicability to biosensing was not much noticed until Baselt et al. demonstrated, in 1998, the capacity of using an GMR-based sensor for detection of magnetic beads. [9] Since then a variety of GMR-based platforms have been developed for sensitive and low-cost biodetection. [5,8,9,12,18–20] In recent years, magnetic tunnelling junction [21,22] and spin-valve GMR [8] based sensors have gained growing interest over regular GMR and anisotropic MR sensors for their higher detection sensitivity. [6] Regardless of the sensor type, the detection of magnetic biomarkers, either single bead or their mass coverage, using a GMR sensor significantly depends upon the measurement conditions. For instance, delivery of a test sample to the sensor by drop casting or open flow injection techniques requires

a large amount of sample volume, takes a longer time for the sample to be settled on the sensor surface, and offers no control over the physical motion of the beads that minimizes the chances of the beads reaching to the sensor surface. These effects degrade the biosensors' performance, thus providing limited information about the bioagents tagged to the beads. In these circumstances, the sensors are also unsafe when working with biothreats, limiting their practical use for epidemic and public health purposes.

On the other hand, microfluidic systems have been developed as a popular pathway in biology and medicine for reliable experiments in a controlled and safe environment. [20,23] This technology has been being widely exploited in a wide range of domains, such as biosensing, cell culturing, miniaturization, and bio-chemical processes. [20,23] For example, Li *et al*. integrated tunneling magnetoresistive sensors with a microfluidic system containing circular bead concentrators to detect *E. coli* tagged to Dynabeads® of 2.8 µm diameter. [19,24] Recently, Kokkinis *et al*. have reported upon the detection of pathogens using the volumetric change of a single micro-bead in a microfluidic biosensing system composed of spin-valve GMR sensors and a set of parallel microconductors (MCs). [12] These studies have revealed new approaches to integrating GMR-based sensors with microfluidic systems for advanced biosensing. While conventional biosensors require the application of an external magnetic field, these biosensing devices utilize a current flowing through the MC's, thus making the diagnostic system more portable and compatible to modern electronics. While the previous studies were focused mainly on detection of micronsized biomarkers, labelling of biological identities such as DNA, viruses and cells require the use of magnetic nanobeads or magnetic nanoparticles and thus detection of these nanosized biomarkers became increasingly important. These have motivated us to develop a novel spin-valve GMR-integrated microuidic system for such purposes.

In this paper, we report upon the possibility of using this newly developed microfluidic platform as a biosensor for sensitive detection and quantification of Nanomag-D beads of 250 nm in diameter. The nanobeads used, with the protruding amino groups (-NH_2), can be functionalized with the EDC - NHS chemistry [12] and thus can be used to tag biological entities (e.g. viruses, microbial pathogens

and cells). For that reason, our system can be ideal for use in clinical diagnosis that requires a rapid and reliable analysis of bioagents.

6.2 Materials and methods

6.2.1 GMR sensors and microfluidic channels

Four spin valve GMR sensors with dimensions of 6 µm × 2 µm were fabricated on a Si substrate by sputtering Al_2O_3 100 nm/ Ta 3 nm/ NiFe 3.6 nm/ MnIr 8.5 nm/ CoFe 2.3 nm/ Ru 0.8 nm/ CoFe 2.3 nm/ Cu 3 nm/ CoFe 3 nm/ NiFe 3.6 nm/ Ta 5 nm and the patterns were defined by an ion milling process. The 300 nm thick GMR electrodes were sputtered to provide an in-plane current flow to the sensing structures. A 300 nm silicon nitride passivation layer was then deposited. On top of the passivated sensors, nine-gold conducting MCs were fabricated using photolithography and sputtering techniques. Each MC had a width of 10 µm and a thickness of 500 nm, and was separated by 10 µm from the nearest neighboring MC. This way, two GMR sensors lied below the first MC and two GMR sensors lied below the last MC. Finally, two PDMS microfluidic channels, a reference and a measurement channel respectively, of 50 µm height, 500 µm width, and 50 mm length were fabricated using a negative photoresist mold patterned by a standard photolithography technique and upon which the PDMS was casted, cured, peeled off and placed on top of the MCs. The MCs were used to concentrate the Nanomag-D beads from the inlet to the outlet of the channels thus decreasing the lower limit of the sensor's range. Figure 6.1 (a) displays a schematic of the developed GMR microfluidic sensor, with the details of its cross section and the spin-valve GMR structure shown in Figure 6.1 (b). At the inlets and outlets of the reference and measurement channels, fluidic connectors were integrated to inject the magnetic fluid and pump it out after each measurement. Details of the fabrication of spin-valve GMR sensors, MCs, and microfluidic channels have been reported elsewhere. [12, 18]

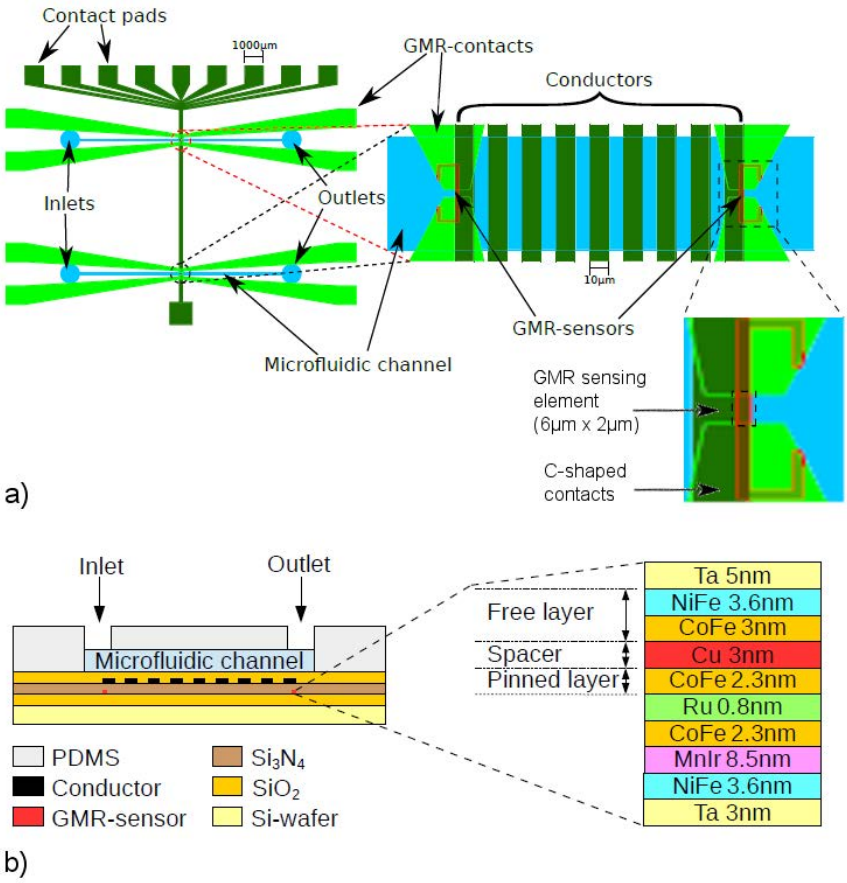

Figure 6.1: (a) Schematic of the developed GMR-microfluidic sensor; one microfluidic channel is used as a reference channel and the second one as the measurement channel; (b) the details of a spin-valve GMR element.

6.2.2 Magnetic nanomarkers

In this study, we used commercially available Nanomag-D nanobeads (diameter $\approx 250\,\text{nm}$) composed of iron oxide nanoparticles encapsulated into a dextran matrix with protruding amino groups (-NH_2). Such nanoparticles can also be purchased with a functionalization layer (e.g. antibodies) in order to tag biological entities (e.g. viruses or microbial pathogens). These nanobeads with an original concentration of $\approx 10\,\text{mg/ml}$ were purchased from Micromod Partikeltechnologie GmbH, Germany and were diluted to various concentrations

in water. A room-temperature magnetic hysteresis (M - H) loop of the nanobeads and their TEM image are shown in Figure 6.2 and its inset, respectively. It can be seen in the figure that the M - H loop shows no hysteresis ($H_c = 0$) and no remanence ($M_r \approx 0$), indicating the superparamagnetic characteristic of the nanobeads used. The superparamagnetic nature has been further confirmed by the best fit of the M - H data to the Langevin function. We recall that the superparamagnetic property of magnetic markers is desirable for a variety of biomedical applications. [25, 26]

6.2.3 System integration and implementation

In our microfluidic biosensing system, the spin valve GMR sensors and MCs were integrated into a chip and they were covered by the PDMS channels aligned perpendicular to the MCs (Figure 6.1 (a)). This configuration allows the magnetic fluid to flow across the MCs. In this study, the desired fluid concentration of Nanomag-D beads was injected to the measurement channel through the inlet and pumped through the outlet for a full coverage of the channel volume. An optical microscope (Nikon- Eclipse LV150) was set up

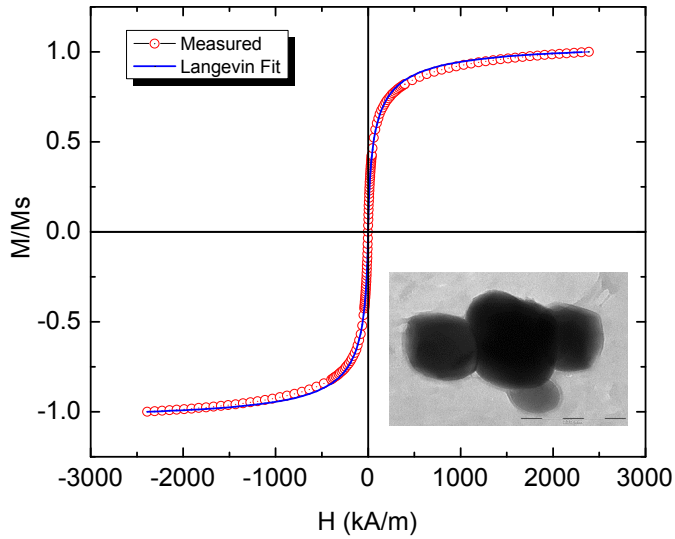

Figure 6.2: Room temperature magnetic hysteresis loop of Nanomag-D beads. Inset shows a typical TEM image of the particles.

on top of the channel to observe the physical motion of the beads in real time. The MCs were connected to a DC power source of 50 mA (Agilent E3649A dual output DC power supply) that allowed the beads to be concentrated at the desired MC. In addition, MC #1 was also connected to an AC function generator providing a sinusoidal signal of I_M . 10 mA, $f_M = 1.234$ kHz (Agilent model 33220A) that was used as a source for an externally applied magnetic field to magnetize the nanobeads. The sensor itself was connected to an AC source of $I_S = 1\,mA$ operating at a frequency $f_S = 0.234\,kHz$ (Agilent model 33220A) and the voltage across it was measured by a LabVIEW controlled SR830 Lock-in Amplifier at a locked frequency of flock . $f_M + f_S = 1.468\,kHz$ and a reference voltage of 1 V supplied by an Agilent function generator (model 33220A). All three function generators where interconnected and operated at infinite burst mode so as to be in phase. The modulation - demodulation technique using a lock-in amplifier has been described in detail elsewhere. [27] As the sensor's transfer curve suggests (Figure 6.3) the working point is near the lowest saturation point. This way, even though the sinusoidal voltage output of the sensor decreases, a span of 50 Oe is offered until the sensor is saturated on the upper part of the curve. This way we make sure the upper laying MC's magnetic field, which

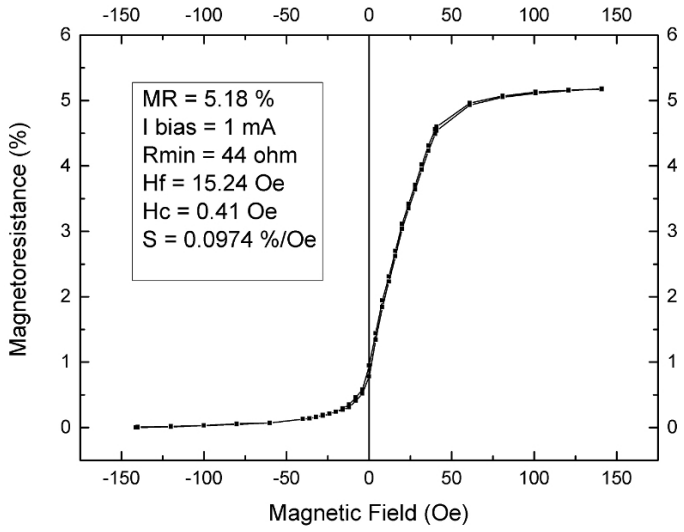

Figure 6.3: Transfer curve of the integrated GMR sensor.

is of the order of a few Oe, does not saturate the sensor. Finally, all sensors on the chip were of similar characteristics within an insignificant range.

The Nanomag-D beads, suspended in water, were injected into the channel by placing a droplet in the inlet and applying a subpressure in the outlet. Once injected with no additional flow applied (static fluid), the beads were first attracted at MC #8 by a DC magnetic field and then transferred towards the sensor by sequentially applying a current through the consecutive MCs.

The voltage V_s measured across the GMR sensor was recorded as a function of time and the relative change in voltage was considered as the sensor's figure-of-merit. The relative change in the sensor voltage due to the presence of themagnetic nanobeads on the first MC was defined as the voltage ratio; calculated as

$$\frac{\Delta V}{V} = \frac{\mid V_0 - V_{sat} \mid}{V_{sat}} \tag{6.1}$$

where V_0 is the voltage V_s across the GMR sensor at $t = 0$, i.e. the beads begin to move towards the first MC from their original position and V_{sat} is the saturation value of V_s, which is ideally achieved when all the magnetic markers are collected at the vicinity of the sensor i.e. on the surface of the MC #1.

6.3 Results and discussion

Figure 6.4 (a) and 6.4 (b) show the optical microscopy images of Nanomag- D beads (300 ng/ml) concentrated on MC #2 and MC #1, respectively. The nanobeads were spread throughout the PDMS measurement channel when the magnetic fluid was injected into it. To achieve the highest effect of the nanobeads on the GMR sensor's voltage V_s, all of the beads must be collected into a close proximity to the sensor. To achieve that the sample was initially left for two minutes to sediment. With the channels height being 50 µm and the conductors being able to exert a magnetic force on the beads from a distance of 30 µm we can confirm that the entire volume of the channel was swept clean from beads at the area above the conductors. Initially the nanobeads were manipulated and collected on the

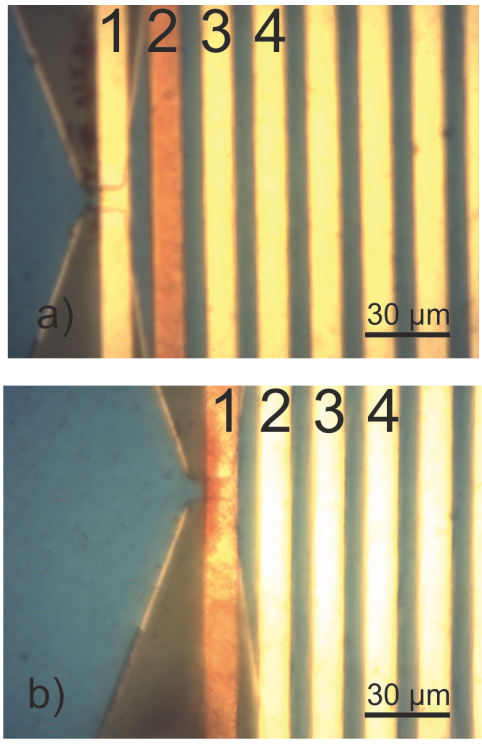

Figure 6.4: Optical microscopy images of Nanomag-D beads (300 ng/µl) on the micro-conductors: (a) MC #2 and (b) MC #1.

surface of MC #8 by supplying a DC current of $I_M = 50\,mA$. The DC current applied to the MC induced a magnetic field gradient and hence the magnetic force that pulled the nanobeads onto its surface. Once the nanobeads were collected on MC #8, they were then transferred to MC #7. This process continued until the nanobeads reached MC #3 or #2, followed by the measurement of V_s across the sensor. The transfer of the nanobeads to each consecutive MC was followed by the V_s measurement which remained unaffected until the beads reached MC #1. Then, MC #1 was supplied with an AC current as described above and produced a field gradient to the beads on MC #2 or #3 which pulled them towards it. As soon as the beads were collected on the surface of MC #1, as shown in Figure 6.4 (b), the voltage across the GMR sensor started changing. The reduction of V_s continued until all the beads were collected on the conductor's surface (MC #1).

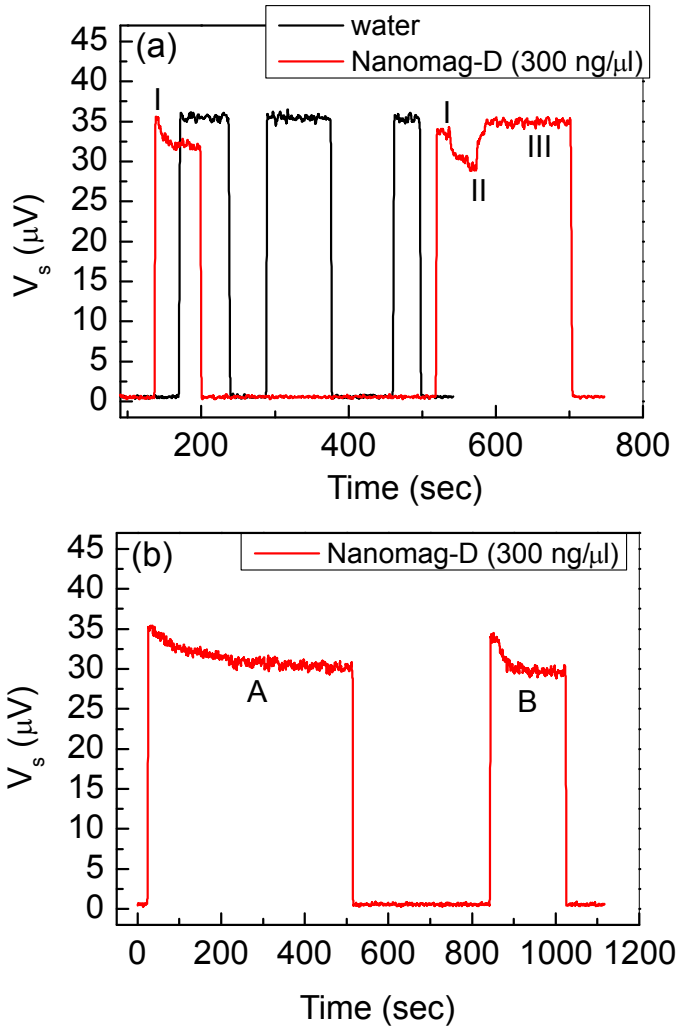

Figure 6.5: (a) Voltage drop V_s across the GMR sensor head due to the presence of water and water dispersible Nanomag-D beads of the concentration 300 ng/ml. (b) V_s for Nanomag-D beads transferred to the sensor proximity from different MCs (distance covered for A 36 µm and for B 18 µm).

Figure 6.5 (a) shows the sensor voltage (V_s) as a function of time (t) for water (injected in the reference channel) and Nanomag-D beads (injected in the measurement channel), using the same concentration of 300 ng/ml. The OFF and ON states labelled in the figure represent $I_s = 0$, $I_M = 0$ and $I_s \neq 0$, $I_M \neq 0$ (where I_s is a current flowing through the sensor and I_M the current flowing through

the conductor), respectively. In this study, the parameter of interest is the ON state for which V_s was recorded as a function of t. It can be seen that V_s remained almost unchanged with t when MC #1 was surrounded by water (reference sensor), indicating a negligible effect of water on V_s. On the other hand, the $V_s(t)$ measured for Nanomag-D beads on the surface of MC #1 (measurement sensor) showed a different behavior. Specifically, $V_s = V_{s,peak}$ (state I) was observed immediately after switching on the current (ON state) i.e. at $t = 0$ and then declined with time ($t \neq 0$) as shown in the first ON state for the nanobeads. In the second ON state for the nanobeads, V_s suddenly increased (state II) and regained the peak value (state III) when the beads were swiped off the sensor. The peak value (state III) is similar to the $V_{s,peak}$ (state I) observed at $t = 0$.

In real time observation of the motion of nanobeads, none of the nanobeads reached the surface of MC #1 at $t = 0$. As a result, the nanobeads induced no effect on the sensor voltage giving the peak value, $V_{s,peak}$. However, as the nanobeads reached the proximity of the sensor head i.e. on the surface of MC #1 for $t > 0$, V_s started reducing to a lower value. The drop in V_s was higher for a larger number of nanobeads on the surface of the conductor (MC #1) and the sensor head, but V_s increased again up to $V_{s,peak}$ when the nanobeads were removed from the conductor and the sensor head. When current was supplied to MC #1 for a longer time, so that all the nanobeads were collected on MC #1, the variation in V_s was observed as shown by the "ON states" in Figure 6.5 (b). It can be observed that with increasing t, V_s first decreased sharply, then slowed down, and finally reached saturation ($V_{s,sat}$). We define the time required to achieve $V_{s,sat}$ as the cutoff time, $t = t_{cutoff}$ for a particular measurement.

The falloff of V_s from $V_{s,peak}$ at $t = 0$ as the nanobeads reached on the surface of MC #1 i.e. approached the proximity of the sensor head. The return of V_s to a level of $V_{s,peak}$ after removing the nanobeads and water from MC #1 indicated that the decrease in V_s was purely due to the fringe field of the nanobeads. When the nanobeads were present on the surface of the GMR sensor head and/or on the AC-conductor (MC #1), they were magnetized and behaved as magnetic dipoles producing a stray field. This stray field disturbed/super-posited the fields produced by the MC and the sen-

sor itself, thereby modifying the net magnetic field which ultimately altered the orientation of the spins on the free layer of the spin valve sensor from their original directions. This eventually altered the resistance of the sensor that was observed in terms of the decrease in V_s. At $t = 0$ and when the nanobeads were swept off the conductor, they were far enough from the sensor head so that the effects of the stray field on the other magnetic fields present on the sensor proximity were negligible. Therefore, V_s maintained the constant peak level as in the case of water. The decrease in V_s can be explained by considering the high and low resistance directions of the spin moments. When the nanobeads were present in the proximity of the sensor and on the surface of MC #1, their magnetization was transverse to the sensor/MC length. This caused the magnetic moments in the free layer of the sensor to rotate towards a low resistance state, causing the decrease in V_s. With increasing number of nanobeads on the sensor's surface, most magnetic moments were rotated towards a lesser resistance state and V_s was therefore further decreased. When all the nanobeads reached MC #1 at $t = t_{cutoff}$, there was no further disturbance in the resultant magnetic field on the sensor head to change the angle of the spins so V_s remained unchanged ($V_s = V_{s,sat}$).

Thus, t_{cutoff} depends upon how fast the nanobeads are collected in the proximity of the sensor for a particular measurement. Ideally the nanobeads should reach the conductor simultaneously as the nanobeads are identical in composition (Fe_3O_4 Dextran -NH_2) and size (diameter, $\approx 250\,nm$). However, since the width of the MCs ($w = 10\,\mu m$) was fairly large, there was no control for the nanobeads to stick to a particular edge of the MCs. This limited the nanobeads from reaching to MC #1 altogether. Given that the nanobeads were identical and suspended in the same medium and attracted by the same magnetic field gradient, it is possible to estimate the initial position of the nanobeads by knowing t_{cutoff} or vice versa. For example, the ON states A and B in Figure 6.5 (b) show V_s recorded for the nanobeads transferred to MC #1 from MC #3 and MC #2, respectively. From the figure, one can clearly observe $t_{cutoff}(A) \approx 350\,sec$, which is about $4 * t_{cutoff}$ (B) ($\approx 100\,sec$), while maintaining a similar change in V_s in both cases. The nominal distances to the centres of MC #2 and MC #3 from the centre of MC #1 were $d_2 = 18$ and $d_3 = 36\,\mu m$ (i.e. $d_3 = 2d_2$), respectively. Therefore, the measured

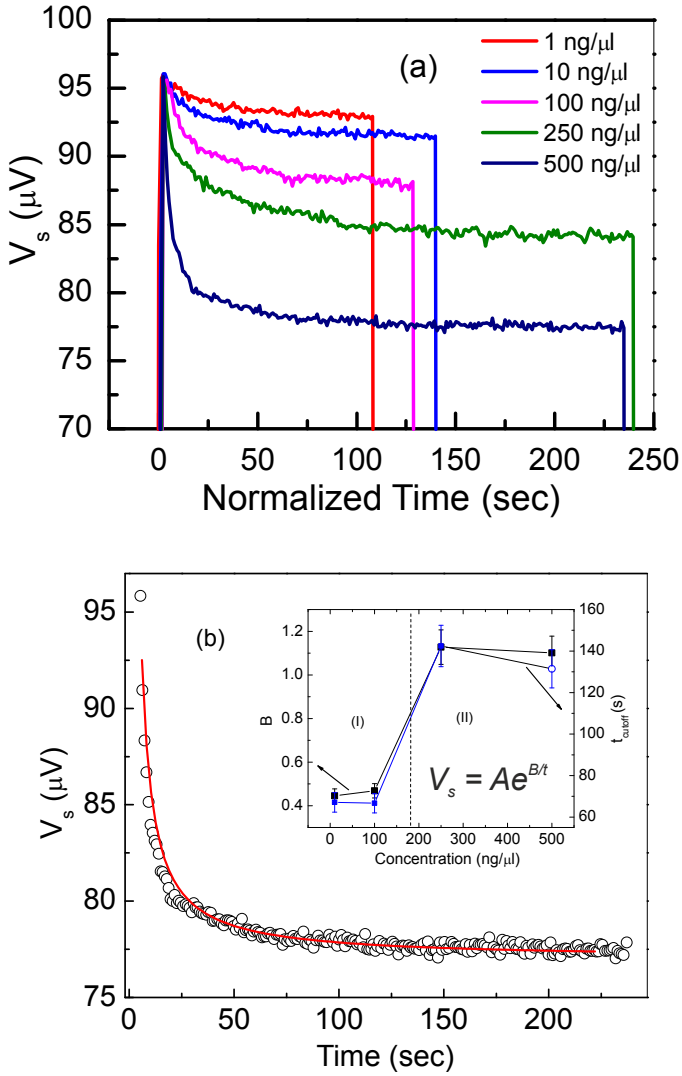

Figure 6.6: (a) Change in the sensor voltage with accumulation of superparamagnetic Nanomag-D beads on the micro-conductor with respect to the normalized time (t assumed zero at the beginning of the measurement); (b) the fit to V_s (t) for Nanomag-D beads of the concentration 500 ng/ml. Inset shows variations in the fitting parameter B and cutoff time with particle concentration and error bars deriving from the fitted curves.

value of the respective t_{cutoff} could be related to the nanobeads' original point of transfer towards the sensor head. In this case, by doubling the initial position of the nanomarker from the sensor head, the cutoff time increased by about 3.5 times. However, it should be recalled that if the nanobeads are far away from MC #1 such that the field gradient is negligible, they cannot be transferred to the sensor head.

Figure 6.6 shows V_s as a function of t measured for various concentrations in the range of 1 ng/ml - 500 ng/ml of the magnetic nanobeads. It can be observed that there was a larger drop in V_s (i.e. smaller values of $V_{s,sat}$) and a difference in t_{cutoff} when increasing the concentration of the nanobeads. The nanobeads of each concentration were transferred from MC #2 to MC #1, as described above, but V_s took longer time to reach its saturation $V_{s,sat}$ in the case of higher concentrations. With increasing concentration of the nanobeads on MC #1, the net stray field was increased; that impacted more the spin moments of the free layer of the sensor, thus leading to a state of lower resistance which ultimately resulted in the lower value of $V_{s,sat}$.

To better quantify the change trend in V_s with t with respect to change in the concentration of the nanobeads, we have developed a mathematical formulation to describe $V_s(t)$ as:

$$V_s(t) = Ae^{B/t} \tag{6.2}$$

where A and B are the fitting parameters. The experimental $V_s(t)$ data for all the concentrations were fitted using Equation 6.2, the representative result of which is shown in Figure 6.6 (b) for a given concentration of 500 ng/ml. From the best fits, A and B were extracted and plotted as functions of the nanobeads' concentration. We found that while A remained almost unchanged, B followed the variation trend of t_{cutoff} with increasing concentration of nanobeads. It can be seen in the inset of Figure 6.6 (b) that there existed a critical concentration of the nanobeads ($\approx$ 150 ng/ml), below and above which values of B and t_{cutoff} are remarkably different, denoted as "Regime I" and "Regime II", respectively. Since B and t_{cutoff} are associated with the detection rates of the sensor, such knowledge of their dependences on particle concentration is of practical importance in selecting an optimal particle concentration for rapid biodetection.

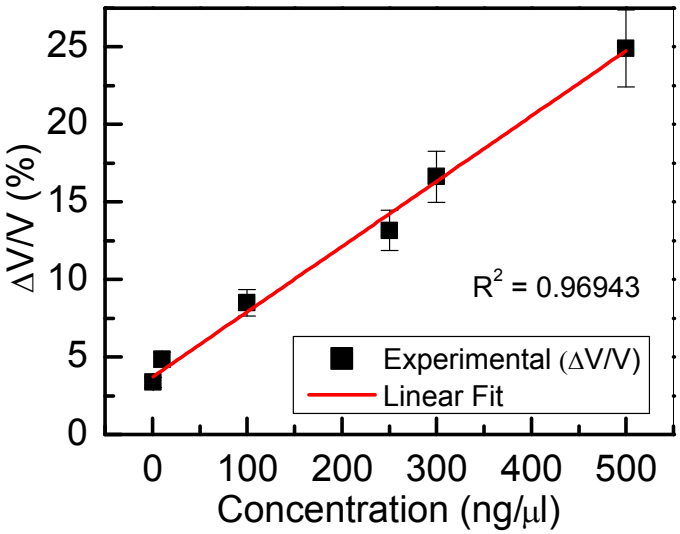

Figure 6.7: Relative change in the voltage across the GMR sensor head due to the presence of various concentrations of Nanomag-D beads on the MC.

From a biosensing perspective, a good biosensor should be capable of detecting low particle concentrations and effectively quantifying particle concentrations over a large and linear scale. [28] Therefore, in the present study we have calculated the relative change in voltage according to Equation 6.1 for various concentrations of Nanomag-D bead, which can be used to tag biomolecules when functionalized. The calculated results and their linear fits are shown in Figure 6.7. As one can see from this figure, $\Delta V/V$ increased linearly with the concentration of Nanomag-D beads in the entirely investigated range, from 3.4% for 1 ng/ml to 24.9% for 500 ng/ml.

6.4 Conclusions

In this study, we detected particle concentrations as low as 500 pg/µl, quantified them in a linear scale over a wide particle concentration range (1-500 ng/µl) and measured the sensor voltage for a collection of approximately 20 nanobeads directly above the GMR sensor. We observed a clear decrease in V_s, and the corresponding DV/V ratio was determined to be about 1.5%. Our developed sensor also covers a wider linear sensing range in comparison to the range offered by

other sensors based on nanoparticles. [5,8,29–31]

We have proven the application of a spin valve GMR integrated microfluidic platform for the detection of very low concentrations and quantification of mass coverage of Nanomag-D beads of 250 nm diameter. As several biological identities can be tagged to these nanobeads once they are properly functionalized, the developed sensor has potential for a rapid, portable, and reliable diagnosis of diseases. Experiments are currently being carried out to prove this statement.

Acknowledgements

Research at the Vienna University of Technology was supported by the Austrian Science Fund (FWF) with Project Nr: P 24372- N19. Research at the University of South Florida was supported by the Florida Cluster for Advanced Smart Sensor Technologies (FCASST) and by USAMRMC through grant numbers W81XWH- 07-1-0708 and W81XWH1020101/3349. JD acknowledges the USF Frank Duckwall Research Fellowship and the Vienna University of Technology Fellowship.

Bibliography

[1] T. Aytur, J. Foley, M. Anwar, B. Boser, E. Harris, and P. R. Beatty, "A novel magnetic bead bioassay platform using a microchip-based sensor for infectious disease diagnosis," *Journal of immunological methods*, vol. 314, no. 1, pp. 21–29, 2006.

[2] N. Sanvicens, C. Pastells, N. Pascual, and M.-P. Marco, "Nanoparticle-based biosensors for detection of pathogenic bacteria," *TrAC Trends in Analytical Chemistry*, vol. 28, no. 11, pp. 1243–1252, 2009.

[3] B. Pejcic, R. De Marco, and G. Parkinson, "The role of biosensors in the detection of emerging infectious diseases," *Analyst*, vol. 131, no. 10, pp. 1079–1090, 2006.

[4] J.-i. Hahm, "Functional polymers in protein detection platforms: Optical, electrochemical, electrical, mass-sensitive, and magnetic biosensors," *Sensors*, vol. 11, no. 3, pp. 3327–3355, 2011.

[5] J. B. Haun, T.-J. Yoon, H. Lee, and R. Weissleder, "Magnetic nanoparticle biosensors.," *Wiley Interdisciplinary Reviews: Nanomedicine and Nanobiotechnology*, vol. 2, pp. 291–304, may 2010.

[6] J. Llandro, J. J. Palfreyman, A. Ionescu, and C. H. W. Barnes, "Magnetic biosensor technologies for medical applications: a review," *Medical & biological engineering & computing*, vol. 48, no. 10, pp. 977–998, 2010.

[7] G. Li, S. Sun, R. J. Wilson, R. L. White, N. Pourmand, and S. X. Wang, "Spin valve sensors for ultrasensitive detection of superparamagnetic nanoparticles for biological applications.," *Sensors and actuators. A, Physical*, vol. 126, pp. 98–106, jan 2006.

[8] S. X. Wang and G. Li, "Advances in giant magnetoresistance biosensors with magnetic nanoparticle tags: review and outlook," *Magnetics, IEEE Transactions on*, vol. 44, no. 7, pp. 1687–1702, 2008.

[9] D. R. Baselt, G. U. Lee, M. Natesan, S. W. Metzger, P. E. Sheehan, and R. J. Colton, "A biosensor based on magnetoresistance technology," *Biosensors and Bioelectronics*, vol. 13, no. 7, pp. 731–739, 1998.

[10] J. Devkota, T. Mai, K. Stojak, P. Ha, H. Pham, X. Nguyen, P. Mukherjee, H. Srikanth, and M. Phan, "Synthesis, inductive heating, and magnetoimpedance-based detection of multifunctional Fe3O4 nanoconjugates," *Sensors and Actuators B: Chemical*, vol. 190, pp. 715–722, jan 2014.

[11] R. S. Gaster, L. Xu, S.-J. Han, R. J. Wilson, D. A. Hall, S. J. Osterfeld, H. Yu, and S. X. Wang, "Quantification of protein interactions and solution transport using high-density GMR sensor arrays," *Nature nanotechnology*, vol. 6, no. 5, pp. 314–320, 2011.

[12] G. Kokkinis, F. Keplinger, and I. Giouroudi, "On-chip microfluidic biosensor using superparamagnetic microparticles," *Biomicrofluidics*, vol. 7, no. 5, p. 54117, 2013.

[13] H. Wang, "Magnetic sensors for diagnostic medicine: CMOS-based magnetic particle detectors for medical diagnosis applications," *Microwave Magazine, IEEE*, vol. 14, no. 5, pp. 110–130, 2013.

[14] I. Koh and L. Josephson, "Magnetic nanoparticle sensors.," *Sensors (Basel, Switzerland)*, vol. 9, pp. 8130–45, jan 2009.

[15] I. Giouroudi and F. Keplinger, "Microfluidic biosensing systems using magnetic nanoparticles," *International Journal of Molecular Sciences*, vol. 14, pp. 18535–18556, jan 2013.

[16] G. Binasch, P. Grünberg, F. Saurenbach, and W. Zinn, "Enhanced magnetoresistance in layered magnetic structures with antiferromagnetic interlayer exchange," *Physical review B*, vol. 39, no. 7, p. 4828, 1989.

[17] M. N. Baibich, J. M. Broto, A. Fert, F. N. Van Dau, F. Petroff, P. Etienne, G. Creuzet, A. Friederich, and J. Chazelas, "Giant magnetoresistance of (001) Fe/(001) Cr magnetic superlattices," *Physical review letters*, vol. 61, no. 21, p. 2472, 1988.

[18] P. P. Freitas, R. Ferreira, S. Cardoso, and F. Cardoso, "Magnetoresistive sensors," *Journal of Physics: Condensed Matter*, vol. 19, no. 16, p. 165221, 2007.

[19] F. Li and J. Kosel, "A magnetic method to concentrate and trap biological targets," *Magnetics, IEEE Transactions on*, vol. 48, no. 11, pp. 2854–2856, 2012.

[20] D. Mark, S. Haeberle, G. Roth, F. von Stetten, and R. Zengerle, "Microfluidic lab-on-a-chip platforms: requirements, characteristics and applications," *Chemical Society Reviews*, vol. 39, no. 3, pp. 1153–1182, 2010.

[21] F. Li and J. Kosel, "A Magnetic Biosensor System for Detection of E. coli," *Magnetics, IEEE Transactions on*, vol. 49, pp. 3492–3495, jul 2013.

[22] W. Shen, B. D. Schrag, M. J. Carter, J. Xie, C. Xu, S. Sun, and G. Xiao, "Detection of DNA labeled with magnetic nanoparticles using MgO-based magnetic tunnel junction sensors," *Journal of Applied Physics*, vol. 103, no. 7, p. 7A306, 2008.

[23] S. Halldorsson, E. Lucumi, R. Gómez-Sjöberg, and R. M. T. Fleming, "Advantages and challenges of microfluidic cell culture in polydimethylsiloxane devices," *Biosensors and Bioelectronics*, vol. 63, pp. 218–231, 2015.

[24] F. Li, I. Giouroudi, and J. Kosel, "A biodetection method using magnetic particles and micro traps," *Journal of Applied Physics*, vol. 111, no. 7, p. 07B328, 2012.

[25] M. Colombo, S. Carregal-Romero, M. F. Casula, L. Gutierrez, M. P. Morales, I. B. Boehm, J. T. Heverhagen, D. Prosperi, and W. J. Parak,

"Biological applications of magnetic nanoparticles," *Chemical Society Reviews*, vol. 41, no. 11, pp. 4306–4334, 2012.

[26] Q. a. Pankhurst, J. Connolly, S. K. Jones, and J. Dobson, "Applications of magnetic nanoparticles in biomedicine," *Journal of physics D: ...*, vol. 167, pp. R167–R181, jul 2003.

[27] G. Kokkinis, M. Jamalieh, F. Cardoso, S. Cardoso, F. Keplinger, and I. Giouroudi, "Magnetic-based biomolecule detection using giant magnetoresistance sensors," *Journal of Applied Physics*, vol. 117, p. 17B731, may 2015.

[28] R. Ahmad, M. Vaseem, N. Tripathy, and Y.-B. Hahn, "Wide linear-range detecting nonenzymatic glucose biosensor based on CuO nanoparticles inkjet-printed on electrodes," *Analytical chemistry*, vol. 85, no. 21, pp. 10448–10454, 2013.

[29] J. Devkota, C. Wang, A. Ruiz, S. Mohapatra, P. Mukherjee, H. Srikanth, and M. H. Phan, "Detection of low-concentration superparamagnetic nanoparticles using an integrated radio frequency magnetic biosensor," *Journal of Applied Physics*, vol. 113, no. 10, p. 104701, 2013.

[30] J. Schotter, P. B. Kamp, A. Becker, A. Pühler, D. Brinkmann, W. Schepper, H. Brückl, and G. Reiss, "A biochip based on magnetoresistive sensors," *Magnetics, IEEE Transactions on*, vol. 38, no. 5, pp. 3365–3367, 2002.

[31] J. C. Rife, M. M. Miller, P. E. Sheehan, C. R. Tamanaha, M. Tondra, and L. J. Whitman, "Design and performance of GMR sensors for the detection of magnetic microbeads in biosensors," *Sensors and Actuators A: Physical*, vol. 107, no. 3, pp. 209–218, 2003.

Chapter 7
Publication F

Detection and quantification of alginate functionalized magnetic nanoparticles on a surface modified magnetoresistive biosensor

Authored by G. Kokkinis, M. Jamalieh, J. Devkota, S. Cardoso, H. Srikanth, M.H. Phan and I. Giouroudi.
Published in *Proceedings of the* 19^{th} *International Conference on Miniaturized Systems for Chemistry and Life Sciences.* October 25-29, (2015), Gyeongju, KOREA.

Abstract

In this paper we present a simple, versatile, portable microfluidic biosensor for the detection and quantification of biomarkers such as proteins, antibodies or anti-cancer drugs conjugated with iron oxide (Fe_3O_4) magnetic nanoparticles (MNs) and suspended into a static fluid. The designed system utilizes Giant Magnetoresistance (GMR) spin valve sensors and microconductors for the manipulation of the nanoparticles, integrated on a microfluidic chip with a modified surface for preventing biofouling. In this study we used MNs encapsulated into a polymeric matrix of Alginate, which are perfect candidates for applications in biomedicine and for being an important carrier for different biological agents.

Keywords: Biosensor, Magnetic Nanoparticles, Alginate, GMR.

7.1 Introduction

Magnetic nanoparticles play an increasingly important role in biotechnology due to the vast possibilities for use in medical applications that range from magnetic separation and contrast enhancement for imaging to diagnostics and quantification platforms for genomics and proteomics. [1–3] Among the different functionalizations of magnetic nanoparticles, lately, alginate encapsulated iron oxide nanoparticles draw attention due to their biocompatibility, the straightforward gelation with divalent cations [4] and for being an important carrier for different biological agents. [5]

In this paper we present a microfluidic chip (Figure 7.1), with integrated magnetic field inducing microconductors for the manipula-

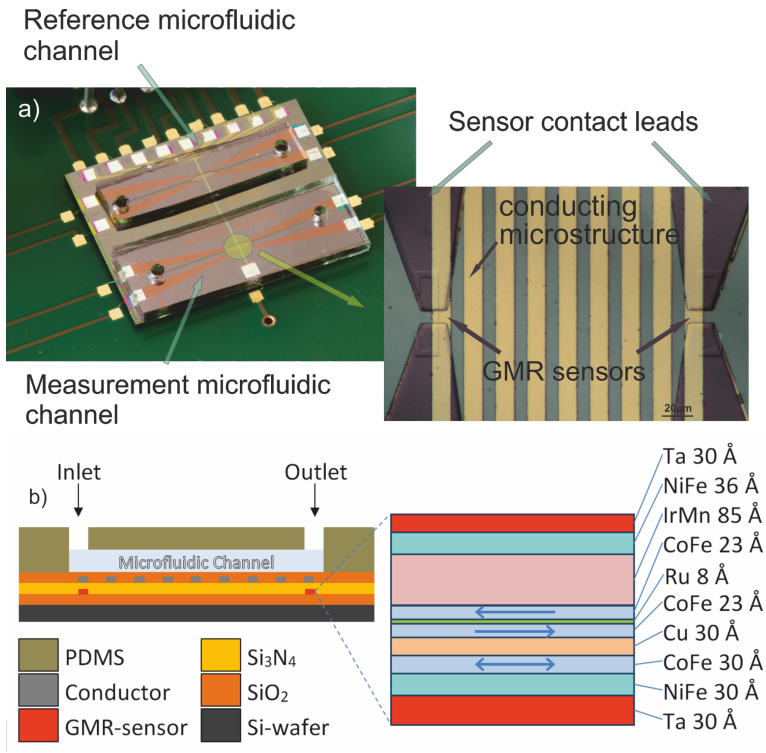

Figure 7.1: (a)Photograph of the proposed microfluidic chip mounted on a PCB board. In the accompanied microscope image the GMR sensors with their connecting leads and the micro conductors' area are shown. (b) Cross section of the chip with a detailed GMR, spin valve sensor element.

tion and magnetization of the MNs, integrated GMR sensors for the detection of the MNs and a modified surface to prevent biofouling, non-specific binding and enabling the possibility for multiple uses of the chip. All the operations on chip are held in a static fluid and the channels are filled with capillary forces alone restraining the need for pumps or other integrated microfluidic components. This in combination with a signal generation and acquisition system realized on a laptops soundcard proclaims the use of the proposed system as a point of care, portable, biosensor.

7.2 Experimental

The biosensors operation is realized in two steps; once the sample is loaded a pre-concentration step is essential as it significantly lowers the LOD (Limit Of Detection) of the biosensor and the amounts of reagent needed thus improving the overall performance. Sequentially switching ON and OFF a current through microconductors (MCs) induces a ”moving” magnetic field gradient, which attracts the MNs from one MC and moves them to the next (Figure 7.2). At the end of the sequential actuation all the MNs - previously scattered over the area of the MCs - are concentrated on one conductor, which is the last MC to be turned ON.

Then the detection itself takes place; the last MC (#2) that is actuated during the pre-concentration step is situated a few micrometers away from a magnetic field sensor. Once the MNs are concentrated on it, the MC right above the sensor (MC #1, Figure 7.2) is actuated

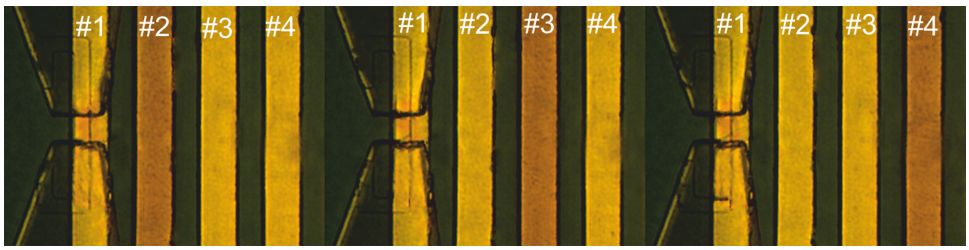

Figure 7.2: Sequential actuations of the MCs and manipulation of the MNs as a pre-concentration step. MNs are attracted to the current currying MCs and are finally concentrated on MC #2.

with an AC current. This AC current both induces a magnetization to the paramagnetic iron oxide particles and attracts them to the vicinity of the sensor which then detects their stray fields. The time the particles need to accumulate on the sensors surface and the magnitude of the sensors output determine their concentration. Furthermore, the time required until the saturation of the sensors signal can be used to define the size difference between the conjugated (with a biomolecule) MNs and plain MNs that are measured in a reference channel (Figure 7.1). That is because conjugated MNs exhibit greater hydrodynamic friction (Stokes drag force) with respect to the plain MNs and/or greater friction force when moving in contact with the chips surface as in the proposed system. [6]

The MNs used in this study are magnetite nanoparticles synthesized by co-precipitation of ferric and ferrous hydroxide in alkaline conditions. In order to be coated with alginate, the MNs were dispersed in an alginate solution, resulting in spherical MNs with an average size of 10 nm $\pm$ 2.5 nm. More details about the studied MNs and their magnetic characterization are reported by Devkota *et al*. [5]

Alginate exhibits adhesion to commonly used passivation materials i.e SiO_2 and Si_3N_4. Thus, a surface modification of the biosensor was necessary. Since alginate is a hydrogel, in which the magnetic iron oxide core of the particles has been engulfed, it repels hydrophobic surfaces. For that reason we developed such a hydrophobic surface modification by immobilizing a monolayer of perfluorinated alkoxysilane [7] on the SiO_2 surface of the biosensor. The monolayer was evaluated with a spectral reflectometer and it was found to be 2.17 nm thick, marginally influencing the sensor's performance.

7.3 Results and discussion

The exact acquisition scheme and experimental set-up have been described in detail elsewhere. [8, 9] Three different concentrations of alginate encapsulated iron oxide nanoparticles suspended in deionized water were prepared, injected into the microfluidic channel and detected using the aforementioned procedure; when the MC on top of the sensor was turned ON, the MNs, previously concentrated on the MC #2 (Figure 7.2), started moving towards the sensor changing

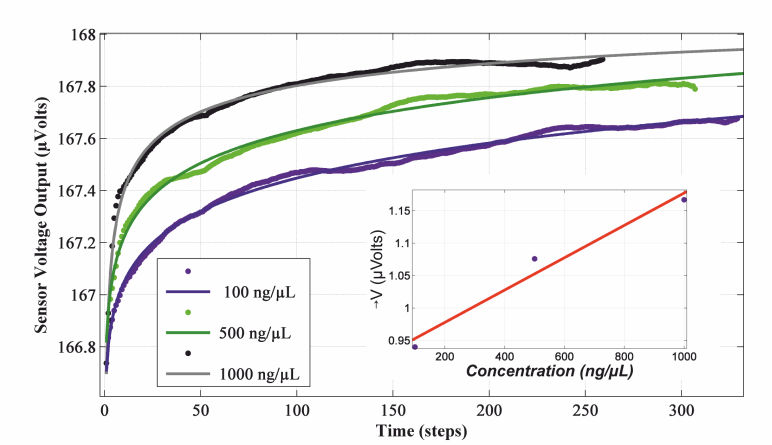

Figure 7.3: Change of the sensor's output voltage with the ac-cumulation of the MNs on its surface versus time. Inset shows the linear ascent of ΔV with concentration.

its voltage output. The change of the sensors output is reported in Figure 7.3, where the response of the sensor to the motion of the MNs has been plotted over time for the three concentrations. Each time step corresponds to 120 msec. The curves were fitted to the equation using an itinerary process in Matlab®. The initial value of the sensor's output is the same for all three concentrations and is due to the magnetic field of the MC #1. The final value and thus the $\Delta V = V_{fin} - V_{init}$ follows a linear increase with goodness of fitting $R^2 = 0.95$ (Figure 7.3, inset).

7.4 Conclusions

The linearity of the GMR sensor's over concentration supports the argument that the pro-posed biosensor can be used for the detection and quantification of alginate functionalized MNs. Further experiments are carried out in order to define the sensor's range and LOD.

Acknowledgements

Research at the Vienna University of Technology was supported by the Austrian Science Fund (FWF) with Project Nr: P 24372-N19. Research at the University of South Florida was supported by USAMRMC through grant numbers W81XWH-07-1-0708 and W81XWH1020101/3349. INESC-MN acknowledges FCT funding through the IN Associated Laboratory (Pest-OE/CTM/LA0024/2011) and Project EXCL/CTM-NAN/0441/2012.

Bibliography

[1] L. Zhang, F. X. Gu, J. M. Chan, A. Z. Wang, R. S. Langer, and O. C. Farokhzad, "Nanoparticles in medicine: therapeutic applications and developments," *Clinical pharmacology and therapeutics*, vol. 83, no. 5, pp. 761–769, 2008.

[2] M. Gao, C. Deng, and X. Zhang, "Magnetic nanoparticles-based digestion and enrichment methods in proteomics analysis," *Expert Review of Proteomics*, vol. 8, pp. 379–390, jun 2011.

[3] J. Gao, H. Gu, and B. Xu, "Multifunctional magnetic nanoparticles: design, synthesis, and biomedical applications," *Accounts of chemical research*, vol. 42, no. 8, pp. 1097–1107, 2009.

[4] A. Jejurikar, G. Lawrie, D. Martin, and L. Grøndahl, "A novel strategy for preparing mechanically robust ionically cross-linked alginate hydrogels.," *Biomedical materials (Bristol, England)*, vol. 6, no. 2, p. 025010, 2011.

[5] J. Devkota, T. T. T. Mai, K. Stojak, P. T. Ha, H. N. Pham, X. P. Nguyen, P. Mukherjee, H. Srikanth, and M. H. Phan, "Synthesis, inductive heating, and magnetoimpedance-based detection of multifunctional Fe3O4 nanoconjugates," *Sensors and Actuators B: Chemical*, vol. 190, pp. 715–722, jan 2014.

[6] G. Kokkinis, F. Keplinger, and I. Giouroudi, "On-chip microfluidic biosensor using superparamagnetic microparticles.," *Biomicrofluidics*, vol. 7, p. 054117, jan 2013.

[7] A. Datta, A. Dhar, P. Kuban, R. Manor, I. Ahmad, S. Gangopadhyay, T. Dallas, M. Holtz, H. Temkin, and P. Dasgupta, "Microfabrication and

characterization of teflon af-coated liquid core waveguide channels in silicon," *IEEE Sensors Journal*, vol. 3, pp. 788–795, dec 2003.

[8] G. Kokkinis, M. Jamalieh, F. Cardoso, S. Cardoso, F. Keplinger, and I. Giouroudi, "Magnetic-based biomolecule detection using giant magnetoresistance sensors," *Journal of Applied Physics*, vol. 117, p. 17B731, may 2015.

[9] J. Devkota, G. Kokkinis, T. Berris, M. Jamalieh, S. Cardoso, F. A. Cardoso, H. Srikanth, M.-H. Phan, and I. Giouroudi, "A novel approach for detection and quantification of magnetic nanomarkers using a spin valve GMR-integrated microfluidic sensor," *RSC Advances*, 2015.

Chapter 8
Publication G

Magnetic Microfluidic Single Cell Trapping and Analysis Platform

Authored by G. Kokkinis, R. Mitterbck, T. Berris, M. Jamalieh, F. Keplinger, I. Giouroudi.
Accepted for publication in the Journal *JMAST,*.

Abstract

This paper presents the design and realization of a portable and cost effective microfluidic platform for trapping and studying the mechanical properties of single cancer cells in suspension. The innovative aspect of the presented trapping method is that it uses magnetic microparticles (MPs) to label the cancer cells and then trap those using microchambers with integrated current carrying microconductors. These intact single cells can then be used for studying their mechanical properties and for additional testing and patient specific drug screening. Developing patient specific therapies can be enabled by analysing the cancer cells' metastasis-driving capabilities on the single cell level.

Keywords: single cell analysis, magnetic trapping, microfluidics.

8.1 Introduction

Metastasis is the process in which cancer cells migrate from the primary tumor site by entering the peripheral blood stream. [1] These circulating tumor cells (CTCs) may invade healthy tissue and create secondary tumor sites [2]. CTCs could act as biomarkers for cancer

diagnostics and prognostics. [3] The hope in CTC research lies in the use of these rare cells in circulation as an accessible "fluid biopsy" that would permit frequent, minimally invasive sampling of tumor cells for molecular and biophysical assessment. [4] Analysing their physical and mechanical properties on a single cell level could assist on understanding their underlying metastasis-driving capabilities. Therefore the development of a highly efficient method for their isolation, trapping and *in vitro* characterization will be a technical advantage over all currently used methods.

Microscale methods such as on-chip magnetic microfluidic platforms show great promise and superiority for *in vitro* capturing and single cell analysis. Most of the reported methods utilizing microfluidics for the confinement of specific cancer cells are based on coating the microfluidic surfaces or microstructures, fabricated inside the microfluidic channels, with antibodies against epithelial cell markers or tumor-specific antigens such as EpCAM or PSMA. [1, 5] The biggest disadvantage of this type of capturing method, which depends on a biological functionalization layer (e.g. antibodies, antigens), is that it is prone to time dependent changes of this functionalization layer such as aging and contamination. Long-term system stability is therefore an issue. This can be effectively overcome by utilizing the method presented in this paper since no functionalization layer on top of the microfluidic surface is required.

In the presented method only functionalized MPs, which are commercially available, are utilized as labels for the cancer cells prior to isolation; the combination with microfluidics will theoretically increase the interaction opportunities of the cancer cells with the functionalized MPs by orders of magnitude due to the reduction in dimensions. As a result, the capture efficiency will be significantly increased and the reaction time can be reduced. Moreover, the capturing procedure is based only on the application of a magnetic field. On reported methods utilizing microfluidics and MPs for the isolation of cancer cells the MPs were manipulated by an applied field generated by an externally positioned permanent magnet. [6] With this method the applied magnetic field strength cannot be controlled and it also does not favor miniaturization and integration on a single chip. On the contrary, in our presented method the application of the magnetic field is based on current carrying microstructures

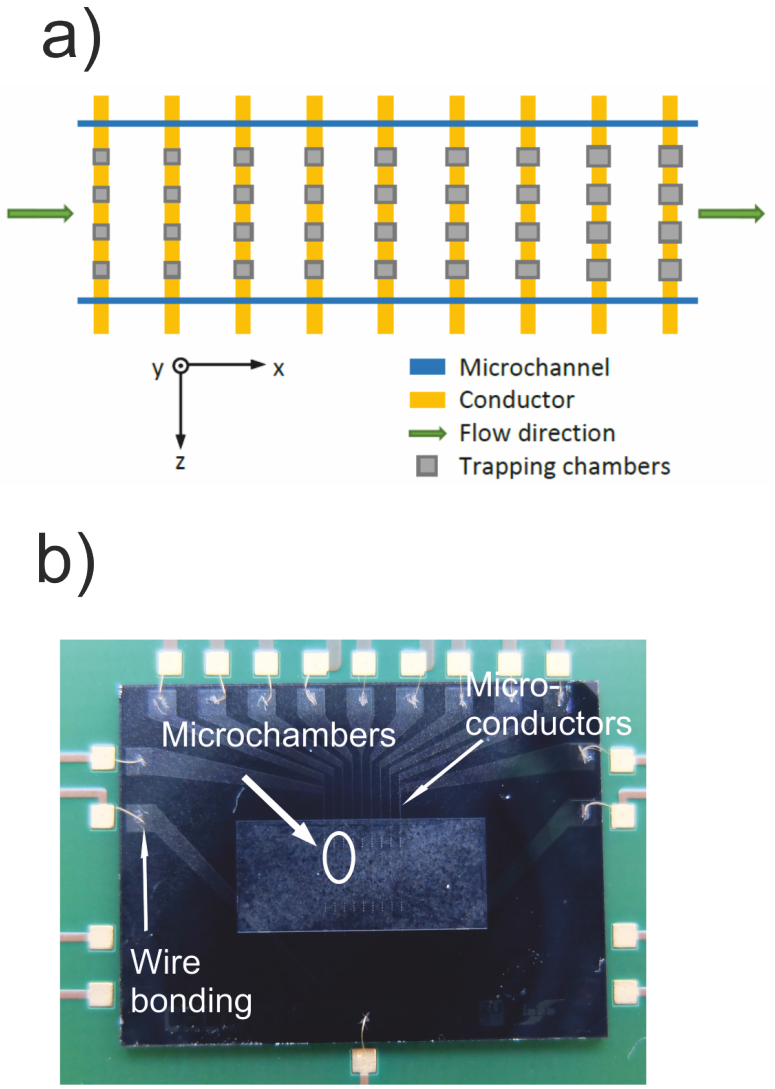

Figure 8.1: (a) Depiction of the microtraps along the current carrying conductors. The blue lines mark the walls of the microchannel. (b) Photograph of the actual chip with its passivation layer. The microconductors and the microchambers can be seen.

which produce a magnetic field gradients strong enough to manipulate and isolate the magnetically labeled cells inside the microchambers. By using these current carrying microstructures, which offer an integrated solution, we can easily control theapplied field's strength by adjusting the applied current to the microstructures.

8.2 Methods

8.2.1 Working Principle

The presented magnetic microfluidic platform consists of a microfluidic channel made of PDMS and several trapping microchambers fabricated by photolithographically patterning a dry photoresist thin film (Ordyl®). The cancer cells in the liquid sample are labeled with commercially available functionalized MPs which have selective affinity to these cells. Current carrying gold (Au) microstructures (microconductors) are fabricated underneath the microtraps using evaporation deposition technique and photolithography; this way, the trapping of the magnetically labeled cells is achieved. Figure 8.1 (a) shows a schematic of the microconductors and the microchambers and Figure 8.1 (b) shows the developed isolation platform.

The trapping procedure has as follows; the sample containing the cancer cells is first mixed with the functionalized MPs to ensure labeling of the cells. Then it is injected into the microfluidic channel. Current is applied sequentially at the microconductors by means of a programmable microcontroller and a power supply. This causes a magnetic force to act on the magnetically labeled cells which flow through the microchannel along the x-axis. This perpendicular to the motion of the labeled cells, magnetic force attracts them, and captures them inside the microchambers. Once captured, the magnetically labeled cell remains in the microchamber even when the current applied at the microconductor is switched off; this is due to the low fluid velocity in the microchamber. This captured cell can now be used for further analysis (e.g. studying of its mechanical properties). Other cells and parts of the fluid do not get influenced by the microchamber or the trapped cells and can pass by the section without problems.

In order to study the mechanical properties of the single magnetically labeled and trapped cells an additional magnetic force is externally applied on them managing to deform them; by means of CCD cameras and a 3D grid we can optically measure their deformation, calculate the elasticity modulus and thus study their mechanical properties. It has to be noted that the channel and trap dimensions are optimized to protect the cells from shear stress and achieve high trapping efficiency.

8.2.2 Fabrication

All fabrication steps were carried out in a cleanroom to prevent contamination of the device. The microconductors were produced using standard photolithography on a Si wafer; the microstructures were fabricated with thermal evaporation and deposition of gold (Au). The thickness of the microconductors was 1 µm after simulations with COMSOL® Multiphysics indicated this value as the optimum for the given application. After sputtering of the microconductors, the complete chip was passivated leaving only the bonding pads exposed. The microchambers were directly positioned on top of the chip with a layer made out of "Ordyl® SY300", which is a negative dry-film photoresist. Ordyl® is available in different thicknesses starting with 17 µm, which was used for the developed device. It was directly laminated onto the wafer and then patterned with standard photolithography. The lamination was made by an office laminator preheated to 121 °C. The wafer was placed between an overhead transparency and its paperback (Folex-X472). Afterwards, the Ordyl® SY300 was positioned on top of the wafer and fixed with tape on the paperback. Then the complete stack of overhead transparency, wafer and Ordyl® was inserted into the laminator. The bottom protective foil of the Ordyl® was slowly removed during the movement through the laminator so that the Ordyl® binds to the surface of the wafer. After lamination the overhead transparency was removed and the wafer with the Ordyl® on top were brought to the cleanroom in an UV-secure wafer carrying case (wafer was positioned topside down). Note that the other protective layer on top of the Ordyl® was still in place and removed later after exposure. The wafer (with the Ordyl already laminated) was preheated to 90 °C. Meanwhile a

chromium shadow mask with the design of the microchambers was put into the mask aligner. Marks on the wafer, fabricated on the same step with the microconductors, were used to align the Ordyl® layer with the later. After alignment the wafer with the Ordyl® on top was exposed for 20 sec to harden (photopolimerize) the desired structure. Afterwards the top protective layer was pulled off and the wafer was put on the hot plate again for 1 minute at 90 °C for the Post Exposure Bake (PEB). The last step was the development in an ultrasonic bath filled with Ordyl® developer for 60 sec. The processed Ordyl® is thinner than the original one at the end, due to the Soft Bake (pre exposure bake). Hence the thickness was reduced from 17 µm to 12 µm, which is appropriate for the presented application. A photo of the chip with the Ordyl® layer is shown in Figure 8.1 (b).

The microfluidic channel used for the cell trapping device was fabricated using PDMS (Polydimethylsiloxane). The channel consist of an inlet, an outlet, a straight part for fluid transportation and a wider trapping/measurement area as shown in Figure 8.2. The channel was fabricated using Ordyl® structured by standard soft lithography and used as a mold for the PDMS channel. The PDMS is an organosilicon polymeric compound, which is prepared by mixing in a ratio of 10:1 the monomer and the curing agent (both viscous liquids). After mixing the liquid was poured over the mold, degassed and cured for 1 hour at 70 °C on the hot plate. In the last step the

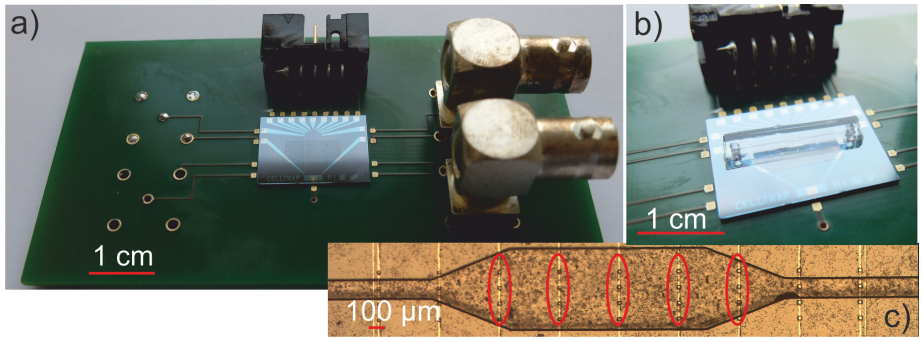

Figure 8.2: (a) Photo of the device and its connectors. (b) The PDMS channel positioned over the microtrapping area of the chip. (c) Micro-photograph of the PDMS channel over the conductors and the microtraps. The microtraps along the microconductors are visible.

PDMS was gently pilled off the molds surface.

8.3 Simulations

Simulations using COMSOL® Multiphysics were carried out in order to determine the range of magnetic forces that need to be applied in order to adequately deform the cells without breaking the bond between MP and cell and without damaging the cell itself. We concluded that by applying a perpendicular magnetic pressure of $10\,\mathrm{pN}/\mu\mathrm{m}^2$, a maximum displacement of $4.12\,\mu\mathrm{m}$ occurs in the z-axis. Figures 8.3 (a),(b) show the simulation results. These simulations indicated that it is possible to deform cells by applying on them forces in the range of pN that are feasible by the magnetic means on that size scales.

8.3.1 Jurkat Cells

The presented platform was tested using T-Lymphocyte cells as the cancer cells, originating from an acute T cell leukaemia. The cell line is called "Jurkat cells" and was established from the peripheral blood of a 14 year old boy in 1977 [1]. [7] The cells were provided by "BOKU University of Natural Resources and Life Sciences, Vienna"

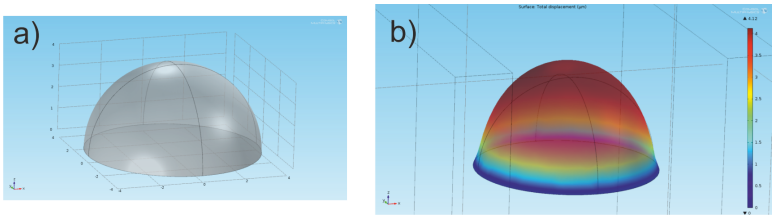

Figure 8.3: (a) A cell of $4.5\,\mu\mathrm{m}$ radius on a flat surface before applying any force to its surface. (b) The deformed cell after the application of $10\,\mathrm{pN}/\mu\mathrm{m}^2$.

[1] "ATCC", 2014. Available: http://www.lgcstandards-atcc.org/products/all/TIB-152.aspx

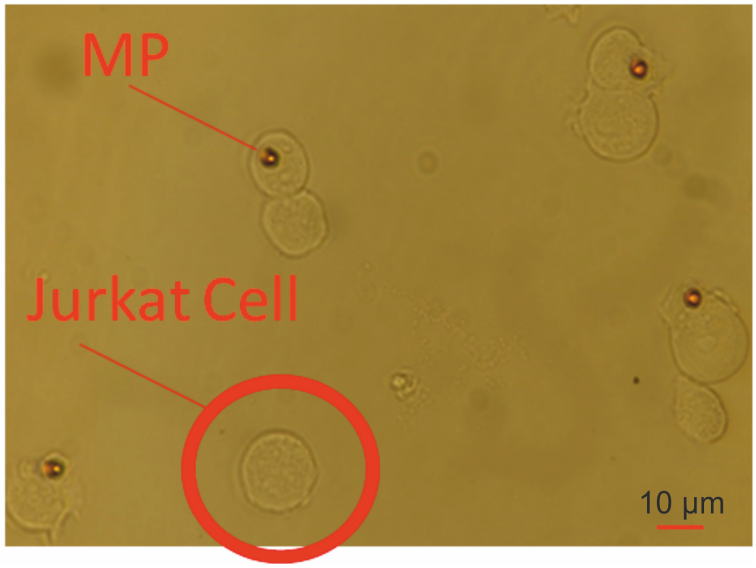

Figure 8.4: Micro-photograph of Labelled and unlabeled Jurkat cells.

[2] and cultured by the "Austrian Institute of Technology" (AIT) [3]. After culturing, the cells were placed into 1 ml tubes with 1 million cells each and put onto a rack for storage. The complete rack was transported in a polystyrene box to maintain the temperature. The cells were stored at 37 °C and usually they were viable and usable for 7 days. However, best results were obtained in the first three days. For the magnetic labeling of the cells 2 µl of "M-450 Dynabeads" (suspension with 800.000 particles) functionalized with Anti-CD3-antibodies were used (diameter of 4.5 µm and susceptibility of 1.6) and were added to the cells (1 million cells). The reaction tube was then placed for 20 min into a multi rotator. To achieve high magnetic labeling rates of the Jurkat cells and prevent contamination of the samples and the final products all mixing tasks were performed in a semi-sterile environment. The working area was cleaned with isopropanol before usage and most tasks were accomplished under a laminar flow hood. The binding rate was always controlled under

[2] "BOKU - University of Natural Resources and Life Sciences", 2014. Available: http://www.boku.ac.at/en/.

[3] "Austrian Institute of Tehcnology," 2014. Available: http://www.ait.ac.at/

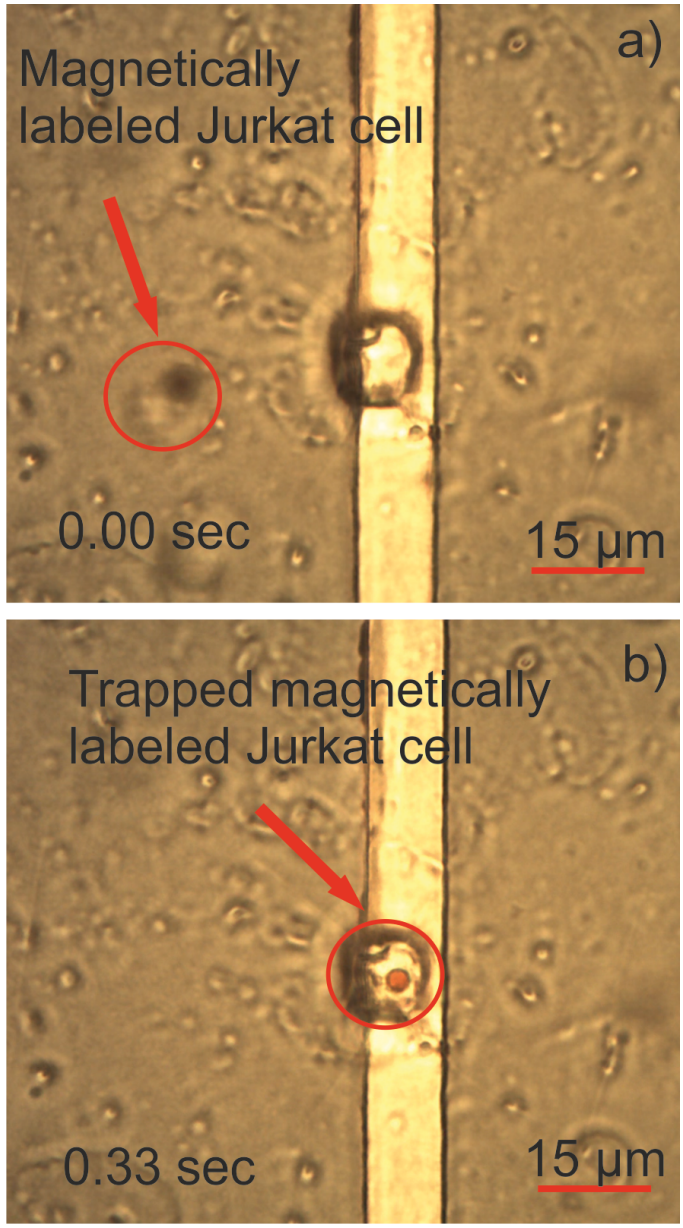

Figure 8.5: (a) A labelled Jurkat cell approaching the microtrap on the surface of the current carrying microconductor, appearing blur due to shallow depth of field and focusing on the microconductor's plane. (b) The labelled cell after it has been trapped.

a microscope. Figure 8.4 shows the magnetically labeled Jurkat cells.

8.3.2 Experiments

Preliminary trapping experiments were successfully carried out with the above mentioned magnetically labeled Jurkat cells. The cells were introduced to the channel through the inlet with an estimated velocity of about 50 µm/sec. It was observed that the microchambers were not influencing the flow of the cells when the microconductors were switched off. In order to begin with the trapping procedure 150 mA were sequentially applied to the microconductors. Figure 8.5 shows the trapping of a single magnetically labeled Jurkat cell. All pictures were taken with a 60-fold lens and above microconductor Nr. 4 (17×17 µm). After the microconductor was switched off it was clearly observed that the cell remains trapped.

8.4 Conclusions

The measurements showed that with the presented platform we successfully managed to trap single cancer cells and hold them in that position for further analysis without permanently applying electric current and magnetic field. By using the presented configuration of the cell trapping platform the fluid flow over the microchambers is neither influenced by the trapped cells nor by the empty microtraps. Finally, clustering did not in the channel even when all microchambers were filled. Simulations proved that it is possible to calculate the Youngs modulus of the single trapped cells by deforming them. Experiments are currently being conducted in order to prove the validity of the simulations.

Bibliography

[1] E. Diamond, G. Y. Lee, N. H. Akhtar, B. J. Kirby, P. Giannakakou, S. T. Tagawa, and D. M. Nanus, "Isolation and characterization of circulating tumor cells in prostate cancer," *Front Oncol*, vol. 2, p. 131, 2012.

[2] R. Shayan, M. G. Achen, and S. A. Stacker, "Lymphatic vessels in cancer metastasis: bridging the gaps," *Carcinogenesis*, vol. 27, no. 9, pp. 1729–1738, 2006.

[3] W. J. Allard, J. Matera, M. C. Miller, M. Repollet, M. C. Connelly, C. Rao, A. G. J. Tibbe, J. W. Uhr, and L. W. M. M. Terstappen, "Tumor cells circulate in the peripheral blood of all major carcinomas but not in healthy subjects or patients with nonmalignant diseases," *Clinical Cancer Research*, vol. 10, no. 20, pp. 6897–6904, 2004.

[4] Y. Dong, A. M. Skelley, K. D. Merdek, K. M. Sprott, C. Jiang, W. E. Pierceall, J. Lin, M. Stocum, W. P. Carney, and D. A. Smirnov, "Microfluidics and Circulating Tumor Cells," *The Journal of Molecular Diagnostics*, vol. 15, pp. 149–157, mar 2013.

[5] S. M. Santana, H. Liu, N. H. Bander, J. P. Gleghorn, and B. J. Kirby, "Immunocapture of prostate cancer cells by use of anti-PSMA antibodies in microdevices," *Biomedical microdevices*, vol. 14, no. 2, pp. 401–407, 2012.

[6] G. Kokkinis, F. Keplinger, and I. Giouroudi, "On-chip microfluidic biosensor using superparamagnetic microparticles," *Biomicrofluidics*, vol. 7, no. 5, p. 54117, 2013.

[7] U. Schneider, H. Schwenk, and G. Bornkamm, "Characterization of EBV-genome negative "null" and "T" cell lines derived from children with acute lymphoblastic leukemia and leukemic transformed non-Hodgkin lymphoma," *International journal of cancer*, vol. 19, no. 5, pp. 621–626, 1977.

Chapter 9
Publication H

Microfluidic biosensing device for controlled trapping and detection of magnetic microparticles

Authored by I. Giouroudi, G. Kokkinis, C. Gooneratne, and J. Kosel. Published in *Proceedings of the* 29^{th} *Southern Biomedical Engineering Conference,* May 3-5, (2013), Miami, USA.

Abstract

A magnetic microfluidic device is proposed to transport and trap magnetic microparticles (MPs) to a sensing area. Once the MPs are concentrated in the vicinity of the sensing area, a spin valve type giant magnetoresistance (GMR) sensor is used to detect their presence. The device is used for the detection of biological targets once they are labeled with functionalized MPs. Manipulation of the MPs is achieved by employing a microstructure which consists of planar ringshaped conducting microloops. These microloops are designed to produce high magnetic field gradients which are directly proportional to the force applied to manipulate the MPs. Upon sequential application of current, starting from the outermost loop, MPs are directed to move from the outermost to the innermost loop. The speed with which the MPs move towards the sensing area is controlled by the speed with which current is switched between the loops. On top of the microstructure, a microfluidic channel is fabricated using a standard photolithography technique and a dry film resist layer (Ordyl® SY355). Experimental results showed that MPs of different diameters were successfully trapped at the sensing area and detected by the GMR sensor located directly under the innermost square loop.

9.1 Introduction

The selective manipulation of biological targets (e.g. pathogens such as *E. coli*) in lab-on-a-chip systems is attracting large interest. [1] Recent research trends suggest that MPs covered with a functionalization coating can be used to label these biological targets and thus manipulate and separate them by magnetic forces generated either by external magnets or by on-chip magnetic structures. Specifically, MPs are magnetized only in the presence of an external magnetic field. Therefore, the magnetic state of the MPs can easily be switched off simply by removing the external magnetic field. Integration of MP manipulation with magnetic detection seems very promising for sensitive, rapid and miniaturized biosensing devices. Miniaturization results in lower sample and reagent consumption, faster reactions and also enables accurate and efficient manipulation of target biological targets. [2, 3] Moreover, such integrated microdevices are highly sensitive and offer the option of on-site analysis since they can be implemented as handheld devices. Finally, they can be mass produced at a low cost. One of the main challenges in magnetic microfluidic-based, biosensing devices is to develop microsize magnetic field generators which produce a magnetic field strong enough to manipulate and confine biological targets labeled with functionalized MPs to a sensing area. The integration of magnetic microsensors that have high magnetic field sensitivity to detect and count the confined biological targets labeled with the MPs is another challenge. In this research we propose a device that includes a microfluidic channel and chamber, a unique magnetic microactuator (MMA) to manipulate MPs and an integrated GMR sensor. We present an effective way to trap MPs in a sensing area thus leading to a rapid and accurate detection of labeled biological targets with MPs.

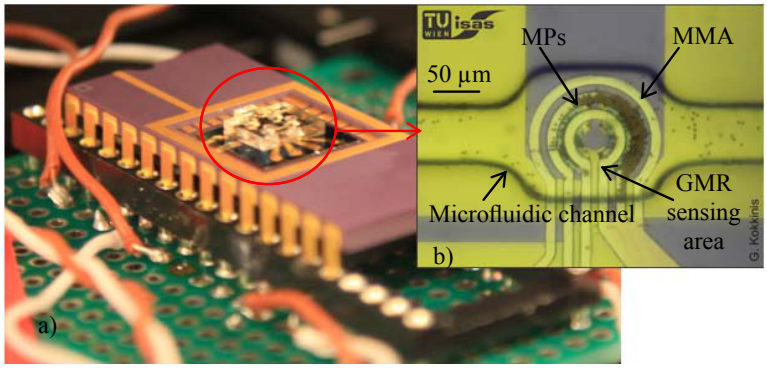

Figure 9.1: (a) The fabricated microdevice on a silicon substrate consisting of the GMR sensor, the magnetic microactuator (MMA) and the microfluidic channel placed on a circuit board in order to perform the measurements. (b) Microscope image of the fabricated microdevice with magnetic microparticles (MPs) inside the microfluidic channel.

9.2 Experiments

9.2.1 Fabrication

The spin valve GMR sensing elements were deposited using a magnetron sputtering system on a Si/SiO_2 substrate with the following bottom pinned structure: Substrate/ MgO 15/ $Ni_{80}Fe_{20}$ 2.5/ $Ir_{17}Mn_{83}$ 9/ $Co_{50}Fe_{50}$ 4.5/ Ru 0.8/ $Co_{50}Fe_{50}$ 1.0/ $Ni_{80}Fe_{20}$ 4/ $Co_{50}Fe_{50}$ 1.5/Cu 4/ $Co_{50}Fe_{50}$ 0.8/ $Ni_{80}Fe_{20}$ 5/Ru 1 (all thicknesses in nanometers) as presented in [4]. The GMR sensor had four GMR sensing elements with two active and two reference sensors in a Wheatstone bridge configuration. An MMA consisting of conducting loops that produce magnetic field gradients, which exert a force on the MPs was then fabricated on top of the GMR sensor. Finally, a microfluidic channel was fabricated on top of the MMA. The fabrication was realized using a standard photolithography process and a dry photoresist thin film (Ordyl® SY355) of 55 µm thickness. The fabricated microdevice is shown in Figure 9.1.

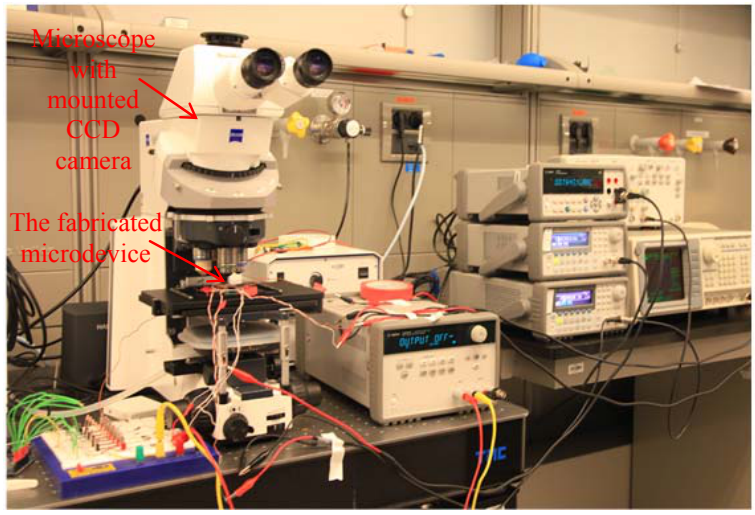

Figure 9.2: Measurement Set-up.

9.2.2 Measurement Set-up

Experiments were carried out using the measurement set-up shown in Figure 9.2 to prove the concept. The experimental process involved injecting 2 µl of MPs Dynabeads M270 coated with carboxylic acid having different diameters (2 µm - 6 µm) with a diluted concentration of 1 mg/ml to the microfluidic channel.

For the measurements a signal modulation technique was used. An AC current of 1 mA (RMS) was conducted through the GMR bridge at a frequency of 1 kHz. This carrier signal was modulated by the alternating magnetic field generated by the innermost coil conducting a current of 10 mA (RMS) at 210 Hz. The output of the GMR bridge was fed to a lock in amplifier. The reference signal was adjusted at 1.210 Hz in order to avoid crosstalk.

9.3 Results and discussion

The resistance of the GMR sensor was measured to be 458 Ohms. The maximum magnetoresistance was approximately 2% and the average sensitivity in the linear region was approximately 0.5 %/mT without application of an external bias field. Figure 9.3 shows experimental results of the variation of the GMR sensor output at four

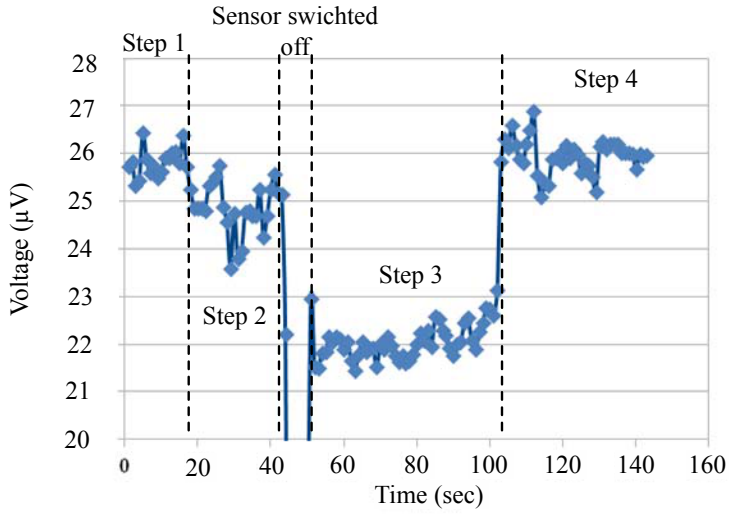

Figure 9.3: Experimental results showing the variation of the output of the Wheatstone bridge at different steps of the manipulation process.

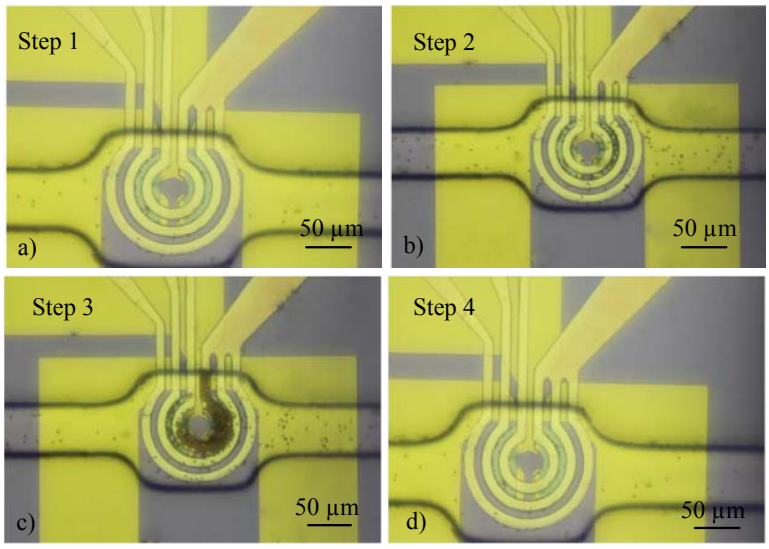

Figure 9.4: Images of the transported and trapped MPs (a) Step 1: the MPs are not yet at the sensing area (b) Step 2: the MPs begin to be attracted towards the innermost ring (c) Step 3: the MPs are in the sensing area, innermost ring (d) Step 4: the MPs are flushed away with water injected in the microfluidic channel.

different steps of the manipulation process and Figure 9.4 shows the images of the transported and trapped MPs during these different steps.

The movement of the MPs was captured by a CCD camera mounted on a microscope. In Step 1, no MPs were on the sensing area. Current was applied to the GMR sensor bridge. Its output signal was 26 µV due to some imbalance in the sensor bridge and differences in the magnetic fields produced by the MMA. In Step 2, after the MMA was switched on, the MPs began to be attracted towards the sensing area (center of the MMA) causing a slight difference in the voltage output. The bridge current was then switched off, so as not to interfere with the trapping procedure now fully controlled by the MMA. In Step 3 this current was switched back on, and an apparent voltage drop was observed due to the stray field of the MPs. In the final Step 4, the MMA was switched off and the MPs were flushed away with water injected in the microfluidic channel. It has to be noted that the change in magnitude due to the MPs stray magnetic field is causing a voltage drop rather than a rise because the magnetic field imposed to the sensing elements of the bridge is not identical and also because the sensing elements are not completely identical themselves, in terms of sensitivity.

Acknoledgement

The authors acknowledge the ”Hochschuljubilumsstiftung der Stadt Wien” for the financial support under the Project Nr: H1765/2012.

Bibliography

[1] M. A. M. Gijs, F. Lacharme, and U. Lehmann, “Microfluidic applications of magnetic particles for biological analysis and catalysis,” *Chemical reviews*, vol. 110, no. 3, pp. 1518–1563, 2009.

[2] C. P. Gooneratne, I. Giouroudi, and J. Kosel, “Microdevice with half-ring shaped GMR sensors for magnetic bead manipulation and detection,” in *Advancement in sensing technology*, pp. 121–138, Springer, 2013.

[3] I. Giouroudi and J. Kosel, "Recent progress in biomedical applications of magnetic nanoparticles," *Recent patents on nanotechnology*, vol. 4, no. 2, pp. 111–118, 2010.

[4] C. P. Gooneratne, C. Liang, I. Giouroudi, and J. Kosel, "An integrated micro-chip for rapid detection of magnetic particles," *Journal of Applied Physics*, vol. 111, no. 7, p. 07B327, 2012.

Chapter 10
Conclusions and Outlook

In the frame of this thesis, microfluidic platforms utilizing functionalized magnetic particles and integrated, magnetic sensors were designed, implemented and assessed in proof of concept studies , towards new lab-on-a-chip applications in diagnostics and biomedicine. Specifically, a bacteria detection biosensor, a biomolecule (e.g. antibodies) detection system, a nanomarker quantification system and rare cells trapping and detection schemes were realized and presented. In this chapter the cumulative conclusions of the studies conducted in this thesis, are reported and further research is proposed.

10.1 Bacteria detection biosensor

Initially, the potential of using the velocity change due to the volumetric increase (of the non-magnetic volume) of functionalized magnetic particles, conjugated with biological entities (of the μm scale), as a detection principle is demonstrated. The reason of this lower velocity was the enhanced Stoke's drag force. With the incorporation on the system of magnetic sensors, the means of on-chip velocity measurements are provided and successfully realized. In particular, single magnetic particles were successfully detected from the sensors. A velocity change between magnetically tagged *E. coli* bacteria and bare, unloaded magnetic particles was also successfully recorded. Lastly, a new signal acquisition scheme (from the magnetic sensors) that maximizes portability and minimizes costs was developed.

Further research should be conducted in order to assess the biosensor's capacity for defining the concentration of bacteria, the lower limit of detection as well as the detection range. Moreover,

other members of the family Enterobacteriaceae (e.g. Salmonella and Klebsiella) should be measured with the presented microfluidic biosensor in order to prove that it can be used as a general pathogen sensor.

10.2 Biomolecule detection system

Similarly to the bacteria detection biosensor, the velocity change was utilized in the detection of smaller organic compounds, down to the biomolecular scale. The detection of IgG antibodies was successfully demonstrated. This time the reason for the reduced velocity was assumed to be the change in the friction force between the antibody loaded and the plain unloaded magnetic particles. This assumption was proven by AFM friction force measurements. The actual nature of the enhanced friction is unclear but most probably linked to the 3D protein structure of the antibodies and their spatial orientation, protruding out of the magnetic particles' surface. In this system, the frictional forces are employed for the first time in the resolution of biomolecules, suggesting potential methods akin to capillary electrophoresis or liquid chromatography.

Undergoing studies seek to explore the possibility of using the same system for the detection of smaller entities other than antibodies, such as proteins or non-organic substances like polymers. Moreover, the correlation of the friction force is of interest.

10.3 Magnetic nanomarkers quantification system

The developed system was tested with commercial nanomarkers (Nanomag-D, 250 nm in size) as well as with custom functionalized (with an alginate hydrogel) magnetic nanoparticles. Nanomag-D particle concentrations as low as 500 pg/ µl were detected and quantified in a linear scale over a wide particle concentration range (1 - 500 ng/µl). Alginate functionalized magnetic particles were quantified in concentrations ranging from 100 - 1000 ng/µl and with a linear transform function.

During the course of the experiments it was reported that the time the magnetic particles needed to accumulate on the sensor's surface was also correlated to the concentration. Further experiments should be carried out in order to explore the potential of utilizing the accumulation time for extracting data, such as the surface functionalization or the presence of a biomolecule on the surface. That implies that frictional forces would slow down this accumulation.

10.4 Rare cell trapping platforms

Two distinctive platforms were presented. In the first, cell traps were fabricated on a photostructurable polymer. The efficiency of the system was demonstrated by successfully trapping leukaemia cells, tagged with magnetic particles, for further analysis. Simulations suggest that it is possible to calculate the Youngs modulus of the single trapped cells by deforming them. The second system is using microconducting rings for the entrapment of magnetic particles and it detects their present using magnetic sensors.

All the aforementioned sytems were developed for proof of concept studies. In order to fully exploit their potentials a lot of challenging issues must be confronted. Of course the same applies for most of the devices proposed in the frame of the emerging field of microfluidics. The quest for the development of more robust, hand-held, integrated and user-friendly devices that will revolutionize modern medicine in the field of diagnostics and threurapeutics is bound to last.

Appendix A

Supplementary information: Publication D

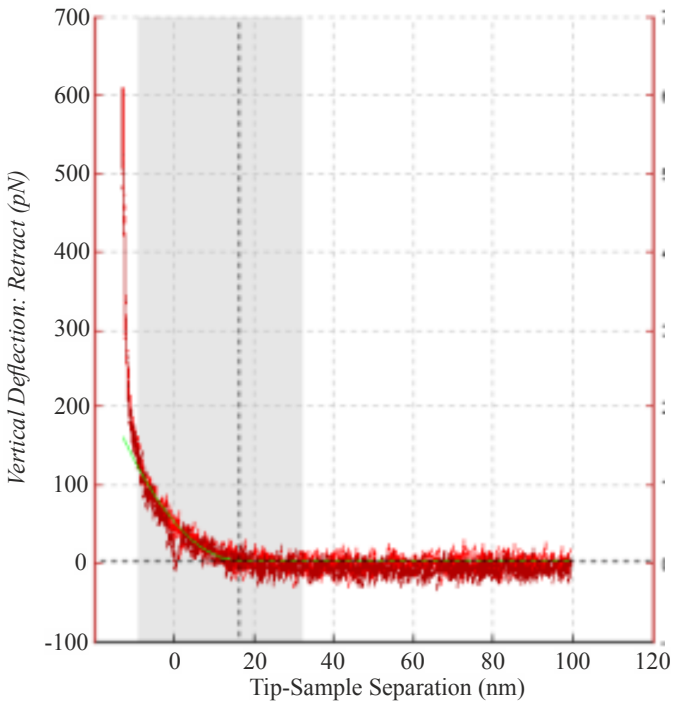

Figure A.1: Evaluation of the surface modification thickness from the vertical deflection versus the tip-sample separation in nm; thickness evaluated between 20 - 25 nm.

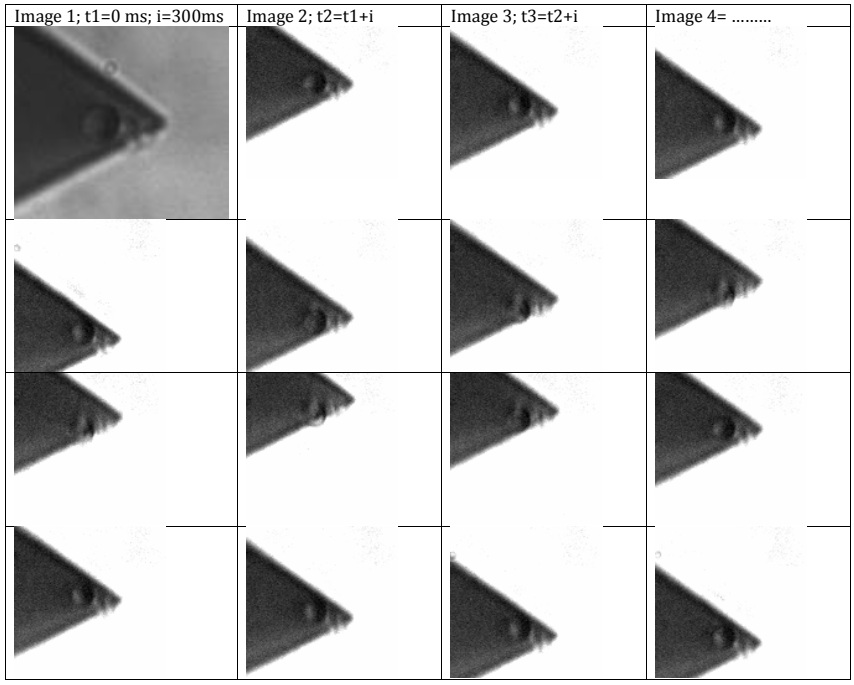

Figure A.2: Different instances of the AFM-tip during scan (tipless cantilever: nanoSensor): the tips were functionalized with APTES and a biotin-PEG-NHS crosslinker. The long crosslinker results to a drift of the MPs with respect to the tip during measurements, thus an alternative measurement scheme was used.

Acknowledgements

From the first day I arrived in the Institute of Sensors and Actuators Systems (ISAS) of the Technische Universität Wien, I realized that synergy is the "modus operandi" of the research group. I was overwhelmed by the eagerness of everybody to answer my numerous questions, to propose ideas and to actively engage in overcoming obstacles, of scientific or other, nature.

In particular, I would like to thank Dr. Ioanna Giouroudi for giving me the chance to come to Vienna and work on the FWF (Austrian Science Fund) project (No. P24372-N19), within the Industrial Sensors' research group. Dr. Giouroudi has been an excellent advisor, that aspired me to achieve higher goals and provided me with solid scientific guidance on the field of magnetism, nanoparticle technology and magnetic sensors technology.

I would like to gratefully thank my supervisor, Univ.-Prof. Dr. Franz Keplinger. As head of the department of Industrial Sensors, he provided an excellent working environment, as well as scientific advice and support over the years. I particularly enjoyed discussions about research and other matters with him. Finally, he offered a great help in the writing of this thesis.

I am really grateful to Dietmar Puchberger-Enengl for indulging me into the microfluidics' theoretical and practical aspects and for promptly responding to any request for help, at a wide range of topics. The same applies for Christoph Haiden, that on top of the other had the "luck" of sharing the same office with me. He has been most welcoming and friendly and I thank him for that. Lastly, Anna Haller, although we met later on during my studies, she contributed to the excellent working environment that made this thesis feasible.

Silicon technology is a extensive scientific branch with numerous of applications and processes that require sound knowledge of all the physical and chemical parameters, as well as considerable experience. All of these assets are encountered at the technical personnel of the ISAS. Thus I owe my gratitude to Ing. Peter Svasek, Ing. Edeltraud Svasek, Dr. Johannes Schalko, Dr. Arthur Jachimowitz,

Patryk Meyer and Alexander Klein for helping me with the device fabrication and for the interesting discussions about the feasibility of my designs. Everybody has been very cooperative and responsive to short calls.

Special thanks to Prof. Susana Cardoso and Felipe Cardoso of the INESC Microsistemas e Nanotecnologias, Lisbon for introducing me in the technology of GMR sensor fabrication and co-producing the sensors of the devices presented in this thesis. To Dr. Birgit Plochberger for performing the Atomic Force Microscopy measurements. To Prof. Jurgen Kosel for introducing me to MEMS technology and to Prof. Hari Srikanth and Mahn-Huong Phan who provided me with custom made magnetic nanoparticles.

In addition I want to thank the master students: Murad Jamalieh, Alexander Dangl, Richard Mitterboeck and Martin Stipsitz for their invaluable contribution in our research findings and their co-operation throughout the course of their thesis.

Lastly, a great thank to my parents Evangelos and Vasiliki Kokkinis for supporting me all these years with their love, trust and guidance.

List of Publications

Peer-reviewed Journal Papers

[1] G. Kokkinis, B. Plochberger, S. Cardoso, F. Keplinger, and I. Giouroudi, "A microfluidic, dual-purpose sensor for in vitro detection of Enterobacteriaceae and biotinylated antibodies," *Lab Chip*, vol. 16, no. 7, pp. 1261–1271, 2016.

[2] G. Kokkinis, S. Cardoso, F. Keplinger, and I. Giouroudi, "Magnetic Microfluidic Platform for Quantification of Cancer Cells," *RSC Advances*, (under review), 2016.

[3] M. Jamalieh, G. Kokkinis, C. Haiden, T. Berris, F. Keplinger, and I. Giouroudi, "Microfluidic Platform for Pathogen Load Monitoring," *Journal of microelectronic engineering*, vol. 158, pp. 91–94, 2016

[4] G. Kokkinis, R. Mitterboeck, T. Berris, M. Jamalieh, F. Keplinger, and I. Giouroudi, "Magnetic Microfluidic Single Trapping and Analysis Platform," *JMAST*, (Accepted), 2016.

[5] J. Devkota, G. Kokkinis, T. Berris, M. Jamalieh, S. Cardoso, F. A. Cardoso, H. Srikanth, M.-H. Phan, and I. Giouroudi, "A novel approach for detection and quantification of magnetic nanomarkers using a spin valve GMR-integrated microfluidic sensor," *RSC Advances*, vol. 5, p. 51169, 2015.

[6] G. Kokkinis, M. Jamalieh, F. Cardoso, S. Cardoso, F. Keplinger, and I. Giouroudi, "Magnetic-based biomolecule detection using giant magnetoresistance sensors," *Journal of Applied Physics*, vol. 117, p. 17B731, May 2015.

[7] G. Kokkinis, S. F. Cardoso, F. A. Cardoso, and I. Giouroudi, "Microfluidics for the Rapid Detection of Pathogens Using Giant Magnetoresistance Sensors," *IEEE Transactions on Magnetics*, vol. 50, pp. 2–5, nov 2014.

[8] G. Kokkinis, F. Keplinger, and I. Giouroudi, "On-chip microfluidic biosensor using superparamagnetic microparticles," *Biomicrofluidics*, vol. 7, no. 5, p. 54117, 2013.

Proceedings in International Conferences

[1] G. Kokkinis, M. Phan, H. Srikanth, S. Cardoso, and I. Giouroudi, "Magnetic Microfluidic Biosensor for the Detection & Quantification of Biomolecules," in *Proceedings - 32th Southern Biomedical Engineering Conference, SBEC 2016*, (Accepted), 2016.

[2] J. Devkota, G. Kokkinis, M. Jamalieh, M. Phan, H. Srikanth, S. Cardoso, F. Cardoso, and I. Giouroudi, "GMR microfluidic biosensor for low concentration detection of Nanomag-D beads," in *Progress in Biomedical Optics and Imaging - Proceedings of SPIE*, vol. 9518, 2015.

[3] R. Mitterboeck, G. Kokkinis, T. Berris, F. Keplinger, and I. Giouroudi, "Magnetic microfluidic system for isolation of single cells," in *Progress in Biomedical Optics and Imaging - Proceedings of SPIE* (S. van den Driesche, ed.), vol. 9518, p. 951809, jun 2015.

[4] I. Giouroudi, G. Kokkinis, K. Fodil, M. Denoual, C. Dolabdjian, S. Madtha, Torabi-Makhsos, and F. Keplinger, "On-chip separation and detection of magnetically labeled pathogens," *Journal of Nanomedicine & Nanotechnology*, vol. 05, no. 05, 2014.

[5] M. Stipsitz, G. Kokkinis, C. Gooneratne, J. Kosel, S. Cardoso, F. Cardoso, and I. Giouroudi, "Magnetic Microfluidic Platform for Biomedical Applications Using Magnetic Nanoparticles," *Key Engineering Materials*, vol. 644, pp. 207–210, may 2015.

[6] I. Giouroudi, C. Gooneratne, and G. Kokkinis, "Controlled Trapping and Detection of Magnetic Particles by a Magnetic Microactuator and a Giant Magnetoresistance (GMR) Sensor," *Key Engineering Materials*, vol. 605, pp. 352–355, apr 2014.

[7] A. Dangl, G. Kokkinis, F. Keplinger, and I. Giouroudi, "In vitro biosensing based on magnetically induced motion of magnetic

nanoparticles," in *Technical Proceedings of the 2013 NSTI Nanotechnology Conference and Expo, NSTI-Nanotech 2013*, vol. 3, pp. 135–138, 2013.

[8] I. Giouroudi, G. Kokkinis, C. Gooneratne, and J. Kosel, "Microfluidic biosensing device for controlled trapping and detection of magnetic microparticles," in *Proceedings - 29th Southern Biomedical Engineering Conference, SBEC 2013*, (Miami, FL), pp. 1–2, 2013.

[9] G. Kokkinis, A. Dangl, F. Keplinger, and I. Giouroudi, "Microfluidic Biosensing Method Using the Motion of Magnetic Microparticles," *Key Engineering Materials*, vol. 605, pp. 348–351, apr 2014.

[10] G. Kokkinis, F. Keplinger, and I. Giouroudi, "Magnetophoretic manipulation of suspended magnetic particles for on-chip biosensing applications.," in *Proceedings of the 3rd International Conference on Bio-Sensing Technology, Sitges, Spain, May*, 2013.

Other Publications

Proceedings in International Conferences

[1] G. Kokkinis, "Magnetic Field Sensor Based on the Domain Wall Nucleation and Propagation," *Key Engineering Materials*, vol. 495, pp. 225–228, 2012.

[2] G. Kokkinis, "Cordless position sensor based on the magnetostrictive delay line principle," *Key Engineering Materials*, vol. 495, pp. 220–224, 2012.

Book Chapters

[1] G. Kokkinis, S. Cardoso, I. Giouroudi, "Biomedical applications of magnetic nanoparticles," submitted in the book: *Lecture Notes in Nanoscale Science and Technology*, 2016.

About the Author

Georgios Kokkinis was born in Athens, Greece, in 1983. Between 2001 and 2007 he studied Electrical Enginnering at the Aristotle University of Thessalloniki, Greece, from where he received his Engineering Diploma degree. After working for a year as an Automation engineer, concluding his military service and his European Voluntary Service (EVS), he went back to acquiring a master's degree in Automation and Control by the National Technical University of Athens (NTUA), Greece. His Master's thesis topic was the implementation of sensors using amorphous magnetic wires. Since 2011 he has been employed in research groups; initially in the Electronic materials research group of the NTUA, then in the GREYC - Electronics research group of the Ecole nationale superieure d'ingenieurs de Caen, France and finally in the Institute of Sensors and Actuators Systems of the Technische Universitt Wien in the frame of the Austrian Science Fund's (FWF) project with No. P 24372-N19 and title "On-chip Biosensing Utilizing the Motion of Magnetic Particles".